

THESIS FOR THE DEGREE OF DOCTOR OF PHILOSOPHY

Studies of acoustic waves, noise and charge
pumping using single-electron devices

MARTIN GUSTAFSSON

Department of Microtechnology and Nanoscience
CHALMERS UNIVERSITY OF TECHNOLOGY
Göteborg, Sweden 2012

Studies of acoustic waves, noise and charge pumping using single-electron devices

MARTIN GUSTAFSSON

©Martin Gustafsson 2012

ISBN 978-91-7385-676-8

Doktorsavhandlingar vid Chalmers tekniska högskola

Ny serie nr 3357

ISSN 0346-718X

ISSN 1652-0769

Technical Report MC2-223

Quantum Device Physics Laboratory

Department of Microtechnology and Nanoscience - MC2

Cover art: Surface acoustic wave impinging on a single-electron transistor, by Philip Krantz
2012

Chalmers Reproservice
Göteborg, Sweden 2012

Studies of acoustic waves, noise and charge pumping using single-electron devices

MARTIN GUSTAFSSON

Department of Microtechnology and Nanoscience

Chalmers University of Technology, 2012

Abstract

This thesis covers a range of experiments on single-electron devices, electrical circuits that utilize the discreteness of the electron charge. The Single-Electron Transistor (SET) is of special importance among these, being the most sensitive electrometer demonstrated, and sufficiently mature to serve as a building block in sensors and detectors for physical phenomena that can be transformed into charge signals.

Such an example is the use of the SET as a local probe for Surface Acoustic Waves (SAW), demonstrated here for the first time. The SAW is a mechanical wave propagating on the surface of a solid, in this case a GaAs substrate. Due to the piezoelectricity of GaAs, the SAW is accompanied by a wave of electrical polarization which couples efficiently to an SET deposited on the same substrate. The experiments demonstrate a sensitivity to surface displacement of $30 \text{ am}/\sqrt{\text{Hz}}$, which is 2–3 orders of magnitude better than in previous SAW experiments. The SET is located between two on-chip acoustic reflectors separated by 2.9 mm, and has a sufficient measurement bandwidth to resolve the echoes of acoustic pulses between the reflectors. The resolution when averaging over many pulses is sufficient to resolve an average energy of $\hbar\omega$ per pulse reaching the SET. These experiments, along with associated theoretical treatments, indicate that studies on propagating acoustic waves in the quantum mechanical regime are feasible.

The high charge sensitivity of the SET was also applied in prototypes for detection of single optical photons, where photo-generated electron-hole pairs near the surface of a semiconductor heterostructure are separated and transported to within the detection range of SETs deposited on the same chip.

Another part of the thesis concerns the characterization of charge noise, which limits performance in SETs and related devices such as qubits and electron pumps. The dependence of the noise level on temperature and SET bias conditions is investigated, as well as its connection to the long-term relaxation observed after sudden application of a strong electric field. The results show that the sources of charge noise are in thermal equilibrium also at comparatively low temperature, and are in strong thermal contact with the electrons residing in the SET. This gives an indication about the microscopic nature and possible locations of the noise sources.

The final part of the thesis is devoted to the study of quantized current sources, devices which can transport electrons one by one through a circuit at a controlled rate. To be comparable with other metrological standards, such a current source must be accurate to around one part in 10^8 , which requires careful study and elimination of all possible error sources. Errors due to Photon-Assisted Tunneling were studied in a resistively terminated multi-junction pump, and errors due to Andreev tunneling were demonstrated in a hybrid SINIS electron turnstile. The latter experiment shows that errors due to Andreev tunneling is reduced substantially in turnstiles with high charging energy.

Keywords: single-electron devices, single-electron transistor, SET, electrometer, surface acoustic wave, SAW, noise, two-level fluctuator, TLF, single-photon detector, charge pumping, single-electron pump, SINIS turnstile.

List of publications

This thesis is based on the work contained in the following papers:

I: Local probing of propagating acoustic waves in a gigahertz echo chamber

Gustafsson, M. V., Santos, P. V., Johansson, G., and Delsing, P.

Nature Physics, **8**, 338-343, (2012)

Supplementary material is attached with this paper.

II: Activation mechanisms for charge noise

Gustafsson, M. V., Pourkabirian, A., Johansson, G., Clarke, J., and Delsing, P.

Submitted to Physical Review Letters, (2012)

III: Acousto-electric single-photon detector

Batista, P. D., Gustafsson, M., de Lima, Jr., M. M., Beck, M., Talyanskii, V. I., Hey, R., Santos, P. V., Delsing, P., and Rarity, J.

Proceedings of SPIE: Photon Counting Applications, Quantum Optics and Quantum Cryptography, **6583**, 658304, (2007)

IV: Photon-Assisted Tunneling in a Resistive Electron Pump

Giblin, S., Gustafsson, M., Lotkhov, S. V., and Zorin, A. B.

AIP Conference Proceedings: 24th International Conference on Low Temperature Physics, **850**, 1425-1426, (2006)

V: Andreev tunneling in charge pumping with SINIS turnstiles

Aref, T., Maisi, V. F., Gustafsson, M. V., Delsing, P., and Pekola, J. P.

EPL, **96**, 37008, (2011)

Preface

During my time as a Ph.D. student, I have worked on several research topics. They all involve single-electron devices but are otherwise somewhat dissimilar, and that reflects in the structure of this thesis: To make the reading as easy as possible I have devoted a separate chapter to each topic, rather than merging material from all projects under general headings. The chapters are arranged in approximately inverse chronological order, with subjects relevant to more than one topic gathered in Chapter 2.

The readers of a Ph.D. thesis generally fall into three categories, each with a different level of prior knowledge: The first group consists of the experts whose role it is to review the scientific merits of the work. A primary goal in the writing has of course been to satisfy this group of readers.

On the opposite side of the scale of expertise are the casual readers, who do not have scientific backgrounds, but may be interested in finding out what has kept me busy all this time. The Introduction in Chapter 1 is written with this readership in mind.

The final group consists of new PhD students, who are educated in physics but may lack experience with the field. These are the readers that can potentially make use of the text, as I have made great use of the works by previous students. In the hope that sophisticated readers will look past the occasional triviality, my aim has been to write a thesis that would have been useful to me when I first began to study these topics.

Abbreviations and symbols

Natural constants:

e	Electron charge
h	Planck constant
k_B	Boltzmann constant
ϵ_0	Vacuum permittivity
R_K	Resistance quantum, h/e^2

Abbreviations:

CP	Cooper pair
$e - ph$	Electron - phonon (<i>e.g.</i> $e - ph$ thermalization)
HEMT	High electron mobility transistor
IDT	Interdigital transducer
LO	Local oscillator
PSD	Power spectral density
QP	Quasiparticle
RF	Radio-frequency
RF-SET	SET read-out by radio-frequency reflectometry
SAW	Surface acoustic wave
SEB	Single-electron box
SET	Single-electron transistor
SINIS	Superconductor, insulator, normal metal, insulator, superconductor
SNR	Signal-to-Noise Ratio
SQUID	Superconducting quantum interference device
S-SET	Superconducting SET
TIA	Transimpedance amplifier
TLF	Two-level fluctuator

General variables and quantities:

f	Frequency
ω	Angular frequency ($2\pi f$)
T	Temperature
E	Energy
\mathbf{E}	Electric field
\mathbf{P}	Electric polarization
Q	Charge
P_n	Probability for state n
$\Gamma_{n \rightarrow m}$	Transition rate from state n to state m
S_x	PSD of the quantity x
Δ	Superconducting gap energy
E_F	Fermi energy

SETs:

Q_g	Induced charge
n_g	Q_g/e
δQ	Charge sensitivity

Γ_0	Charge transfer function
R_J	Junction resistance
R_s	Source junction resistance
R_d	Drain junction resistance
R_Σ	Total junction resistance
C_J	Junction capacitance
C_s	Source junction capacitance
C_d	Drain junction capacitance
C_g	Gate capacitance
C_Σ	Total capacitance
E_C	Charging energy
V_b	Bias voltage
V_g	Gate voltage
I_{SET}	SET current
A_{SET}	Area of an SET island
f_p	Pilot signal frequency
Q_p	Induced charge from a pilot signal

RF techniques:

f_0, ω_0	Center frequency
Z_0	Transmission line impedance
Z_S	Source impedance
Z_L	Load impedance
Z_{LC}	Impedance of a series LC -circuit on resonance
Z_{LCR}	Impedance of an LC -circuit with embedded SET resistance R
Γ	Amplitude reflection coefficient
Q	Quality factor
Q_{ext}	External quality factor
Q_{int}	internal quality factor
BW	Bandwidth
RBW	Resolution bandwidth
f_p	Pilot signal frequency
f_{RF}	Frequency of applied RF signal
f_{LO}	Local oscillator frequency
τ	RF period ($1/f_{RF}$)
Q_{RF}	Induced charge at high frequency
Q_{DC}	Induced charge at low frequency
Q_{LO}	Induced charge from a local oscillator
Q_p	Induced charge from a pilot signal

Thermalization:

P_{SET}	Power dissipated on an SET island
P_{e-ph}	Electron-phonon thermalization power
T_0	Refrigerator temperature
T_e	Electron temperature
T_{ph}	Phonon temperature
T_{sub}	Phonon temperature in the substrate immediately under an SET island
T_{TLF}	Temperature of an ensemble of TLFs
Σ	Electron-phonon thermalization coefficient
Ω	Electron-phonon thermalization volume
n	Electron-phonon thermalization exponent

Λ Thermal conductivity

Noise and TLFs:

S_Q	Charge noise PSD
$S_{Q,Lor}$	Lorentzian charge noise PSD, from a single TLF
\tilde{S}_Q	Characteristic level of charge noise
$S_{I,shot}$	Current shot noise
$S_{V,exc}$	Voltage shot noise PSD integrated over negative frequencies
α	Actual slope in a log-log plot of an $1/f$ -like spectrum.
E_{TLF}	Barrier height or activation energy for a TLF
E_1 E_2	Barrier heights for a double-well TLF
ΔE	Energy difference between TLF states
P_g	Ground state occupation probability
P_e	Excited state occupation probability
Γ_{\uparrow}	Transition rate from the ground state to the excited state
Γ_{\downarrow}	Transition rate from the excited state to the ground state
q_{TLF}	Charge of the stochastically moving particle in models for TLFs
n_{TLF}	Spatial density of TLFs
χ_{TLF}	Electrical susceptibility of an ensemble of identical TLFs with density n_{TLF}
χ_i	Susceptibility of an idealized material
d_{TLF}	Physical separation between the two potential wells of a TLF
G	Geometry factor for a capacitor, with the dimension of distance
F	Fano factor

SAW:

v_{SAW}	SAW propagation speed
λ	SAW wavelength
λ_0	Periodicity of an IDT or SAW reflector
f_{SAW}	SAW frequency
K^2	Electro-acoustic coupling coefficient of a material surface
y_{SAW}	Characteristic SAW conductance of a material surface
Y_{SAW}	Characteristic conductance of a SAW channel
Z_{SAW}	Characteristic SAW beam impedance; the inverse of Y_{SAW}
ϕ	Complex SAW amplitude expressed in electric potential
ϕ^+ , ϕ^-	SAW amplitude in the forward and backward direction
ϕ_{in}	Incoming SAW amplitude
ϕ_{em}	SAW amplitude emitted by an IDT
Q_{SAW}	Charge amplitude induced on the SET by the SAW
P_{IDT}	Power applied to IDT, assuming matched impedance
V_{IDT}	Voltage amplitude applied to IDT, assuming matched impedance
V_T	IDT voltage
P_{SAW}	Power carried by a SAW
C_S	Characteristic capacitance of a material surface
C_T	IDT capacitance
W_{IDT}	IDT width
N_{IDT}	Number of finger pairs in an IDT
μ	Conversion factor from voltage to SAW potential for an IDT
μ_s	Conversion factor from voltage to SAW potential for a single IDT finger
g_m	Conversion factor from SAW potential to IDT current
G_a	Acoustic conductance of an IDT
iB_a	Imaginary acoustic admittance of an IDT

r_f	Amplitude reflection coefficient of each finger in a SAW reflector or IDT
R	Power reflection coefficient
d_{ref}	Reflection depth of a SAW reflector or IDT
β	SAW reflection power loss
σ	Surface charge density
e_{14}	Piezoelectric constant of GaAs
S_{xx}	Surface strain in the \hat{x} -direction
u_x	\hat{x} -directed surface displacement
u_z	\hat{z} -directed surface displacement
\tilde{u}_z	\hat{z} -directed surface fluctuations
c_x	Relation between \hat{x} -directed surface displacement and SAW potential
c_z	Relation between \hat{z} -directed surface displacement and SAW potential
C_{SAW}	Coupling from IDT to SET, with acoustic resonance
C_{SAW}^*	Coupling from IDT to SET, without acoustic resonance

Transmon qubits:

E_C	Charging energy
E_J	Josephson energy
L_J	Josephson inductance
C_{tr}	Geometric transmon capacitance
W_{tr}	Length of transmon fingers
N_{tr}	Number of transmon finger pairs
R	Power reflection coefficient
T	Power transmission coefficient
Γ_{tr}	Coupling frequency

Charge pumps:

n_J	Number of junctions
R_P	Electron pump series resistor
V_T	Microwave amplitude
\tilde{n}_g	Pump amplitude in electron units
$d_{n \rightarrow m}$	Transition threshold for tunneling from state n to state m , through the drain junction
$s_{n \rightarrow m}$	Transition threshold for tunneling from state n to state m , through the source junction

Contents

Abstract	iii
List of publications	v
Preface	vi
Abbreviations and symbols	vii
1 Introduction	1
2 Background and common topics	3
2.1 Single-electron devices	3
2.1.1 The single-electron transistor	5
2.1.2 Power dissipation in the SET	7
2.1.3 Noise in SETs	8
2.1.4 Radio-frequency SET read-out	10
2.1.5 The SET as an intrinsic GHz mixer	14
2.1.6 Superconductivity	17
2.2 Surface acoustic waves	19
2.3 Cryogenics	24
2.4 Sample fabrication	29
3 Coupling quantum devices to surface acoustic waves	35
3.1 Experimental setup	35
3.2 Basic characterization	37
3.3 Acoustic modeling	39
3.4 Sensitivity	39
3.5 Noise and back-action	40
3.6 Coupling SAW to a superconducting qubit	42
3.7 Conclusions and outlook	45
4 Charge noise in SETs	47
4.1 Experimental setup	47
4.2 Thermal properties of charge noise	50
4.3 Descriptions of TLFs and their susceptibility	56
4.4 Step response of charge TLFs	59
4.5 Conclusions and outlook	59

5	Photon detection with SETs on heterostructures	63
5.1	Heterostructures	64
5.2	Surface acoustic wave carrier transport	66
5.3	Resistive carrier guiding	69
5.4	Conclusion and outlook	69
6	Charge pumping with single-electron devices	71
6.1	Photon-assisted tunneling in a resistive electron pump	72
6.2	Principles of the SINIS turnstile	73
6.3	SINIS samples and experiments	76
6.4	Conclusions and outlook	77
A	Recipes for sample fabrication	79
A.1	Three-layer hard mask	79
A.2	Large scale photolithography.	80
A.3	Large-scale e-beam lithography	80
A.4	Small-scale e-beam lift-off	81
	Acknowledgements	83
	Bibliography	85

Chapter 1

Introduction

In everyday life, we rarely see any effects of the fact that electrical current flows in the form of electrons, individual packets of charge. Even though electrons repel each other, a piece of metal the size of a coin can be charged with hundreds of them before it gets notably difficult to add another one. The repulsion becomes more prominent the less space the electrons have to share, and for a grain less than a micrometer in size, it may take substantial effort to add an extra electron, even if the grain was initially uncharged. This is utilized in the group of electrical circuits known as *single-electron devices*.

If two pieces of metal are brought close to – but not quite into – contact with each other, it is possible for electrons to jump over the gap by so-called *quantum mechanical tunneling*. The gap is then known as a *tunnel junction*, and a voltage over the junction can make the electrons jump in a certain direction. When two large pieces of metal (the *source* and the *drain*) couple to a single grain by tunnel junctions, electrons can jump from the source to the grain through one junction and from the grain to the drain through the other one, thereby producing an electric current.

If the electrons truly were a continuous fluid, capable of flowing freely through the junctions, there would always be just enough electron fluid on the grain to keep it neutrally charged. We call this *optimal* amount of electron charge Q_g , and it depends on what other charges are in the vicinity of the grain, repelling or attracting its electrons.

In reality, the electrons are discreet quanta, each with the charge e , so the electron charge on the grain is always $n \times e$ where n must be an integer. The optimal charge Q_g , on the other hand, can take on any value. For $Q_g = 1 e$, one electron can render the grain perfectly neutral. This is a stable state – if we try to add an electron to the grain it will be repelled, and if we try to remove one it will be attracted back. This in turn means that no current can flow from source to drain: The electrons jump one at a time, so any current would have to start with an electron entering or exiting the grain, in either case removing it from the stable state.

If the optimal electron charge on the grain is instead $Q_g = e/2$, it does not matter if the number of actual electrons is $n = 0$ or $n = 1$, since both cases differ equally from the optimum. Starting from $n = 0$, an additional electron can easily tunnel in and change the state to $n = 1$. Just as easily, it can then tunnel out again through the opposite junction. This cycle can then repeat itself at a high rate, allowing a current to flow from source to drain while the number of electrons on the grain flips back and forth between $n = 0$ and $n = 1$.

The lack of current at $Q_g = n e$ is known as the *Coulomb blockade*, and the device with two tunnel junctions coupled to a grain is a *Single-Electron Transistor* or SET, shown schematically

in Fig. 2.2. Since the SET current changes dramatically with minute changes in Q_g , which in turn depends on the presence of charge in the vicinity of the grain, the SET works as a very good electrometer. At room temperature, the random motion of electrons is fast enough to overcome the Coulomb blockade, *i.e.* jump onto the island even though $Q_g = ne$. Thus, SETs and similar devices are usually cooled to 1 K – one degree above absolute zero – or lower in order to work as intended.

We can exploit the charge sensitivity of the SET to detect physical effects that do not inherently involve the motion of charges, but may in some way be converted to charge signals. This thesis presents two such detector applications: A photon detector and a sensor for Surface Acoustic Waves (SAW).

Surface acoustic waves are sound waves that move over the flat surface of a solid. They can exist on scales from the microscopic to the seismic, in the latter case caused by earthquakes and known as “ground roll”. On the microscopic scale, SAW can be produced artificially on the surface of a microchip made from a piezoelectric crystal. Characteristic for piezoelectric materials is that they produce electric charge on their surfaces when deformed, and since SAW is a wave of mechanical deformation, it is joined with a wave of surface charge wherever it goes on the chip. An SET can be deposited on the same surface, and its high charge sensitivity then makes it well suited to detect SAW with very low amplitudes, which is the topic of Ch. 3. The ultimate goal of such a sensor and associated components is to bring SAW into the realm of quantum mechanics – to produce and detect propagating phonons, *i.e.* quantum particles of sound.

Phonons are the mechanical equivalent of photons, the quantum particles that constitute light. Photons can also be made to produce free charges, which in turn can be detected by SETs. In the example studied in Ch. 5 of this thesis, a photon hitting a piece of semiconductor sets loose an electron that was previously bound, so that it can move around in the semiconductor material. It is possible to grow a layered structure of semiconductors that can confine such an unbound electron – and the hole left in its wake – to a sheet near the semiconductor surface. Both the electron and the hole can then be guided in the lateral directions, either with the moving electric field from a SAW or with steadily applied voltages, to regions of the surface where SETs have been deposited to detect their charges.

The SET does not only react to the charge we set out to detect, but also to random movements of charged particles in its surroundings. This *charge noise* does not only affect SETs, but other sensitive devices such as the qubits that are developed as building blocks for future quantum computers. In spite of the many studies that have been done, it is not clear exactly what the sources of charge noise are or where they are located. The SET is a good tool for investigating this, and such studies are presented in Ch. 4.

If several grains and tunnel junctions are connected in series, it is possible to transport one electron from grain to grain in a controlled manner, while the free flow of current is prohibited just as in the Coulomb-blockaded SET. Such a device is known as a *single-electron pump*, which can produce an accurate current by sourcing electrons at a rate that is high and well-controlled. For instance, transferring 100 million electrons per second corresponds to a current of 16 pA.

The Coulomb blockade can also be used together with the special properties of superconductors in a different kind of electron pump, which has some advantages compared with the multi-grain type. To make either type of pump sufficiently accurate to serve as a universal comparison standard for current, it is important to determine the sources of error and find means to suppress them, which is the topic of Ch. 6 of this thesis.

Chapter 2

Background and common topics

2.1 Single-electron devices

The single-electron tunneling devices are a family of electrical circuits that rely on the discreteness of electrical charges for their operation. They include the single-electron transistor [1, 2] which is the record holder in electrometer sensitivity [3], charge pumps which aspire to become metrological standards for electrical current [4–7], and attempts are being made to use them for digital memories and logic [8, 9]. Refs. [9–12] provide good introductions to the field.

The simplest member of the family, the Single-Electron Box (SEB), is depicted in Fig. 2.1(a). Apart from a regular voltage source and a capacitor, it contains a small *tunnel junction*, a circuit element particular for this class of devices. The tunnel junction physically resembles a capacitor, but has the special feature that an electron can move from one terminal to the other by quantum mechanical tunneling. It is characterized by its capacitance C_J and its resistance R_J which gives the current of tunneling electrons in the limit of high voltage bias by Ohm's law. Given a high enough resistance, $R_J \gtrsim \frac{h}{e^2} \approx 26 \text{ k}\Omega$, where h is Planck's constant and e the electron charge, electrons are localized to either side of the junction, and the tunneling from one side to the other can be regarded as an instantaneous event.

Ramping up the gate voltage V_g applied to the SEB polarizes the capacitors C_g and C_J , creating a deficit of electrons in the region between them, known as the “box” or the “island”. We denote the total capacitance of the island with C_Σ . In this simple case, it is just the sum of C_g and C_J , whereas in a more general circuit it will include any additional junctions and stray capacitances.

The charge induced on the island, $Q_g = V_g C_g$, is a continuous variable, and if electrons had been a continuous medium, the exact opposite charge, $-Q_g$, would enter the island to render it electrically neutral. However, since an electron must either enter the island with all its charge or none at all, the island can be neutral only for certain values of Q_g , and otherwise charged with $Q_g - n e$, where n is the number of electrons that have entered the island, starting from $n = 0$ at electrostatic equilibrium with $Q_g = 0$. This charging stores a potential energy $E = (Q_g - n e)^2 / 2C_\Sigma$. As the gate voltage increases from zero, the $n = 0$ state gets less and less energetically favorable, until Q_g reaches the value $e/2$, where the states $n = 0$ and $n = 1$ are energetically degenerate and an electron can easily hop back and forth through the junction, switching the circuit between the two states. As the gate voltage increases further, $n = 1$ will be the most stable state until Q_g reaches the value $3e/2$, where the states $n = 1$

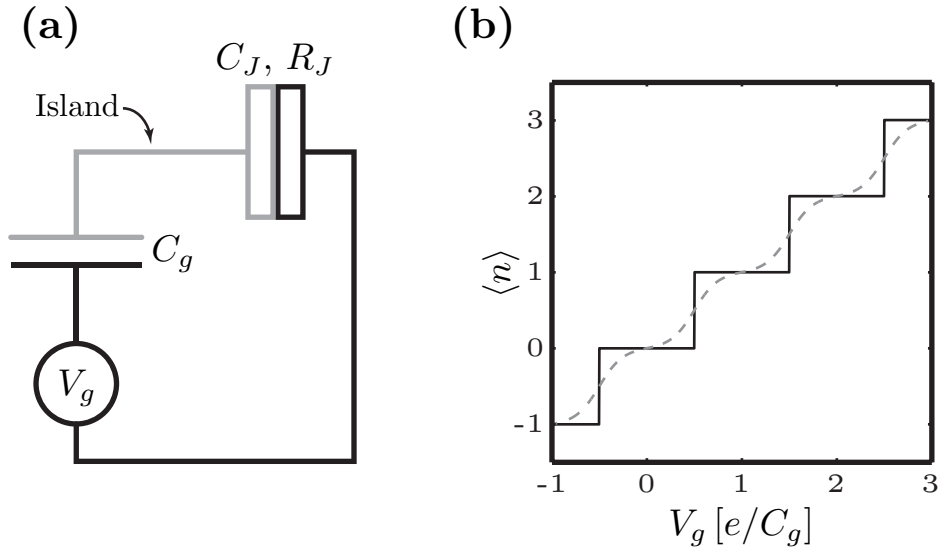


Figure 2.1: The Single-Electron Box (SEB): (a) Schematic of a SEB, with the divided rectangle representing a tunnel junction. (b) The Coulomb Staircase of electron tunneling. The solid stepwise curve shows the expected number of electrons $\langle n \rangle$ on the island at zero temperature, whereas the dashed curve shows the expectation value of n at an elevated temperature.

and $n = 2$ are degenerate.

As a result of this, the number of electrons n on the island increases stepwise with gate voltage, following the *Coulomb Staircase* shown in Fig. 2.1(b). For $Q_g = ne$, *i.e.* when the state n is maximally stable, the energy required to force an electron on or off the island is referred to as the *charging energy*, $E_C = \frac{e^2}{2C_\Sigma}$, which is an essential parameter and figure of merit for any single-electron device.

As shown in Fig. 2.1 (b), the steps between states are perfectly sharp only at zero temperature. In realistic devices, thermal fluctuations are capable of driving transitions in a region around the charge degeneracy point. If the thermal energy is increased up to and beyond the charging energy, $k_B T \gtrsim E_C$, the features of the staircase will be increasingly blurred, to the point where charging effects can finally not be detected at all. Hence, to observe and make use of single-electron phenomena, T and C_Σ must be kept as low as possible, in order to maximize the $E_C/k_B T$ ratio. A high E_C implies small device dimensions. For example, a typical charging energy of $E_C/k_B = 1$ K corresponds to a sum capacitance of $C_\Sigma = 0.9$ fF, roughly that of a metallic sphere with radius $8 \mu\text{m}$ in free space. The capacitances of junctions and the dielectric contribution from the substrate on which the device is fabricated make practical devices still a lot smaller than this. The majority of the total capacitance tends to come from the junctions, which have to be no more than a few tens of nanometers on the side for devices to work at $T \approx 1$ K.

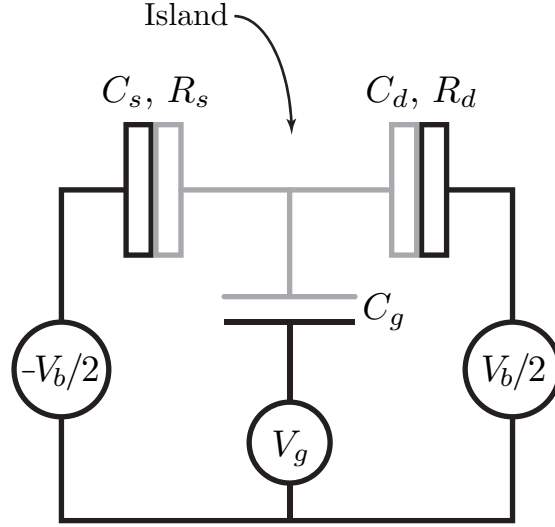


Figure 2.2: Schematic of the Single-Electron Transistor (SET). Due to the Coulomb blockade, the source-drain current is controlled by the charge $Q_g = V_g C_g$ induced on the island. Its electrical characteristics are plotted in Fig. 2.3

2.1.1 The single-electron transistor

The SEB is modified into a Single-Electron Transistor (SET) by the addition of a second junction and a second voltage source, as illustrated in Fig. 2.2. The extra junction means that a current of tunneling electrons can pass through the island, driven by the bias voltage. For the SET, the sum capacitance includes both junctions and the gate capacitance $C_\Sigma = C_s + C_d + C_g$, neglecting stray capacitances.

For $k_B T \gg E_C$ or $eV_b \gg E_C$, the tunnel current is limited by the series resistance of the junctions, whereas in the opposite limit, the dynamics are governed by charging effects in the same way as for the SEB. Just like in the SEB, the energetically optimal charge state is defined by the charge induced on the island through the gate capacitor. When two charge states (*e.g.* $n = 0$ and $n = 1$) are degenerate, a small voltage bias V_b can easily bring the state from $n = 0$ to $n = 1$ by the tunneling of an electron onto the island through the source junction, and back to $n = 0$ by tunneling of an electron out through the drain junction.

However, for $Q_g = n_0 e$, the island is neutral and the charge state $n = n_0$ stable. In order for any current to flow through the island, the charge state of the island must change, *i.e.* either the transition $n \rightarrow n + 1$ or $n \rightarrow n - 1$ must be energetically favorable. This is only the case if the voltage over any of the junctions is at least E_C/e , assuming zero temperature. For junctions with equal capacitances, the bias voltage divides equally between the two, so the threshold for tunneling to occur is $V_b > 2E_C/e$. Once the system is able to depart from the stable state $n = n_0$, *e.g.* by an electron entering the island, the subsequent process of an electron tunneling out of the island through the other junction is commanded, so a continuous current can flow. At values of Q_g corresponding to intermediates between stable and degenerate charge states, the threshold voltage changes linearly with Q_g , producing the characteristic diamond plot shown in Fig. 2.3.

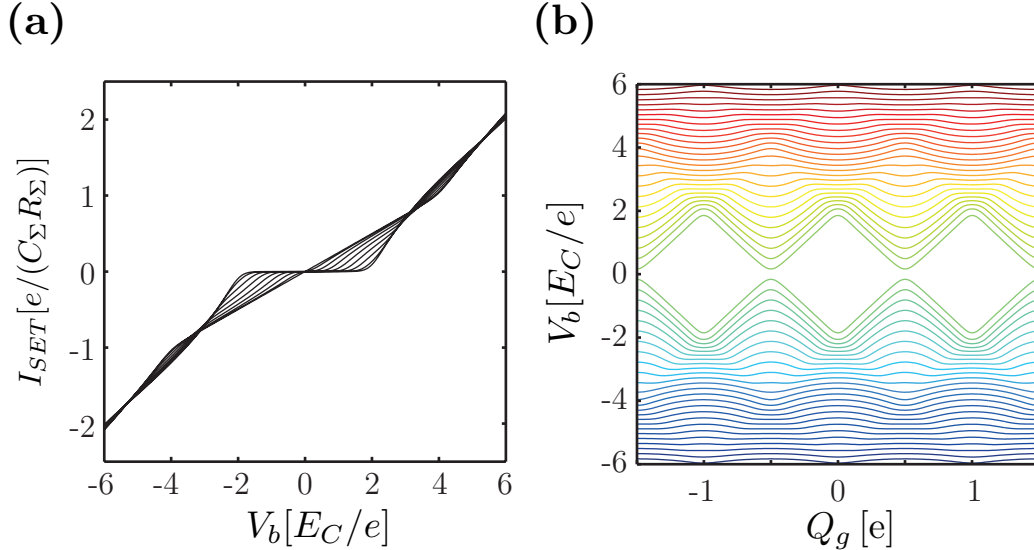


Figure 2.3: Characteristics of a symmetric SET in the normal-conducting state. (a) $I - V$ characteristics for several values of Q_g . (b) Stability diagram of the same SET. Each curve represents a fixed value of the SET current I_{SET} . Inside the diamonds, the suppression of current is exponential in V_b .

The modulation of I_{SET} with Q_g makes the SET useful as an electrometer, sensitive to small changes in the charge induced on its island. Throughout this thesis, Q_g is used to denote induced charge on the island in general, not only through a gate capacitor.

For an SET with asymmetric junction capacitances, the bias voltage falls more strongly over one of the junctions, producing a slant to the diamonds, and at temperatures above zero, the electrical characteristics of the SET become rounded just as for the SEB. For high values of V_b and T , more than two charge states at a time may be accessible. To predict the full DC behavior of the SET, one needs to consider all states that can be accessed, and determine the rates of moving between them. The rate of tunneling between two charge states can be derived from Fermi's Golden Rule as

$$\Gamma = \frac{-\Delta E}{e^2 R_J [1 - \exp(\Delta E/k_B T)]} \quad (2.1)$$

Here, ΔE is the difference in electrostatic energy between the initial and final state, with negative values denoting energetically favorable events. The occupation probabilities for a charge state n is given by the Master Equation

$$\delta P_n / \delta t = \sum_{m \neq n} [\Gamma_{m \rightarrow n} P_m(t) - \Gamma_{n \rightarrow m} P_n(t)] \quad (2.2)$$

which can be solved self-consistently for all values of n in the limit of steady-state current, $\delta P_n / \delta t = 0$. If there are multiple junctions in the system, the rate $\Gamma_{m \rightarrow n}$ must include all tunneling transitions that bring the charge state from m to n . This approach is valid also for circuits with more than one island, if the charge states are generalized to several dimensions, *e.g.* $n = [n_1, n_2]$ for a system of two coupled islands.

Solving the Master Equation translates to a fast matrix inversion once the transition rates have been calculated, which is usually done numerically [9]. As part of the work on Resistive Electron Pumps (Ch. 6), the author developed such a Master Equation simulator for arbitrary networks of tunnel junctions and capacitors, along with an equivalent version based on a Monte Carlo method. Both simulators included support for Photon Assisted Tunneling processes. For the curve-fitting procedures in Ch. 4, Göran Johansson implemented an SET simulator using the Master Equation, which self-consistently takes into account the temperature increase of the SET island due to the tunneling current.

The calculations outlined above represent the *Orthodox Theory* of the Coulomb blockade [1, 12–14]. For more precise calculations, additional high-order electron transport channels should be accounted for. These include *co-tunneling*, whereby one electron tunnels onto the island and one tunnels off simultaneously; *Photon-assisted tunneling*, where tunneling events are aided by energy absorbed from high-frequency electric fields; and for the case of superconductive devices and superconducting-normal hybrids, *Andreev tunneling*. These higher-order processes are discussed further in the chapter about metrological charge pumping (Ch. 6).

2.1.2 Power dissipation in the SET

When operated as an electrometer, the SET is typically biased at $V_b \approx 2E_C/e$, *i.e.* at the threshold voltage for tunneling under maximal Coulomb blockade. For an aluminum device with high charging energy, E_C/k_B can be as high as 10 K, which implies a bias voltage of $V_b > 1.7$ mV. For junctions with resistance $R_s + R_d = 50$ k Ω , this computes to a total power dissipation of 30 pW. To a good approximation, half of this power ends up on the SET island, $P_{SET} = V_b I_{SET}/2$.

For a large conductor at high temperature, the conduction electrons can usually be considered fully thermalized with the ionic lattice, but in the opposite regime – where single-electron devices are usually operated – this is not necessarily the case. An electron entering the island of an SET under strong voltage bias initially has an energy above the Fermi level of the island electrons. The excited electron relaxes quickly, dissipating its energy to the electron gas of the island. This process is typically fast enough on the time scale of the tunneling rate that the electron gas can always be considered uniform and Fermi-distributed, although exceptions to this have been shown and studied [15, 16].

The heat added to the electron gas of the island can then be further dissipated by three processes:

1. Preferential tunneling of electrons removed from the Fermi energy (depletion of hot electrons and injection of cold ones).
2. Emission of photons to the surrounding circuit.
3. Excitation of mechanical modes in the lattice of the island and surrounding matter, *i.e.* phonon thermalization.

Preferential tunneling can be accounted for in the Orthodox model of tunneling, and only has an impact at very low temperatures [17, 18]. Thermalization through photon emission is usually treated as secondary, although the argument has been presented that it can play a more profound role at very low temperature [19]. The third process, thermalization of the electron gas with phonons, is generally the dominant one in SETs. This has been studied in great detail both theoretically and experimentally [15, 17, 20–22]. By the most common

model, where the island electrons are assumed to thermalize with phonons in three dimensions, the flow of thermal energy is given by

$$P_{e-ph} = \Sigma\Omega(T_e^n - T_{ph}^n) \quad (2.3)$$

with $n \approx 5$, where T_e is the electron temperature, T_{ph} the phonon temperature, Σ a material-dependent electron-phonon scattering parameter, and Ω the volume where the thermalization takes place, in this case the metal of the SET island. This thermalization rate can usually be considered the limiting factor in cooling the island electron gas. Some authors have also considered a phonon interface resistance (Kapitza barrier) between the SET island and the substrate [17]. However, due to the small size of the typical SET island, it cannot be regarded as a separate phonon bath at the lowest temperatures – where the phonon wavelengths exceed its dimensions – and one should instead consider the electron gas as thermalizing directly to the coupled mechanical system of the SET and the substrate [23, 24]. Taking into account the device geometry can lead to modifications to Eq. 2.3 [25, 26]. In particular, the thermalization power should in theory scale as $P \propto T^6 \log T$ for a thin film on a flat substrate [26]. Nonetheless, the experimental evidence for Eq. 2.3 with $n \approx 5$ is strong [22, 24, 27–29].

Requiring equilibrium between the power P_{SET} dissipated by the tunneling current and that removed by phonons, and assuming $T_{ph} \approx 0$, we have a fifth root dependence of T_e on both the dissipated power and the pre-factors of Eq. 2.3. This weak dependence means that SETs operating under normal cryogenic conditions usually have a similar range of island electron temperatures (around a few hundred millikelvin) even if the device parameters are very different.

In Paper II, the use of an SET with high charging energy allows us to maintain charge sensitivity while tuning the power dissipation over a relatively wide range. This allows us to study how the temperatures of the SET electron gas and the local substrate phonons relate to the level of charge noise coupling to the SET.

2.1.3 Noise in SETs

Since the current-carrying electrons tunnel stochastically through an SET, it will always be subject to a certain amount of *shot noise*, essentially a jitter in the timing between tunneling events. Due to the asymmetry between incoming and outgoing tunneling rates, the noise spectrum will have a small dependence on Q_g , but to a good approximation it has a uniform spectral power of

$$S_{I,shot} = 2F\langle I_{SET} \rangle e \quad (2.4)$$

up to a cut-off frequency set by the tunneling rates [30–32]. Here, F is the Fano factor, which is a measure of the correlation between tunneling events. In a blockaded SET at low temperature, tunneling events are sequential and correlated, so each tunneling event onto the island is rapidly followed by a tunneling event off the island, corresponding to $F = 1$. When the Coulomb blockade is lifted or the temperature increased sufficiently that incoming electrons and outgoing ones are no longer correlated, the Fano factor drops to $F = 1/2$.

The shot noise sets the fundamental bound on the sensitivity of aluminum SETs to $\delta Q \approx 1 \mu e / \sqrt{\text{Hz}}$ [3, 30, 33]. Since the potential of the island fluctuates with the charge state, the shot noise also puts a lower bound on the back-action exerted by the SET on the system being measured [34], see Sec. 3.5. In practical SET setups to date, amplifier noise dominates over the shot noise, although the opposite situation has been approached [3, 31, 35].

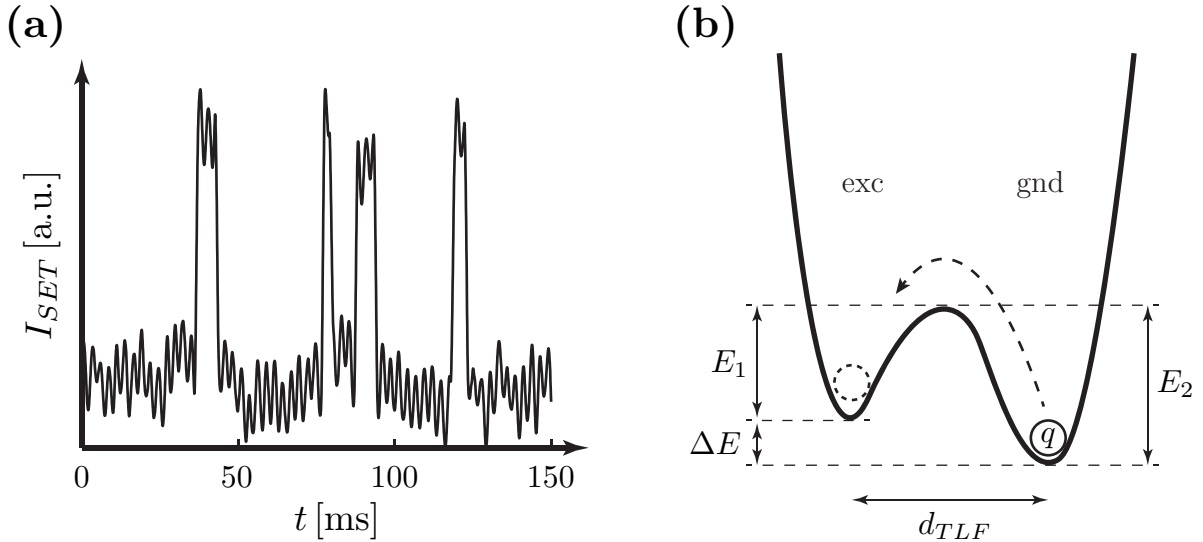


Figure 2.4: Two Level (charge) Fluctuator (TLF): **(a)** Telegraph signal observed in an SET. The fast oscillation is a “pilot” signal applied to the SET gate at $f_p = 377$ Hz (see Ch. 4). **(b)** Schematic of a TLF, after [36]. The particle with charge q moves stochastically between the two potential wells, separated by a distance d_{TLF} . The energies E_1 and E_2 are required for classical activation, *i.e.* over the barrier, between the ground state and the excited state.

At low frequencies, the sensitivity of an SET is typically limited by charge noise with a spectrum of $S_Q \propto 1/f^\alpha$, with $\alpha \approx 1$. Apart from its impact on SETs [37, 38], this noise causes decoherence in qubits [39–42] and has been suggested to be a dominant error source in single-electron pumps [43, 44].

In time domain measurements of SETs, it is often possible to discern a telegraph signal, as shown in Fig. 2.4(a), where the induced charge on the island switches stochastically between two values. In the frequency domain, such a signal produces a Lorentzian-shaped spectrum [45].

$$S_x(\omega) = \frac{\Gamma_\uparrow \Gamma_\downarrow}{\omega_0} \frac{1}{\omega + \omega_0^2} \quad (2.5)$$

Here, Γ_\uparrow and Γ_\downarrow are the characteristic switching rates between the two states, which set the Lorentzian cut-off frequency

$$\omega_0 = 2\pi(\Gamma_\uparrow + \Gamma_\downarrow) \quad (2.6)$$

The $1/f$ character of the noise arises from an ensemble of weak Lorentzian contributions with different ω_0 [46, 47].

Each telegraph signal is typically modeled as a charged particle moving between two adjacent potential wells, either by quantum mechanical tunneling or due to thermal activation. Such a system is referred to as a Two-Level Fluctuator or TLF, illustrated in Fig. 2.4 (b). Many studies have been conducted, of $1/f$ -shaped charge noise [36, 37, 48–55] as well as individual fluctuators [56–60]. Yet, no general agreement has been achieved on the microscopic nature and location of the TLFs, or even whether there is more than one type.

A particular point of dispute is whether the TLFs are located in the barriers of the tunnel junctions, in the substrate, or in interface layers between different materials. The main argument for locating the TLFs to the tunnel barriers are that a short distance between the potential wells is sufficient to strongly affect the SET, whereas a particle with the same charge would have to move a distance orders of magnitude longer to produce the same response if it was located in the substrate¹ [48].

On the other hand, correlation measurements between two adjacent SETs indicate that at least some of the TLFs are located in the substrate, where they can couple to both SETs [38, 58]. Zimmerman *et al.* [56] also argue against the TLFs sitting in the junction barriers, based on an experiment where the noise level depended monotonously on an external gate voltage over a range much wider than the periodicity of the junction voltage. Measurements on SETs with small contact area between the island and the substrate have shown a reduction in the noise [54, 62]. However, the charge noise measured in a fully suspended SET was not found to be much lower than in equivalent devices with an intact substrate [51]. This was attributed to self-heating of the SET, in agreement with our findings which are discussed further in Ch. 4 and Paper II .

The standard model by Dutta and Horn [46] describes each TLF as having a single activation energy ΔE , required to bring the TLF from one state to the other. Assuming that the transitions are thermally activated, this gives rise to an $1/f$ spectrum if the activation energies for the ensemble of TLFs are uniformly distributed. This also gives a linear dependence of the noise power with temperature. However, this simplified model was originally intended to describe resistance fluctuations, where a charge carrier in an otherwise conductive material may get trapped by a local defect, only to be released again some time later [63].

For a TLF like the one shown in Fig. 2.4(b), there are two activation energies governing the dynamics, one for each direction of switching, which is also seen in the telegraph noise [Fig. 2.4(a)] as a difference between Γ_{\uparrow} and Γ_{\downarrow} . This was treated in Refs. [36] and [57], which predicted that the noise should scale as $S_Q \propto T^2$ in this case. Such a dependence was found experimentally by these authors, and also in Ref. [55]. However, our measurements disagree with this, showing a clear $S_Q \propto T$ scaling for all measured SETs. This should be the case if the TLFs are in thermal equilibrium and switch state by quantum tunneling. The implications of our results on the description of TLFs are discussed further in Ch. 4.

2.1.4 Radio-frequency SET read-out

Due to the requirement that electrons must be localized to either side of each tunnel junction, an SET fundamentally has a high resistance, which limits the measurement speed unless special techniques are used. The fact that it must operate at low temperature further aggravates the problem, since the long wires required in cryogenic systems have high capacitances, typically limiting the measurement bandwidth to a few kilohertz.

Initial attempts to improve the measurement speed used High Electron Mobility Transistor (HEMT) amplifiers on the same chip as the SET, which increased the bandwidth up to 700 kHz, although with some additional issues of device heating [64, 65]. The major breakthrough

¹The charge induced on the SET by a point charge can be found by solving the electrostatic Poisson equation with unity potential applied to the SET island and all other electrodes grounded. The calculated potential at any point in space is then equivalent to the charge that would be induced on the island if a unit charge was placed in that point. The coupling strength of a TLF moving a distance \vec{d}_{TLF} is given by $\vec{d}_{TLF} \cdot \vec{E}$, where \vec{E} is the electric field from the electrostatic solution. This approach is described in Ref. [61].

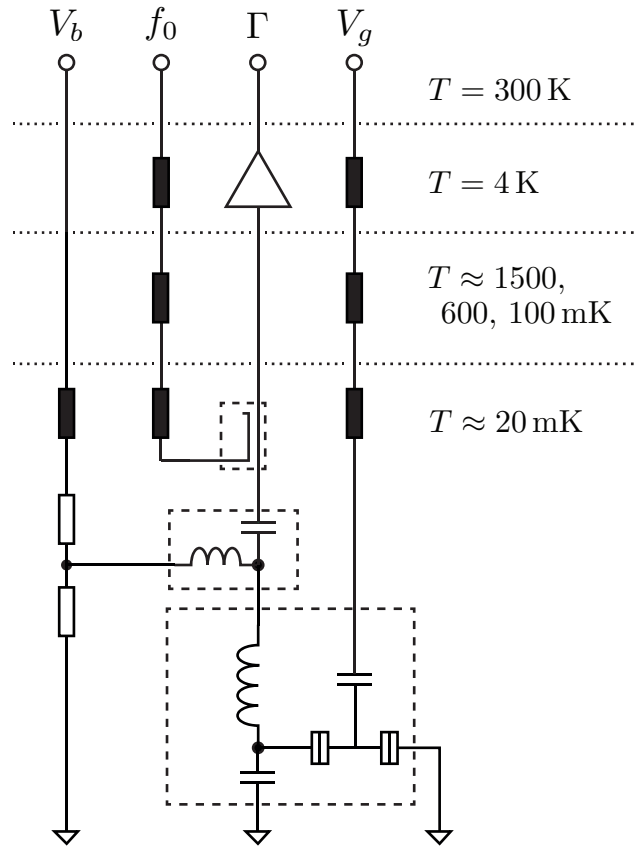


Figure 2.5: Schematic of an RF-SET measurement setup. A directional coupler (or a circulator) is used to feeds an RF signal at frequency f_0 toward the sample (upper dashed box). The RF signal passes a bias tee (middle dashed box) before it reaches the tank circuit with the embedded SET (lower dashed box). The reflected signal goes up through the same transmission line to a HEMT amplifier at $T = 4$ K. The black boxes represent attenuators and filters, intended to prevent radiation from higher temperature stages from reaching the SET. The white boxes are resistors which form a voltage divider to bias the SET. Alternatively, a well-filtered line can be brought from room temperature directly to the bias tee, to allow DC measurements on the SET.

came with the invention of the RF-SET, *i.e.* the efficient read-out out of an SET by means of RF reflectometry [66]. In the RF measurement mode, a signal with a typical frequency of $f_0 = \omega_0/2\pi = 300$ MHz to 1 GHz is launched through a transmission line towards a resonant LC circuit (or “tank circuit”) where the SET is embedded, as shown within the lower dashed box of Fig. 2.5. The tank circuit transforms the minimal resistance of the SET from the range of ~ 100 k Ω to the impedance of the transmission line, usually $Z_0 = 50$ Ω . The amount of dissipation, and hence the total circuit impedance, depends on the differential resistance $R_{SET}(V_b, Q_g) = dI_{SET}/dV_b$ of the SET around the bias point V_b .

Without the SET, the impedance of the LC circuit is $Z_{LC} = \sqrt{\frac{L}{C}}$ on resonance. With the resistance R_{SET} of the SET included, the total impedance is

$$Z_{LCR} = j\omega L + \frac{R_{SET}}{1 + j\omega R_{SET}C} \quad . \quad (2.7)$$

Resonance occurs when the imaginary part of Z_{LCR} is zero, for

$$\omega = \omega_0 \equiv \sqrt{\frac{1}{LC} - \frac{1}{R_{SET}^2 C^2}} \approx \frac{1}{\sqrt{LC}} \quad . \quad (2.8)$$

The last approximation is valid in practical circuits since $R_{SET} \gg Z_{LC}$, *i.e.* $R_{SET}^2 C^2 \gg LC$. The tank circuit impedance on resonance then becomes

$$Z_{LCR}(\omega_0) = \frac{L}{R_{SET}C} \quad (2.9)$$

and the reflection coefficient in linear (voltage) units is

$$\Gamma = \frac{Z_{LCR} - Z_0}{Z_{LCR} + Z_0} \quad . \quad (2.10)$$

The tank circuit can in principle be either over-coupled ($Z_{LCR} < Z_0$) or under-coupled ($Z_{LCR} > Z_0$), but it is technically undesirable to cross the point of optimal circuit matching during operation, since this makes the acquired data hard to interpret. The measurements presented in this thesis all use an over-coupled circuit. The highest dynamic range is then reached when the minimal achievable value of R_{SET} results in Z_{LCR} approaching Z_0 , which results in maximal dissipation and minimal reflection. When the SET is in the maximally Coulomb-blockaded state, R_{SET} is close to infinite so the circuit fully reflects the carrier signal back into the transmission line.

There is a trade-off between the dynamic range and the measurement bandwidth, set by the quality factor of the tank circuit. For a general resonant system, the quality factor is defined as

$$Q = \omega_0 \frac{E}{P} \quad (2.11)$$

where E is the energy stored and P the power loss, evaluated on resonance. In the tank circuit, all the energy resides in the inductor at the point in the cycle when the current is at its maximum:

$$E = I^2 L / 2 \quad . \quad (2.12)$$

With the SET absent, power is lost from the circuit only to the source impedance Z_0 ,

$$P_{ext} = I^2 Z_0 / 2 \quad (2.13)$$

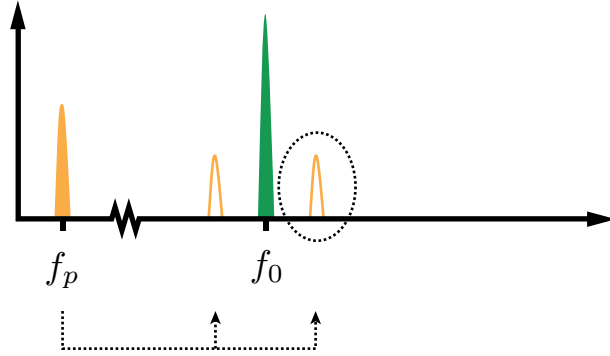


Figure 2.6: RF-SET frequencies: The charge signal at frequency f_p , typically applied through a gate capacitor, amplitude-modulates the carrier signal applied over the SET junctions at f_0 . f_p then shows up as two side-bands to f_0 in the reflected spectrum.

which gives the *external* quality factor

$$Q_{ext} = \frac{E}{P_{ext}} = \omega_0 \frac{L}{Z_0} = \frac{Z_{LC}}{Z_0} . \quad (2.14)$$

For $R_{SET} \gg Z_{LC}$, the dissipation in the SET on resonance is

$$P_{int} = \frac{I^2 L}{2R_{SET} C} \quad (2.15)$$

which gives the *internal* quality factor

$$Q_{int} = \frac{E}{P_{int}} = \omega_0 R_{SET} C = \frac{R_{SET}}{Z_{LC}} . \quad (2.16)$$

The total quality factor is

$$Q_{tot} = \frac{1}{1/Q_{int} + 1/Q_{ext}} \quad (2.17)$$

which gives the measurement bandwidth

$$BW = \frac{\omega_0}{2\pi Q_{tot}} . \quad (2.18)$$

In practice, C is a combination of self-capacitance of the coil, the bonding wire and the pad capacitance. The inductance L can either be fabricated on the same chip as the SET or, as in all experiments presented here, be a coil etched on a separate circuit board. A photograph that includes such an RF coil is shown in Fig. 2.13. The RF carrier signal is generally applied through a series of cryogenic filters and attenuators distributed throughout the fridge, in order to remove thermal noise from temperature stages higher than the lowest one. The signal couples to the tank circuit via a bias-tee through which the bias voltage V_b is applied, and through a directional coupler or a circulator. The latter circuit elements separate the applied

carrier signal from that reflected from the tank circuit. Circulators have the additional advantage of protecting the SET from noise radiated by the subsequent amplifier. For high-fidelity measurements, the amplifier is usually based on HEMTs operating under cryogenic conditions, and hence placed inside the refrigerator, typically at the 4K temperature stage. The experiments presented in this thesis all used a cryogenic HEMT amplifier optimized for operation at $\omega_0/2\pi = 350$ MHz, with subsequent amplification at room temperature. This amplifier dominated the total system noise, which was as best measured to a noise temperature² of $T_N \approx 11$ K.

Fig. 2.5 shows a schematic of an RF-SET measurement setup. For further discussion about cryogenic measurements, see Sec. 2.3.

The charge sensitivity of the RF-SET is measured by applying a ‘‘pilot’’ tone of known charge amplitude Q_p to the gate, typically at several hundred kHz. This tone is seen in the frequency domain as a pair of side-peaks around the carrier frequency, and the sensitivity is given by

$$\delta Q = \frac{Q_p}{\sqrt{2} RBW 10^{SNR_{dB}/20}} \quad (2.19)$$

where RBW is the resolution bandwidth and SNR_{dB} is the signal-to-noise ratio in decibel. The factor $\sqrt{2}$ in the denominator stems from the fact that only one side band is monitored, whereas the information in both of them could in principle be used for better SNR. The record sensitivity is $0.9 \mu\text{eHz}^{-1/2}$ [3], and values around $10 \mu\text{e}/\sqrt{\text{Hz}}$ can be achieved routinely.

2.1.5 The SET as an intrinsic GHz mixer

With the RF approach to SET read-out, a bandwidth of $BW_{meas} \approx 10$ MHz can typically be achieved. This limit is set by the tank circuit; the intrinsic speed of the SET is limited only by the tunneling rate, $f_{SET} \approx 1/(2\pi R_J C_\Sigma) \approx 10$ GHz [67].

In the RF-SET measurement scheme the SET is used as a frequency mixer between an RF signal applied across the junctions and charge signals induced on the island at low frequency. As shown in Ref. [68], it is also possible to use the strongly non-linear nature of the charge transfer function to mix two different charge signals that couple to the SET gate. The SET still has to be read out at the rate imposed by the measurement circuit, be that RF or DC, but the available bandwidth can be centered around any frequency up to f_{SET} .

To a first approximation, the transfer function of the SET can be considered sinusoidal:

$$\Gamma_0 \propto \sin(2\pi Q_g/e) \quad . \quad (2.20)$$

When the charge induced on the SET consists of one slow component and one component at high frequency, $Q_g = Q_{DC} + Q_{RF} \sin(2\pi f_{RF}t)$ with $BW_{meas} \ll f_{RF} < BW_{SET}$, the response observed through the read-out circuit as a function of Q_{DC} is smeared (time-averaged over the RF period $\tau = 1/f_{RF}$) by the RF signal:

$$\Gamma(Q_{DC}) = \frac{1}{\tau} \int_0^\tau \Gamma_0(Q_{DC} + Q_{RF} \sin(2\pi f_{RF}t)) dt \quad . \quad (2.21)$$

²The noise temperature T_N is defined as the temperature of a matched (50Ω) resistor on the amplifier input producing the same noise power as the amplifier adds.

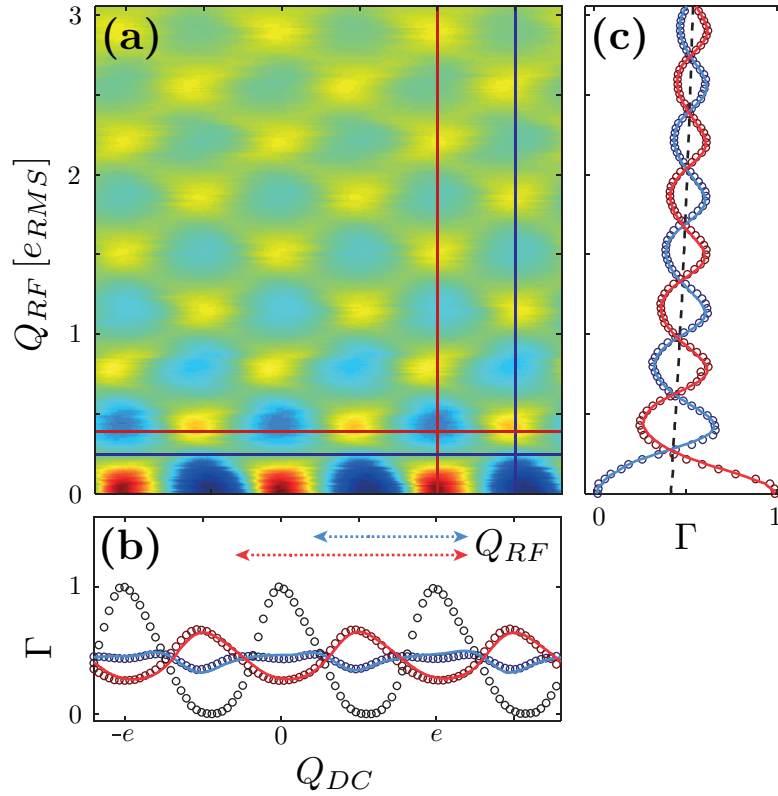


Figure 2.7: An example of smeared SET modulation functions by a charge signal Q_{RF} at high frequency, as a function of its amplitude and the quasi-static charge Q_{DC} induced on the island. The color map (a) is an experimental data set, with Q_{RF} induced by a surface acoustic wave passing underneath the SET on a piezoelectric substrate. The cross-sections along the horizontal and vertical lines are plotted as circles in panels (b) and (c), respectively, and the correspondingly colored solid lines represent a fit to Eq. 2.23, after compensation for the slope shown with a dashed line in (c). The charge modulation Γ_0 in the absence of RF signal is plotted with black circles in (b), and the SET response Γ is normalized so that this curve fits within a $[0, 1]$ interval.

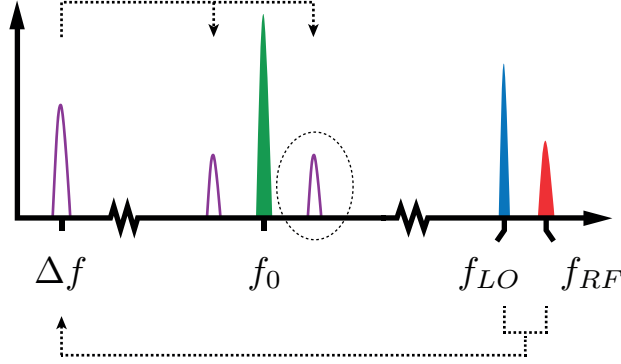


Figure 2.8: Intrinsic mixing in the SET. A high-frequency charge signal at f_{RF} is mixed with a local oscillator signal applied through the SET gate at f_{LO} . The resulting down-converted signal is within the bandwidth of the RF-SET tank circuit and is detected as usual (see Fig. 2.6). For $f_{LO} = f_{RF}$, the mixing is homodyne and depends on the relative phase between f_{RF} and f_{LO} , otherwise heterodyne.

As calculated in Ref. [68], the sinusoidal transfer function of Eq. 2.20 is modulated by a Bessel function of 0:th order in the amplitude of the RF signal:

$$\Gamma(Q_{DC}, Q_{RF}) = J_0\left(2\pi\frac{Q_{RF}}{e}\right) \Gamma_0(Q_{DC}) dt \quad . \quad (2.22)$$

For a general periodic transfer function, each component of its Fourier transform is similarly weighted with a Bessel function:

$$\begin{aligned} \Gamma_0(Q_g) &= \sum_{k=-\infty}^{\infty} c_k e^{2\pi k i \frac{Q_g}{e}} \\ \implies \\ \Gamma(Q_{DC}, Q_{RF}) &= \sum_{k=-\infty}^{\infty} J_0\left(2\pi k \frac{Q_{RF}}{e}\right) c_k e^{2\pi k i \frac{Q_{DC}}{e}} \quad . \end{aligned} \quad (2.23)$$

Eq. 2.23 is illustrated in Fig. 2.7. Due to the Bessel function modulation, the measured SET response is influenced by the high-frequency Q_{RF} , but since $d\Gamma/dQ_{RF}$ is low for low values of Q_{RF} , the sensitivity is limited. This can be improved by applying an additional signal Q_{LO} to the gate at $f_{LO} = f_{RF}$, either in phase or in counterphase with Q_{RF} . This effectively shifts the signal up to the point of maximal $d\Gamma/dQ_{RF}$, a method is known as *homodyne mixing*.

Alternatively, Q_{LO} and Q_{RF} can be applied at different frequencies. The instantaneous SET gain with respect to Q_{RF} is then a function of Q_{LO} , so the latter amplitude-modulates the former. In the time domain, this is equivalent to a multiplication of the two signals, and in the frequency domain, the result is one component at $f_{LO} - f_{RF}$ and another one at $f_{LO} + f_{RF}$. Both the sum and the difference component are proportional to Q_{RF} , and

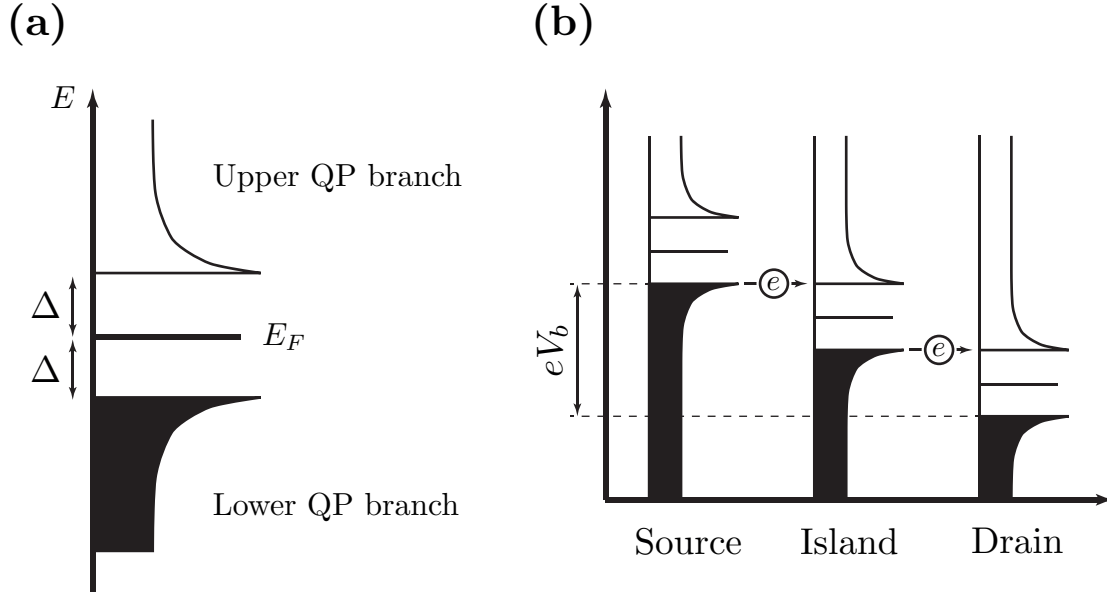


Figure 2.9: Superconductor Density of states (DOS): (a) The two Quasiparticle (QP) branches are separated from the Fermi energy E_F by the gap energy Δ , and have peaked DOS at their onsets. (b) Line-up of the energy bands at the onset of QP current in a superconducting SET. In addition to the bias voltage required to align the QP branches, enough energy must be supplied from the bias to overcome the Coulomb blockade.

if the difference frequency fits within the read-out bandwidth, it can be detected. The sum frequency component is generally far away from the measurement band, reducing the signal-to-noise ratio by a factor of at least $\sqrt{2}$ compared to if the signal to be detected had been applied to the gate directly at $f_{LO} - f_{RF}$. Fig. 2.8 shows the various frequency components involved when an RF-SET is used as an intrinsic heterodyne mixer.

Since f_{LO} can be adjusted arbitrarily, this technique allows the measurement bandwidth to be centered at an arbitrary frequency, as long as it stays lower than f_{SET} . This type of intrinsic SET mixing, both homodyne and heterodyne, is employed to the study of high-frequency surface acoustic waves described in Ch. 3.

2.1.6 Superconductivity

So far, the descriptions of single-electron devices have assumed that they are made of normal-state metals, as opposed to superconductors. Due to the low temperature where the devices are usually operated, effects of superconductivity come naturally, especially since the material of choice for tunnel junctions is oxidized Al, and Al has a superconducting transition temperature of $T_C \approx 1.2$ K. When normal-state operation is desired below the transition temperatures of the materials, superconductivity can be quenched with a strong magnetic field.

In the transition from normal metal to superconductor, as described by the BCS theory [69–71], conduction electrons within a material- and temperature-dependent energy interval

around the Fermi energy E_F couple two-by-two into Cooper pairs. The pairs are bosonic and condensate to a common energy ground state, leaving an energy gap without states around E_F . The resulting Density of states (DOS) is often represented as in Fig. 2.9(a), with two Quasiparticle (QP) branches, each separated from a Cooper pair (CP) branch by the gap energy Δ . For practical purposes, QPs can usually be thought of as electrons and holes just as in normal conductors and semiconductors, and the QP branches as reservoirs for such carriers, although with a special shape to their DOS.

In a superconducting SET (S-SET) [72–74] around zero bias voltage, the Fermi levels of the leads and the island align, and can in some cases allow a current of Cooper pairs to flow. This current can be subject to Coulomb blockade, with a periodicity of $2e$ in Q_g as opposed to e for normal-state electrons and QPs. This effect is, however, usually weak, and unless back-action is an issue, the S-SET is more often operated with a current of QPs. The flow of QPs is suppressed until the bias voltage is sufficient to align the upper and lower QP branches at both the source and the drain junction, *i.e.* at $V_b = \pm 4\Delta/e$, in addition to the voltage required to overcome the Coulomb blockade. This is illustrated in Fig. 2.9(b). Apart from pure CP and QP currents, charge transport involving both types of charge carriers can take place at a few specific combinations of V_b and Q_g , known as the Josephson-Quasiparticle Peak (JQP) and the Double-JQP. The sharpness of these peaks with respect to Q_g makes them suitable for sensitive SET electrometry, although in the presence of $1/f$ noise it can be difficult to maintain the gate bias at a sensitive point.

While the same SET can work as an electrometer in either the normal or the superconducting state, other related devices fundamentally rely on superconductivity for their operation. One example is the superconducting charge qubit, another one the SINIS turnstile, both of which make use of the superconducting gap separating the CP and QP branches, but in different ways: The charge qubit makes use of coherent CP tunneling, and gets “poisoned” by QP excitations, whereas the SINIS turnstile transports QPs one by one and suffers from errors due to their intermingling with Cooper pairs. In both cases, problems arise when reality deviates from the ideal BCS model, which says that the QP branches are free from non-thermal excitations and there are no states available within the BCS gap. Sub-gap states are often observed in practical devices and were described theoretically by Dynes *et al.* [75, 76]. It has recently been suggested that the Dynes DOS is in fact not inherent to the materials, but generated by external high-frequency photons [77].

2.2 Surface acoustic waves

Surface Acoustic Waves (SAW) are mechanical waves that propagate on the surface of a solid, first described by Lord Rayleigh [78]. There are several varieties of SAW in addition to the one described by Rayleigh, including Love waves, which have a component of motion perpendicular to the plane spanned by the surface normal and the direction of propagation, and Leaky SAW, which continuously loses some of its power into the bulk of the solid. Throughout this thesis and Paper I, we use a coordinate system where \hat{x} aligns with the direction of SAW propagation, \hat{y} aligns with the SAW wavefront, and \hat{z} is normal to the substrate surface.

Here, we are concerned with pure Rayleigh waves, where a point on the surface makes an elliptical orbit in the $(x - z)$ plane, moving along with the propagation direction of the wave propagation when it is at its lowest point of the trajectory and vice versa. This direction of motion is the opposite to that of deep-water waves, but there is otherwise a visual resemblance between the two. An artistic interpretation of SAW is shown in the cover of this thesis.

A crucial feature of Rayleigh waves is that they propagate immediately at the chip surface, extending only about a wavelength into the substrate, and dissipate very little power in the form of bulk waves or other mechanical excitations. The speed of propagation is determined by material properties, virtually independent of frequency.

On the microscopic scale, SAW can be produced artificially, typically on the surface of a chip made of a piezoelectric material. The piezoelectricity is utilized to convert electrical power into mechanical and vice versa, which allows SAW-based components to be used as electrical circuit elements. Such components are used extensively for signal processing in the RF and microwave frequency ranges, in the shapes of filters, resonators and delay lines, and recently also in mass-produced identification transponders (RFID) [79]. The theory and applications of SAW are covered in several textbooks [80–84].

Apart from the polished piezoelectric surface which carries the wave, the most essential element in a SAW device is the Interdigital Transducer (IDT). In its simplest form, it consists of two electrodes deposited on the surface, with long parallel fingers interspersed as in Fig. 2.10. IDTs can also be designed with more advanced features than those treated here, *e.g.* to shape the pulse response or produce directed SAW beams. For commercial construction of SAW devices, advanced simulation tools are employed, based on first-principles Finite-Element Method (FEM) and Coupling-Of-Modes (COM) theory. However, we use the model described by Datta [80], which is relatively simple and physically intuitive. We only treat the simplest kind of IDT, which is bi-directional and unapodized, and has a metallization ratio of $\eta = 50\%$, *i.e.* finger widths equal to the distance between fingers.

With a potential applied to an individual IDT finger, the electric field generates strain at the substrate surface. For an AC potential, a wave of strain is produced which propagates acoustically away from the finger in both directions on the surface. The wavelength is given by

$$\lambda = v_{SAW}/f \quad (2.24)$$

where $f = \omega/2\pi$ is the frequency of the applied AC voltage and v_{SAW} is the speed of SAW propagation. An IDT with many fingers spaced by $\lambda_0/2$ resonates at $f_0 = v_{SAW}/\lambda_0$, where the contributions from all fingers add in phase and the strongest SAW beam is emitted.

The amplitude of the SAW is defined by its surface potential ϕ , given as a complex phasor. Denoting waves moving in the positive and negative direction by ϕ^+ and ϕ^- , respectively, the

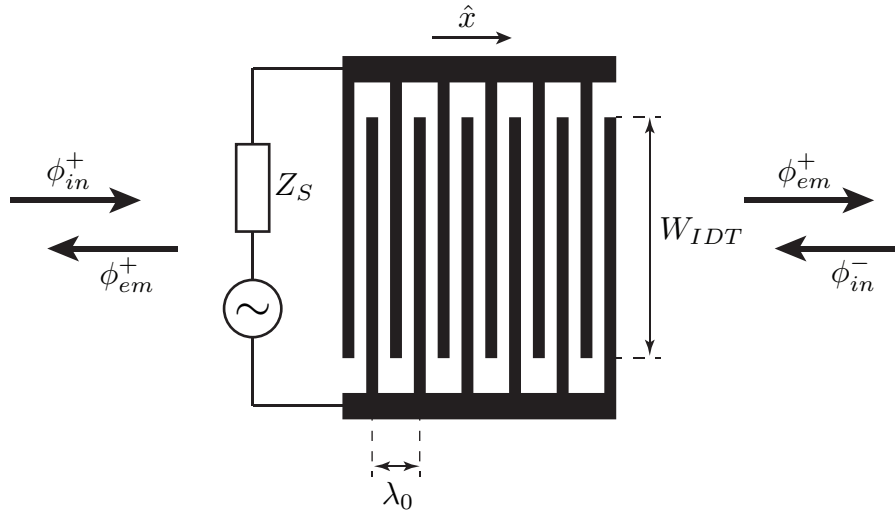


Figure 2.10: Top view of an Interdigital Transducer (IDT). The periodicity λ_0 of the fingers sets the IDT resonance frequency to $f_0 = v_{SAW}/\lambda_0$, and the sharpness of the resonance increases with the number of finger pairs N_{IDT} . The width W_{IDT} of the finger overlap determines the width of the emitted SAW beam, and thereby the power carried for a given SAW amplitude. An IDT of this simple construction emits SAW equally in both directions when driven electrically. The arrows illustrate the complex amplitudes of incoming and generated SAW.

instantaneous potentials at a position x and a time t are

$$\phi_{inst}^+ = \text{Re} \left(\phi^+ e^{2\pi i [x/\lambda - ft]} \right) \quad (2.25)$$

$$\phi_{inst}^- = \text{Re} \left(\phi^- e^{2\pi i [x/\lambda + ft]} \right) \quad (2.26)$$

with x defined with respect to some common reference point.

The description of the SAW beam uses a conductance Y_{SAW} which is defined so that the SAW carries a power

$$P_{SAW} = |\phi|^2 Y_{SAW} \quad . \quad (2.27)$$

P_{SAW} increases proportionally with the width of the SAW beam, set by the finger overlap W_{IDT} of the IDT, and in inverse proportion to the wavelength λ . Hence, we can define a characteristic SAW conductance y_{SAW} that depends only on the properties of the material and the chosen crystal cut:

$$y_{SAW} = \frac{\lambda Y_{SAW}}{W_{IDT}} \quad (2.28)$$

This can be expressed in terms of underlying material properties as

$$y_{SAW} = \frac{2\pi C_S v_{SAW}}{K^2} \quad (2.29)$$

Eq. 2.29 is derived in Datta, based on the definition of the electro-mechanical coupling coefficient K^2 of the material. C_S is an equivalent dielectric constant, equal to the capacitance per unit length for a pair of fingers inside a long IDT with a metallization ratio of $\eta = 50\%$. This gives the geometric capacitance of the IDT as

$$C_T \approx N_{IDT} C_S W_{IDT} \quad (2.30)$$

with N_{IDT} the number of finger pairs in the IDT.

For our situation of SAW propagating in the [110] direction on a (001) surface of GaAs, we have $K^2 = 0.07\%$, $C_S = 120$ pF/m and $v_0 \approx 2900$ m/s, which results in $y_{SAW} = 3.1 \times 10^{-3} \Omega^{-1}$.

The SAW potential generated in each direction by a single finger is given by

$$\phi_s = \mu_s V_T \quad (2.31)$$

where $\mu_s \approx 0.8K^2$ at $f \approx f_0$. This assumes a relatively wide IDT with many fingers, so that edge effects can be neglected.

The electro-acoustic transfer function $\mu(f)$ of the IDT as a whole is the sum of the contributions from all fingers:

$$\phi_{em}^\pm(f) = \mu(f) V_T = \mu_s V_T \sum_n e^{i\pi_s n (f/f_0)} = \mu_s N_{IDT} \frac{\sin(\xi)}{\xi} V_T \quad (2.32)$$

is emitted in each direction, with

$$\xi = N_{IDT} \pi \frac{f - f_0}{f_0} \quad (2.33)$$

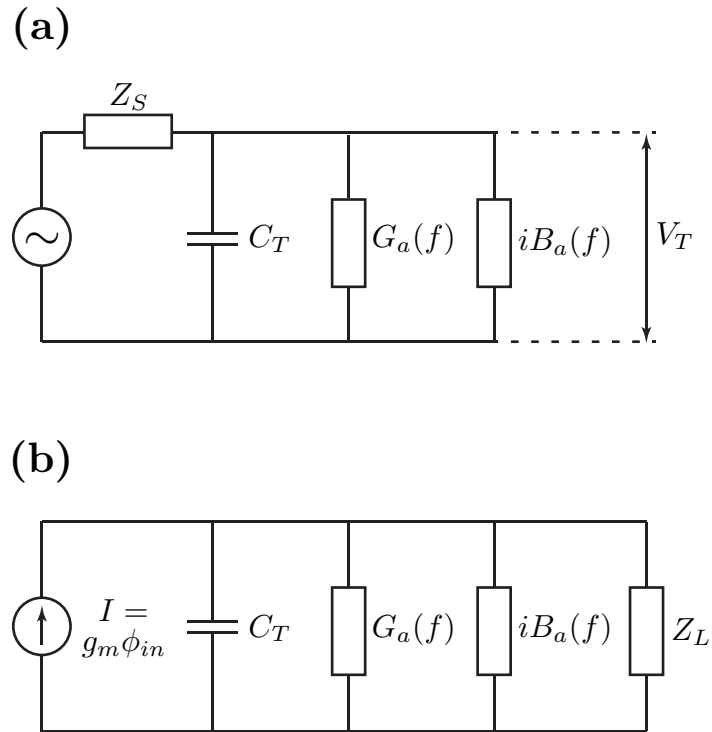


Figure 2.11: IDT equivalent circuits. **(a)** Used as a SAW generator, the IDT is represented by an acoustic conductance G_a which converts an electric signal to SAW. Parallel to G_a are the geometric capacitance C_T and the imaginary acoustic admittance iB_a , which is zero on resonance. The emitted SAW amplitude is $\phi = \mu V_T$ in each direction. **(b)** When the IDT is used as a receiver, the incoming SAW drives a current $I = g_m \mu$ through the circuit elements, including any load impedance Z_L .

When used as a SAW generator, the IDT can be represented by the equivalent circuit shown in Fig. 2.11(a). Equating electrical power with SAW power using Eqs. 2.27, 2.28 and 2.32, we get an effective radiation conductance for converting between electrical and acoustic power:

$$G_a(f) = 2 |\mu(f)|^2 y_{SAW} \frac{W_{IDT}}{\lambda} \quad . \quad (2.34)$$

The factor two comes in since the IDT emits SAW equally in both directions. The geometric capacitance C_T is included in the circuit as a parallel element, along with an imaginary admittance

$$iB_a(f) = i G_a(f_0) \frac{\sin(2\xi) - 2\xi}{2\xi^2} \quad (2.35)$$

with ξ as in Eq. 2.33. B_a is the Hilbert transform of G_a , and it is zero for $f = f_0$.

When subject to an incoming SAW beam, the IDT works as a receiver, generating a current $I = g_m \phi_{in}$ through the circuit elements intrinsic to the IDT as well as any parallel load impedance. The equivalent circuit is shown in Fig. 2.11(b). The receiver response can be inferred from the emitter response through

$$g_m(f) = 2 \mu(f) y_{SAW} \frac{W_{IDT}}{\lambda} \quad (2.36)$$

so that

$$G_a(f) = -\mu(f) g_m(f) \quad . \quad (2.37)$$

Depending on the load impedance shunting the IDT, the current causes a voltage drop V_T over G_a , whereby it re-emits SAW in both directions according to Eq. 2.32. The incoming SAW is regarded as passing straight through the IDT, but it interferes with the re-emitted SAW to a degree that depends on Z_L . In the absence of C_T and Z_L , the incoming ϕ_{in}^+ and the re-emitted ϕ_{em}^+ have opposite phases and cancel out. This effect is prominent in the calculations we do on the coupling between SAW and a superconducting qubit (Ch. 3), since the circuit model for the qubit has a parallel inductance that cancels C_T on resonance.

The formulas presented here do not account for mechanical reflections, which lead to some deviation between theory and experiment when a weakly piezoelectric material such as GaAs is modeled. For a short-circuited IDT ($Z_L = 0$), the model above predicts that any incoming SAW should pass straight through the IDT without interaction, yet this is the way SAW reflectors are usually constructed. The reflection is then described as taking place mechanically, with a certain reflection amplitude for each finger or edge. For thin-film Al IDTs on GaAs, this reflection is around $r_f \approx 1\%$ per finger. Inside the IDT or reflector, the inwards-moving wave decays exponentially from the front edge, and for a finite number of finger pairs N_{IDT} the total power reflection is given by

$$R \approx \tanh^2(2 N_{IDT} r_f) \quad . \quad (2.38)$$

The effective point of reflection is located a distance

$$d_{ref} \approx \frac{\lambda}{4|r_f|} \quad (2.39)$$

into the reflector or IDT from the front. It is possible to combine mechanical and electrical effects in the same IDT model, but we have not done that in the work presented here.

2.3 Cryogenics

As discussed in Sec. 2.1, single-electron devices need to be cold ($k_B T \ll E_C$) to operate, and the same is true for other solid-state quantum devices: The quantum effects are weak and easily destroyed or hidden by thermal fluctuations. For a typical single-electron transistor fabricated by two-angle evaporation (see Sec. 2.4), operating temperatures typically need to be around 1 K or lower. Superconducting qubits and quantized electron pumps are typically operated at temperatures of $T \lesssim 20$ mK, since this is what can reasonably be attained with common cryogenic equipment.

Due to these requirements, and the technical challenges involved in satisfying those, cryogenic engineering and maintenance is an important and integral part of quantum device research. Cryogenic refrigerators become more complex the lower temperatures they are designed to reach. Access to liquid Helium-4 and a suitable vessel are sufficient to reach a temperature of 4.2 K, the boiling point of He-4 at atmospheric pressure. If a vessel containing liquid He-4 is attached to a pump, which removes the gas above the liquid surface, energetic atoms from the bath can more easily escape from the surface, leaving the colder atoms behind. By this type of evaporative cooling, the temperature of the bath can be reduced to $T \sim 1.2$ K. Below this point, there is practically no gas left for the pump to remove, and further cooling becomes increasingly difficult.

To reach lower temperatures, a He-3 refrigerator can be used. It operates by the same principle of evaporative cooling, using the lighter isotope of helium, He-3. Since He-3 is rare and expensive, it is always used in a closed system. A small canister of He-4 (known as the 1 K pot) is cooled continuously by forced evaporation in a separate fluid circuit, which is in thermal contact with the He-3 system. This allows the He-3 to condense and flow to the lowest point of its container (known as the He-3 pot). When all of it has collected there, a charcoal sorption pump is activated, which lowers the pressure above the liquid He-3 and forces evaporation. Since He-3 is light, its atomic adhesion is lower than for He-4 and it continues to evaporate down to lower temperature – a He-3 refrigerator can reach down to 250 mK. Although it is possible to re-circulate the He-3 continuously, it is common for these refrigerators to be of the single-shot type, requiring re-condensation of the He-3 after all of it has evaporated. Such a single-shot He-3 refrigerator is shown in Fig. 2.12(a).

The next step down the temperature ladder is the dilution refrigerator, which is substantially more complex than the He-3 fridge, but capable of reaching a temperature as low as 10 mK and maintain it through a continuous cooling cycle. The dilution refrigerator also has a 1 K pot which is used to condensate He-3. However, instead of cooling the He-3 by allowing it to escape to a gaseous atmosphere of low pressure, the dilution refrigerator uses a similar process taking place inside a liquid mixture of He-3 and He-4. At the lowest and coldest point, known as the *mixing chamber*, the mixture layers into a heavy phase of He-4 with He-3 dissolved in it, and a lighter phase consisting mostly of He-3. The heavy (He-4-rich) phase extends through vertically oriented plumbing to a heated chamber (the *still*) where He-3 can be efficiently evaporated and pumped out. As the evaporation reduces the He-3 concentration in the heavy phase, He-3 crosses the boundary from the He-3-rich phase to the He-4-rich one in the mixing chamber, and it is this transition that absorbs energy from the environment. The mixture that has been pumped out (predominantly He-3) is purified and pre-cooled by the 1 K pot and a system of heat exchangers, after which it is re-injected in the He-3-rich liquid layer in the mixing chamber.

For a dilution refrigerator to serve its purpose, it is essential that electrical conductors

and components are chosen and installed with care: First, the thermal conductance between refrigerator stages at different temperatures must be low, not to heat up the cold parts unnecessarily. By the Wiedemann-Franz law, this means that conductor materials of relatively high resistivity should be used, or alternatively superconducting materials which combine the desirable features of high electrical conductivity and low thermal conductivity for temperatures significantly below the superconducting transition. Cables and wires must be thermally anchored at the various temperature stages of the refrigerator. This is more difficult for coaxial cables than for unshielded DC wires, since the inner conductor of the cable is thermally insulated from the outer conductor. It helps to insert attenuators in the transmission line, to produce galvanic contacts between the two conductors. Lumped-element high-pass filters and bias-tees serve the same purpose, with the additional benefit of segmenting the inner conductor with capacitors, thereby reducing the thermal conductance from the warmer stages. This latter effect that can also be achieved with a DC-block. It is important, however, to make sure all segments of the inner conductor have a galvanic connection to ground, or the insulated segment may get charged by electrons rubbing off from the dielectric, producing voltages high enough to damage equipment and distort signals.

Furthermore, thermal radiation from high-temperature stages must be prevented from reaching the sample. This can be accomplished by inserting low-pass filtering in the measurements lines. However, the filtering must be efficient up to very high frequencies, and commercial lumped-element filters typically cease to work already at frequencies of a few GHz, whereas thermal radiation extends to the THz regime. For low-frequency lines, strong filtering can be achieved by letting a long section of thin insulated wire pass through a volume of fine metal powder [85]. Although stainless steel powder provides stronger attenuation than copper powder due to its higher resistivity, it has been suggested that the stainless steel can have a peaked thermal capacity at low temperature due to residual ferromagnetism, which may keep the weakly thermalized powder grains from reaching base temperature [86]. It is also desirable to mix the powder with epoxy, to improve thermalization of the grains and facilitate the fabrication of the filter.

For coaxial microwave cables, powder filters are not well suited, since they cannot easily be matched to the transmission line impedance. The primary way to filter these is to insert a sequence of attenuators in the line, distributed between the different temperature stages of the refrigerator. Commercial attenuators are usually made from thin resistive films of either NiCr or TaN. Since TaN is a superconductor at low temperature, it is important to avoid those components. At the time of writing, XMA Corporation (USA) are known to use an NiCr process which produces cryogenically compatible attenuators and terminations. Even so, the properties of commercial attenuators do not necessarily extend as high in frequency as required to block thermal radiation from 300 K or even 4 K.

A suitable complement is to use thin coaxial cable made from a resistive material, which strongly attenuate high-frequency signals at least to the limit where waveguide modes dominate over coaxial ones. Such cables also contribute very little thermal conductance between the temperature stages³.

Estimates show that efficient high-frequency filtering can be achieved by using a thin coaxial cable made from a resistive material, but with a superconducting core in the inner conductor. High-frequency noise is forced to run through the resistive coating, whereas DC

³It should be noted that the ratio of attenuation to thermal conductance benefits thin cables: For a given thermal budget, a thin cable attenuates less than a thick one.

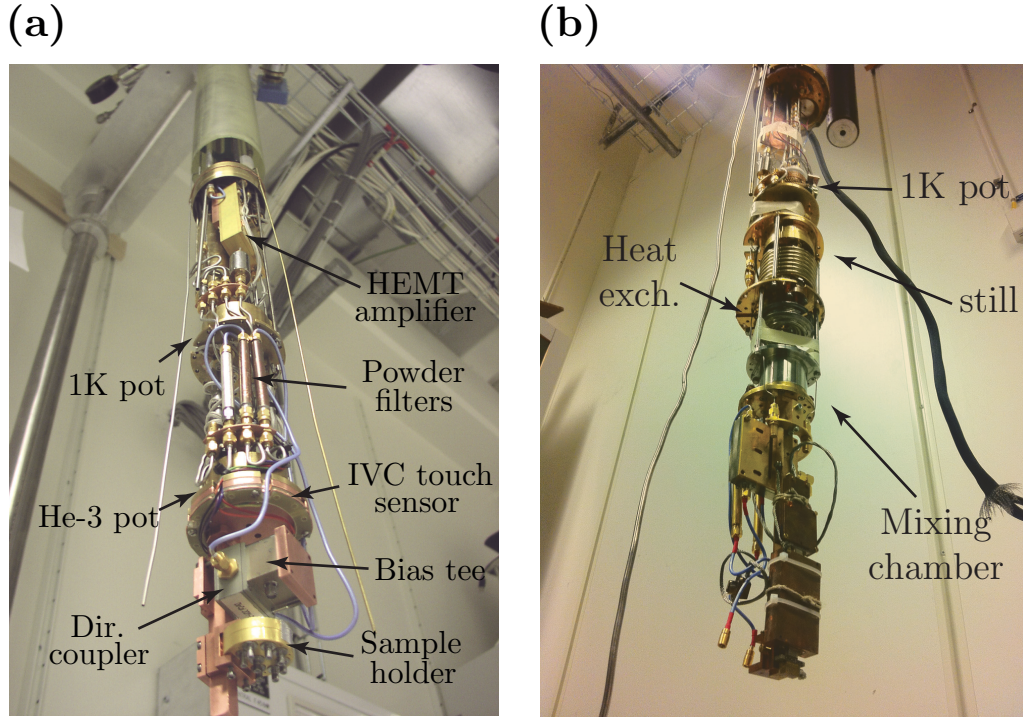


Figure 2.12: Cryogenic measurement setups. (a) Interior view of the He-3 refrigerator known as “Ice Station Zebra”, with important parts labeled. This is an early version of the setup, and several cryogenic components were replaced and added in later experiments. (b) Interior view of the dilution refrigerator known as “Speedy”, where most experiments on detection of surface acoustic waves took place (see Ch. 3).

currents can flow without resistance through the core. Such coaxial cables have yet to be fabricated, but discussions have commenced with one manufacturer (CoaxCo, Japan). Filters using the same principle are demonstrated in Ref. [87].

For signals going from the device under study to pre-amplifiers and room-temperature equipment, it is undesirable to introduce unnecessary attenuation. For such signals, superconducting cable is often used between the base temperature stage and the cryogenic amplifier. Apart from providing nearly lossless signal transmission and negligible thermal conductance, photons with frequencies exceeding $2\Delta/h$, where h is Planck’s constant, are likely to be absorbed by breaking Cooper pairs in the superconductor. Cryogenically compatible low-pass filters with stop-bands extending above 50 GHz are commercially available, *e.g.* from RLC Electronics (USA) and Marki Microwave (USA).

The work leading to this thesis included the installation, testing and troubleshooting of the He-3 refrigerator shown in Fig. 2.12(a). Although the cryogenic measurements presented are mainly electrical, this refrigerator was also equipped with a set of optical fibers going from room temperature to the sample space at base temperature, for use in the experiments on single photon detection (Ch. 5). Fig. 2.12(b) shows the interior of a dilution refrigerator,

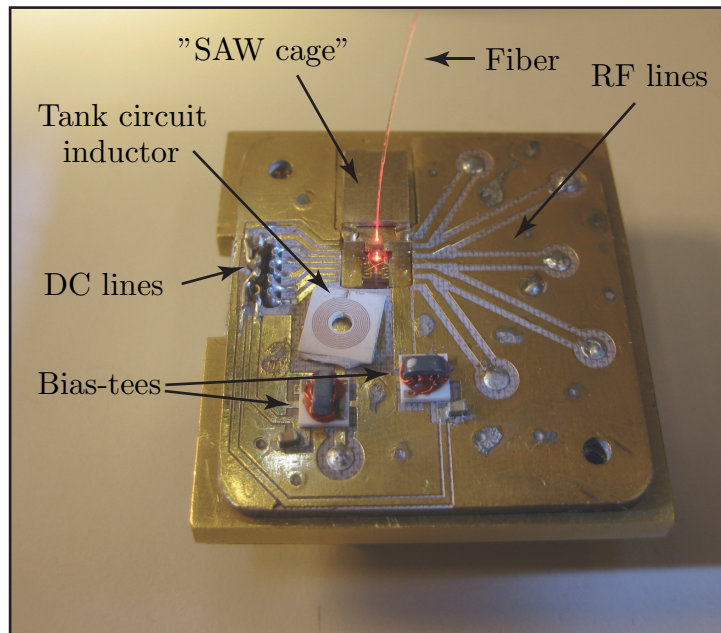


Figure 2.13: A second-generation sample holder for testing photon detectors with SAW and RF-SET, with the lid removed. The bright red spot is the reflection of a visible laser beam in the surface of a photodetector chip (see Ch. 5). The fiber is glued into a metal bar mounted across the sample, and along with the “SAW cage”, it shields the SET and its bonding wires from electrical interference from the SAW and its generation. The sample holder is designed to allow the application of a common-mode potential to the SET in addition to the DC bias and the RF carrier, hence the two bias-tees.

which was used for the experiments on probing surface acoustic waves (Ch. 3). Fig. 2.13 shows a sample holder that was used for many of the experiments.

2.4 Sample fabrication

The devices discussed in this theses are fabricated in a similar fashion to integrated silicon circuits, where the structures are built by layerwise deposition and etching of material on a flat substrate, in patterns defined by lithography using light or accelerated electrons.

Films of metal and dielectric materials can be deposited by many different techniques. In this work, evaporation, sputtering and Chemical Vapour Deposition (CVD) have been the dominant ones. Evaporative coating is done in a high-vacuum chamber, where the substrate is positioned at the top and the source material in a heat-resistant vessel at the bottom. The source can be heated either by passing a high electrical current through a conducting vessel or holder, or by directly bombarding the material with a beam of electrons. When the material reaches its temperature of evaporation or sublimation, atoms are dispatched towards the walls of the chamber. Due to the high vacuum, they have negligible risk of colliding with residual gas, and thus travel in straight lines until they reach the substrate or a chamber wall and stick there. The films produced in this way are usually less dense than those deposited by other methods, and the deposition rate and thickness are limited. The advantages of the process includes its simplicity, compatibility with many different material, and the ability to produce layered stacks of heterogenous materials, including organics which cannot sustain high temperatures. When evaporation is done through a mask of resist, very sharp features can be realized.

Sputtering is a high-throughput process, hence favored in industrial settings. An inert-gas plasma, typically Argon, is used to bombard the source, causing it to erode. The atoms and atomic clusters ejected from the source impact the substrate with high energy and produce a dense coating. Sputtered films are often of higher quality than evaporated ones, but due to the more isotropic impact trajectories and higher surface diffusion, it is not as well suited for deposition through a resist mask.

CVD is a high temperature technique where gas precursors are funneled into a reactor where the substrate is placed. The precursors react chemically at the substrate surface, leaving behind a layer of the desired material, along with volatile byproducts which are removed in a continuous flow of gas. A plasma in the chamber can also help to enhance the chemical reaction. The process is then called Plasma Enhanced CVD, or PECVD. The uniformity and density of SiO₂ and SiN deposited by CVD is usually higher than those achieved by sputtering or evaporation. However, due the the high temperature of the process, it is incompatible with polymeric resist.

Patterning is done by spin-coating the substrate with a thin layer of resist, which is sensitive to ultra-violet radiation, high-energy electrons or both. For work on the laboratory scale, photolithography is usually employed for bigger and less dimension-critical patterns, whereas the finest structures are patterned by a scanned electron beam. In its simplest form, photolithography consists of pressing the photoresist-covered substrate against a glass reticle covered with a metal film in the shape of the desired pattern. After the glass mask and the substrate have been manually aligned, the stack is uniformly exposed to UV light, which triggers a reaction in the parts of the resist where the metal on the glass mask has openings. Development in a chemical bath removes either the regions which were exposed to light or the ones which were not, forming a replica of the mask metal in the resist.

Electron Beam Lithography (EBL) requires vastly more complex and expensive equipment, but is capable of producing much finer structures and does not require the pre-fabrication of a glass mask. Compared with photolithography, EBL is slow, since the resist is not exposed all

at once. Instead, a computer controlled beam of electrons is focused to a spot on the substrate, and moved around to expose the resist in a pattern determined directly from a computer drawing. The development process after exposure is similar to the one used for photolithography, although EBL resist is often developed in an organic solvent whereas photoresist developer is usually water-based.

A modern EBL machine, such as the JBX-9300FS in the MC2 Nanofabrication Laboratory, is capable of making lines as slim as 10 nm in resist. This machine accelerates the electrons to kinetic energies of 100 keV. The high energy minimizes the spread of electrons upon impact with the resist, allowing for a sharp exposure also in thick resist layers. In addition to the high precision, the machine is capable of detecting previously deposited alignment marks on the substrate, and use those to align patterns from different exposures to an accuracy of a few tens of nanometers. A notable issue with EBL is the back-scattering of electrons from the substrate in a region surrounding the impacting beam, which exposes the resist from underneath. This effect is less prominent when high acceleration voltages are used, since the back-scattered electrons spread over a wider area, typically tens of micrometers.

The backscattering effect is counteracted either by modulating the exposure dose with the scattering profile taken into account (“Proximity correction”), or by using a conductive layer underneath the resist, either as part of the permanent device structure or as a sacrificial layer in a multi-layer resist stack. On insulating substrates, EBL has the additional problem of local build-up of charge, which severely distorts the pattern unless precautions are taken. One way to alleviate this is to deposit a charge dispersion layer of Al or Cr on top of the resist by resistive evaporation (neither electron beam evaporation nor sputtering can be used, since they produce X-rays that expose the resist). The metal absorbs and distributes the charge during exposure, and is etched away before the resist is developed. Special caution must be taken when the sample already has patterned conductors covered by dielectric materials, since charge from the conductor may cause a breakdown through the dielectric and the resist up to the charge dispersion layer.

The resist pattern is transferred to the materials of the device either by etching or by lift-off. *Etching* can be done straightforwardly by immersing the sample in an acidic or alkaline bath, which dissolves the topmost layer in the regions that are not protected by resist. The etchant must be chosen according to the material to be removed, which should preferably be etched much more efficiently than the underlying layers and the resist.

Wet processes are straightforward and can be fast, but often suffer from imprecision and undesired etching extending past the edges of the resist mask. The alternative to wet etching is *dry etching* or plasma etching. The process takes place in a vacuum chamber, where the substrate is subject to a mixture of gases which have been ionized into a reactive plasma. An electric AC field applied normal to the substrate surface causes the ions to impact the substrate anisotropically and produce a sputtering effect in addition to any chemical reactivity of the radicals. The plasma can also be isotropically energized by inductive power transfer. A continuous gas flow ensures that the plasma does not degrade over time, and that volatile byproducts are removed from the chamber. By controlling the power transferred to the plasma, the pressure, and the composition of gases, the speed and the degree of isotropy of the etching can be controlled. The etching depth can be measured by laser interferometry or real-time analysis of the etching byproducts. Disadvantages of plasma etching compared with wet etching include the higher cost of equipment, the slower etching speed for certain materials, and the lower etching resistance of the resist. The latter issue is particularly prominent with high-resolution e-beam resist. The impact of the plasma is also believed to damage certain

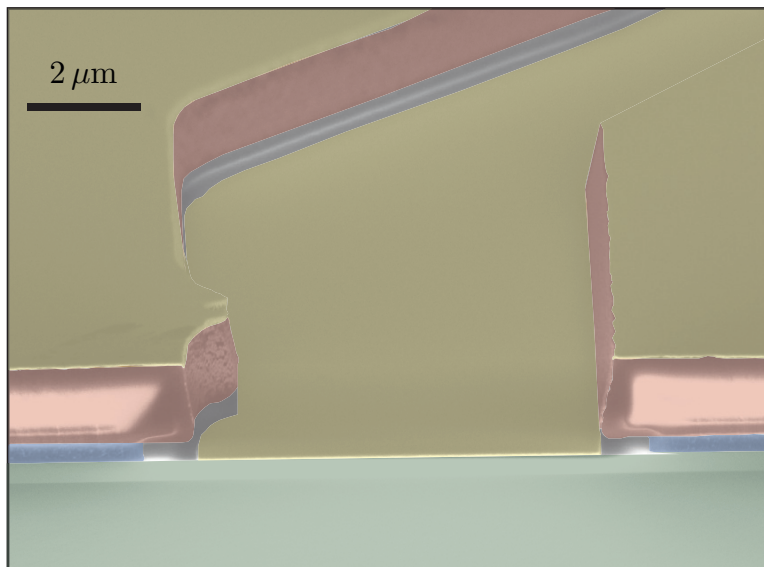


Figure 2.14: Electron micrograph with false-color overlay showing the cleaved edge of an oxidized silicon substrate covered with two-layer photoresist, after development and metal deposition but before lift-off. Red: Imaging layer of photoresist. Blue: Lift-off layer. Yellow: Evaporated gold. Green: Thermal SiO_2 deposited on the silicon substrate. Although the sidewalls of the photoresist are covered with deposited metal, there is no connection between the layer sticking to the resist and the one sticking to the substrate. This ensures sharp and flat edges of the film.

sensitive devices (*e.g.* III-V heterostructures with high demands on carrier mobility).

Lift-off is the other common pattern transfer technique, where material is deposited on top of a substrate already covered with developed resist. The material sticks to the substrate in locations where the resist is absent, and when the resist is dissolved after deposition, the material which was deposited on top of it also comes off. The resist is usually developed with an undercut to keep the deposited material from sticking to its sidewalls. This is done either with a single layer of resist tailored for this purpose, or by using a stack of two resist layers. In a two-layer stack, the image layer where the lithographic pattern is defined sits on top of a lift-off layer, which only serves the purpose of producing a sufficient undercut when developed. A two-layer resist stack for lift-off is illustrated in Fig. 2.14.

Although sputtering can be used together with lift-off if small and sharp features are not required, evaporation is the most common deposition technique, since it is very anisotropic and produces sharp boundaries at the edge of the imaging resist. In commercial circuit fabrication, lift-off is rarely used, since it is time-consuming and less reliable than etching, and does not work well with sputtering or high-temperature deposition techniques.

For SET devices, a particular version of the lift-off process dominates, where metal is evaporated twice through the same resist mask without breaking the vacuum, but with different angles between the source and the substrate to make two displaced copies of the pattern. In an oxidation step between the two evaporations, a thin dielectric layer is produced, which forms

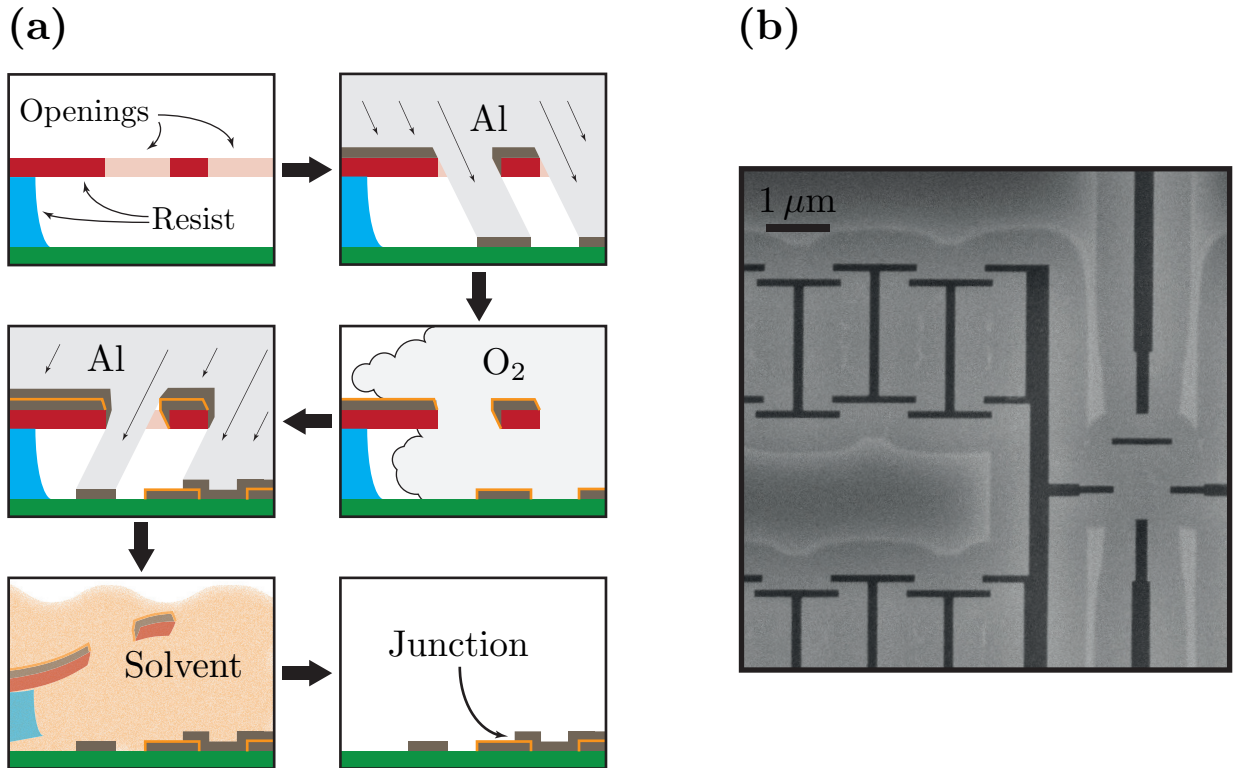


Figure 2.15: Shadow evaporation. **(a)** The developed two-layer resist mask has a relatively large undercut. The first evaporation is done at an angle, forming a shadow that is offset from the mask pattern. After oxidation in pure O_2 , the second layer is evaporated from the opposite direction, forming a junction of Al, AlO_x (shown in orange) and a second layer which may be any metal that can be deposited by evaporation. After lift-off in a liquid solvent, the junction and the leads remain stuck to the otherwise clean substrate. **(b)** Electron micrograph of a rigid Ge mask for a particularly demanding three-angle evaporation, used to make SINIS turnstiles terminated with SQUID arrays (see Ch. 6). The dark regions are openings etched in the Ge layer, the lighter region surrounding the pattern is the plasma-processed undercut, and the lightest regions are the bottom resist layer supporting the Ge. The recipe for this process is given in Appendix 1

a tunnel junction where the second evaporated layer overlaps the first layer and the oxide. The principle is described schematically in Fig. 2.15. To make room for the two shadows, the resist needs to have a bigger undercut than in a common lift-off process. For patterns with relatively large features and no long suspended bridges, and where electron backscattering is not critical, a resist stack consisting of two layers is usually sufficient.

For finer features, and when the resist must have a high structural integrity, it is advantageous to use a three-layer stack with a hard material such as evaporated Ge in the middle. The top layer is made as thin as possible to maximize the EBL writing precision, and after development its pattern is transferred to the hard layer by anisotropic plasma etching. The undercut layer can be developed in a wet process, as for two-layer resist stacks, but the non-polymeric hard mask also allows the undercut to be defined by an O_2 plasma. There are several advantages to this: Unless a critical-point dryer is used, a wet development process exerts stress on the resist when the rinsing fluid is dried, which may distort the mask. With a plasma process, this is not an issue, and the bottom layer can also be baked at higher temperature and for a longer time, making it more sturdy. Finally, by adjusting the plasma parameters, the profile of the undercut can be well controlled. Fig. 2.15(b) shows an example of a developed three-layer resist mask used for three-angle evaporation of SINIS turnstiles with SQUID array terminations.

Detailed recipes for a few common fabrication steps are presented in Appendix 1

Chapter 3

Coupling quantum devices to surface acoustic waves

The experimental work presented in this chapter concerns the probing of Surface Acoustic Waves (SAW) with an RF-SET, locally inside an acoustic echo chamber fabricated on a microchip. The results were disseminated in Paper I and its Supplementary material which consists of Supplementary Methods (Sup. Met.) and Supplementary Discussion (Sup. Disc.).

The project is a spin-off from the work on photodetectors (Ch. 5), where SAW and RF-SETs were included as basic components. The author did the experimental work, and analyzed the data with contributions from Per Delsing (P.D.). The theoretical understanding was largely developed in discussions, with substantial contributions from P.D. and Göran Johansson (G.J). Paulo Santos contributed with his expertise about SAW.

Several impressive experiments have recently been done in order to demonstrate quantum effects in mechanical resonators [88–92]. Our experiment is also mechanical, but what sets our efforts apart is the propagating nature of the waves we study: The suspended mechanical resonators resemble guitar strings or drums, whereas SAW resembles the sound that they produce – capable of moving from the string or drum to your ear. While the experiments we present are all done on classical SAW, the sensitivity we can reach with the RF-SET indicates that quantum mechanical experiments are not out of bounds.

We use the description of Datta [80] for our calculations on SAW-based circuits, as outlined in Sec. 2.2.

3.1 Experimental setup

The experiments were done on a chip of semi-insulating GaAs, which is shown in Fig. 3.1, replicated from Paper I with some cosmetic updates. Two IDTs are deposited on the chip, each with a width $W_{IDT} = 320 \mu\text{m}$ and with their fronts separated by 2.9 mm. One of them, IDT_{left} , can be excited electrically to produce SAW, and IDT_{right} is grounded, to work only as a reflector. The SET is deposited on the SAW propagation axis, a distance $d_1 = 2252 \mu\text{m}$ from the generating IDT and $d_2 = 651 \mu\text{m}$ from the reflector. Since both IDTs reflect incoming SAW to some extent, they work together to form an acoustic cavity – an echo chamber – where the SAW may bounce back and forth. The cavity in this experiment is very long, to allow us enough time to observe SAW reflections in the time domain. It is then necessary to use wide IDTs, in order to avoid the Fraunhofer diffraction which becomes important at

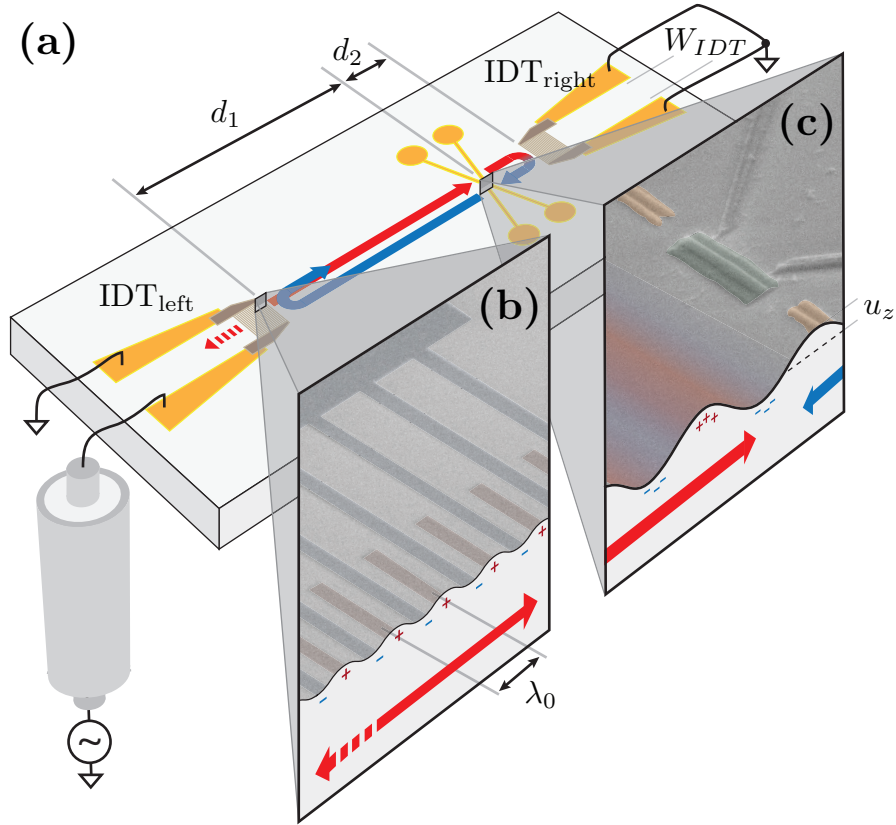


Figure 3.1: Sample with an SET inside an on-chip echo chamber. **(a)** The GaAs chip is around 6 mm long and has two IDTs (IDT_{left} and IDT_{right}) on its surface, separated by a distance $d_1 + d_2 = 2252 + 651 \mu\text{m}$. IDT_{left} can be driven with an RF signal, whereupon it emits SAW (red arrows). IDT_{right} is grounded to act as a reflector (blue arrows indicate reflected SAW). The SET is deposited between the IDTs, in the center of the SAW beam. **(b)** Electron micrograph in false-color, showing the positive and negative electrodes of IDT_{left} interdigitated with period $\lambda_0 = 3.12 \mu\text{m}$. The IDT emits SAW in both directions when electrically excited, as indicated by the red arrows. **(c)** Electron micrograph in false-color of the SET. The island is shown in green and the gate electrodes in yellow. The SET is geometrically symmetric in the propagation axis of the SAW, and the two gate electrodes were connected with a bonding wire. The vertical displacement of the surface, u_z , is exaggerated by a factor $\sim 10^{10}$ for the purpose of illustration.

distances larger than

$$L_D = \frac{W_{IDT}^2}{4\lambda} \quad . \quad (3.1)$$

In our case $L_D = 8.2$ mm, so the beam is well collimated.

As the SAW traverses the substrate, the piezoelectric polarization produces a density of surface charge proportional to the SAW amplitude. When the wave passes the SET, the integrated charge Q_{SAW} in the area underneath the SET island, $A_{SET} = 1.4 \times 0.4 (\mu\text{m})^2$, is induced on the island and detected. The SET had a charging energy of $E_C/k_B = 2.1$ K and a total resistance of $R_\Sigma \approx 50$ k Ω . It was coupled for RF readout and DC-biased through a voltage divider and a PCB-mounted bias-tee at base temperature. Since the SAW frequency $f_{SAW} = 932$ MHz is much higher than the RF-SET read-out bandwidth of $BW \approx 8$ MHz, the mixing techniques described in Sec. 2.1.5 were used to measure Q_{SAW} .

We cooled the sample in a dilution refrigerator (“Speedy”, shown in Sec. 2.3). Although the base temperature of this refrigerator is $T_0 < 20$ mK, dissipation in the voltage divider, attached to the mixing chamber and used to bias the SET, caused the refrigerator to heat slowly up to $T_0 \approx 200$ mK when the SET was operated. This problem is in principle easily corrected, but since the sample had a relatively low level of charge fluctuations, we did not want to take the risk of warming the refrigerator and make adjustments. The total noise temperature of the RF-SET measurement setup was $T_N \approx 11$ K at best, and 200 mK $\ll E_C/k_B$, so the elevated temperature did not significantly influence the results.

The carrier signal for the RF-SET was provided by one channel of a Marconi 2026 RF generator, while another channel supplied the Local Oscillator (LO) signal for mixing measurements. The LO and a pilot signal for SET sensitivity measurements were superimposed with bias tees at room temperature and coupled to the SET gate. The SAW power was sourced from an Anritsu MG3695B microwave generator with pulsing capability, which also provided the 10 MHz synchronization clock for all instruments and the trigger for time-domain data acquisition. The amplified RF-SET signal was digitized with an Aeroflex 3035C PXI unit. We used a DS345 from Stanford Research Systems to generate the pilot signal, and SIM928 units from the same company for biasing and gating the SET at DC.

The sample holder, shown in Fig. 2.13, was designed to screen the electric field of the IDT and its bonding wire from the SET and the rest of the chip, to avoid electrical crosstalk.

3.2 Basic characterization

We did the first characterizations on the coupling between the SAW and the SET with high SAW amplitude, observing the rectification pattern of Fig. 2.7. This provides a calibration between the RF amplitude applied to IDT_{left} and the charge amplitude Q_{SAW} induced on the SET by the SAW. At the frequency where the SAW couples strongest to the SET, we found a ratio between induced SET charge and applied IDT voltage of

$$C_{SAW} = \frac{Q_{SAW}}{V_{IDT}} = 81.5 \text{ aF} \quad (3.2)$$

where $P_{IDT} = V_{IDT}^2/50 \Omega$ is the electrical power supplied to the IDT¹. Time-dependent measurements show that the direct coupling in the absence of cavity reflections, *i.e.* of SAW

¹We use RMS units for amplitudes throughout the calculations.

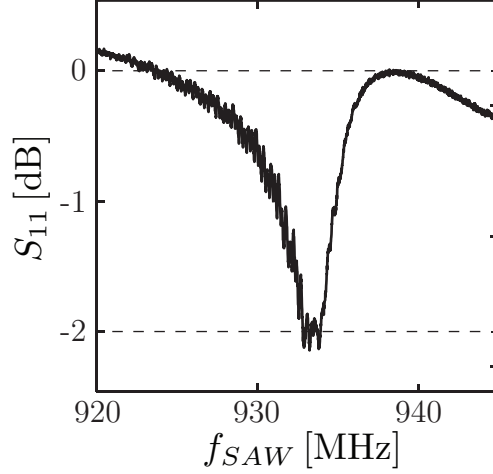


Figure 3.2: Reflection measurement of IDT_{left} , done in a separate cooldown from the SET measurements. The reference level is adjusted to the local maximum on the upside of the resonance. Approximately 60% of the electrical power is reflected, and even though some SAW is back-transduced into electrical power after a round-trip in the cavity, the reflection is predominantly electrical. 50% of the power converted to SAW is immediately lost since the IDT is bidirectional.

reaching the SET directly from IDT_{left} , is

$$C_{SAW}^* \approx C_{SAW}/4 \approx 20 \text{ aF} \quad . \quad (3.3)$$

Calculations on SAW propagating in the $[110]$ direction² of GaAs are relatively straightforward. In our coordinate system, \hat{x} aligns with this direction, \hat{y} with the IDT fingers and \hat{z} with the surface normal of the substrate. The surface charge density is given by

$$\sigma = e_{14} S_{xx} = e_{14} \frac{\delta u_x}{\delta x} \quad (3.4)$$

where $e_{14} = 0.16 \text{ C/m}^2$ is the piezoelectric coefficient of GaAs and S_{xx} the surface strain in the \hat{x} direction. For a harmonic wave, the amplitude is

$$|\sigma| = \frac{2\pi}{\lambda} e_{14} |u_x| \quad . \quad (3.5)$$

The ratios between mechanical surface displacement and SAW potential are

$$|c_x| = \left| \frac{u_x}{\phi} \right| = 0.98 \text{ nm/V} \quad \text{and} \quad |c_z| = \left| \frac{u_z}{\phi} \right| = 1.31 \text{ nm/V} \quad (3.6)$$

from Ref. [80], and we can combine these relations to get the SAW potential measured by the SET:

$$\frac{|\phi|}{V_{\text{IDT}}} = \frac{C_{SAW}^* \lambda}{2\pi A_{\text{SET}} e_{14} |c_x|} \quad . \quad (3.7)$$

²This is the direction of natural fracturing for a standard (001)-cut GaAs wafer.

Comparing the supplied power with the detected one, we get

$$\frac{P_{SAW}}{P_{IDT}} = \frac{|\phi|^2 Y_{SAW}}{P_{IDT}} \approx 20\% \quad . \quad (3.8)$$

This is confirmed by an RF reflection measurement of the IDT, done after all measurements with the SET had been completed, in a different refrigerator but with the sample still bonded to the same sample holder. The IDT reflection is plotted in Fig. 3.2. Around 60% of the electrical power supplied to the IDT is reflected, and half of the power converted to SAW is lost by going toward the left end of the chip. Some of the SAW emitted toward the SET comes back as an electrical signal after a round-trip in the cavity, as seen from the ripples in Fig. 3.2. There is, however, also loss during propagation, possibly due to scattering against some visible dust in the region near IDT_{left} .

3.3 Acoustic modeling

To better understand the cavity resonance between the IDTs, we measured the SET response with $2\mu s$ long pulses applied to IDT_{left} over a range of frequencies. We fitted this data set with a numeric model, and the two figures are compared in Fig. 3(d) of Paper I . We were not able to make an accurate model for the frequency response of the IDT with the theory of Sec. 2.2, but used the estimate

$$\phi_{in} \propto \frac{\sin(\xi)}{\xi} \quad (3.9)$$

from Eq. 2.32 to represent the SAW approaching the SET from IDT_{left} before the first reflection. We assume that the reflections take place in a single point at a distance d_{ref} from the front of each IDT, with a loss of β_{left} or β_{right} for each round-trip from the SET to an IDT and back. Since the IDTs do not have enough fingers to be considered infinite, the reflection losses were bounded by the transmission through the IDT, according to Eq. 2.38. The SET response is given by the sum over the complex amplitudes of all SAW components that coincide at the SET at any time (coming directly from IDT_{left} and from the different reflections). The result is a sequence of plateaus along the time axis and an interference pattern along the frequency axis. After initial manual parameter fitting, a least-squares algorithm was used to fit the levels of the plateaus to the data. In spite of its crudeness, the simulation can replicate the cavity behaviour in the time and frequency directions well, although we cannot use it for quantitative predictions along the amplitude scale. For that, we must study time-domain traces at the specific frequency of interest.

3.4 Sensitivity

We measured the sensitivity of the RF-SET to SAW by heterodyne mixing, as described in Sec. 2.1.5. The local oscillator was displaced from f_{SAW} by 700 kHz to avoid the $1/f$ noise of the SET and the amplifiers. We optimized the sensitivity in an iterative process, with respect to V_b , V_g , the RF-SET carrier amplitude and the LO amplitude, and found a best value of $\delta Q_{SAW} = 25 \mu e_{RMS}/\sqrt{Hz}$. This corresponds to a sensitivity to displacement in the \hat{z} direction of

$$\delta u_z = \delta Q_{SAW} \frac{|c_z|}{|c_x|} \frac{\lambda}{2\pi A_{SET} e_{14}} = 30 \text{ am}_{RMS}/\sqrt{Hz} \quad . \quad (3.10)$$

Compared with other sensitive measurements of SAW [93, 94], this is an improvement of 2 – 3 orders of magnitude. We can compare the sensitivity with the calculated thermal and zero-point background fluctuations

$$\delta \tilde{u}_z \approx |c_z| \sqrt{\frac{2h f_{SAW}}{y_{SAW}} \coth\left(\frac{h f_{SAW}}{2k_B T}\right)} . \quad (3.11)$$

This calculation is described in detail in Sup. Met. IV of Paper I . At zero temperature, we get the amplitude of vacuum fluctuations (the quantum limit) as

$$\delta \tilde{u}_z(T = 0) \approx |c_z| \sqrt{\frac{2h f_{SAW}}{y_{SAW}}} = 0.046 \text{ am}/\sqrt{\text{Hz}} . \quad (3.12)$$

In order to detect very weak pulses, we used the SET as a homodyne mixer (see Sec. 2.1.5). We applied the LO and the RF-SET carrier continuously and used the internal pulsing capability of the Anritsu to generate 1 μs long rectangular pulses to IDT_{left}. With this pulse length, there is some overlap at the SET between the pulse coming directly from IDT_{left} and its reflection from IDT_{right}. The phase of the LO was cycled between eight values during the measurement and one averaged time trace was acquired for each phase. The sampled data were digitally low-pass-filtered in the post-processing. By comparing two signals acquired with the LO in counterphase and verifying the timing of the acquired pulses against the acoustic delay, we can be confident that the pulses we observe are really SAW, in spite of the low signal-to-noise ratio. Two such traces are shown in Fig. 4 of Paper I . In this measurement the SAW power density was $P_{SAW}/W_{IDT} = 2.8 \times 10^{-19} \text{ W}/\mu\text{m}$, which could be detected with 10^7 averages. This corresponds to $\sim 0.6 h f_{SAW}$ per pulse within the width of the SET.

3.5 Noise and back-action

Sup. Disc. I of Paper I describes several possible improvements to the sensitivity, in order to get closer to the quantum limit.

There is room for improvement in the sample layout and the properties of the SET: By extending the width of the SET island to $\lambda_0/2$, we can double the amount of charge the SET picks up, and a higher E_C allows a stronger carrier signal to be used, which improves the Signal-to-Noise Ratio (SNR).

It is also interesting to consider the use of a strong acoustic resonance to increase the SAW amplitude under the SET. The sample used in the experimental study has a long cavity and high reflection loss, which means that there is virtually no resonant enhancement of the signal: In the measurements on weak pulses, each pulse merely passes the SET twice before decaying. This can be put in contrast with other micro-mechanical experiments, where the quest for high mechanical quality factors (Q) is considered essential.

Although our device was not optimized in this respect, it is worth noting that SAW devices are known for achieving high Q -factors at the high frequencies ($f_{SAW} \gtrsim 1 \text{ GHz}$) where the quantum ground state can be reached with regular cryogenic equipment. Not many experiments have been published on SAW at low temperature, but El Habi *et al.* [95] report $Q \approx 180\,000$ at $f_{SAW} = 416 \text{ MHz}$ on quartz, at low temperature but with normal-conducting IDTs and reflectors. During the SET experiments, we found that the dissipation in the IDTs

was large when the Al of the IDTs was kept in the normal state, and a sharp decrease in losses when the IDTs turn superconducting has also been shown in systematic studies [96].

With two SAW reflectors surrounding the SET locally, the resonant enhancement of the SAW should enhance the SNR substantially. In a certain sense, the system then starts to resemble a suspended resonator, since SAW confined to such a Fabry-Perot cavity is no longer propagating. A crucial difference, however, is that the SAW can exist also outside the cavity, and if the internal quality factor dominates over the external one $Q_{int} > Q_{ext}$, the cavity can act as a trapping device for the acoustic waves that impinge on it. For a probe enclosed in a high- Q cavity, back-action becomes an important issue, as discussed below and in Sup. Met. V of Paper I.

The second general improvement, apart from increasing the measured signal, is to decrease the level of added measurement noise. Our noise temperature of $T_N > 10$ K is limited by the cryogenic HEMT amplifier, and amplifiers of the same kind are available with much higher performance. The most substantial noise reduction can be achieved if a parametric amplifier is inserted as the first gain stage in the circuit. For signals with a certain phase, such an amplifier adds no noise at all. Parametric amplifiers have started to become important tools for quantum experiments in recent years, with gains of $\gtrsim 20$ dB in practical devices.

However, even with no added amplifier noise, the SET is dissipative and thus has an ultimate sensitivity limit set by its shot noise (see Sec. 2.1.3). In addition to reducing the measurement sensitivity, the shot noise produces a back-action on any system it is coupled to [34]. In the case of SAW, this manifests as an emission of SAW phonons from the SET within the measurement bandwidth. Without mechanical resonance, the emitted phonons are of little concern since they never return to the SET to be detected. If we were, however to improve the sensitivity by surrounding the SET with high-performance SAW reflectors, the back-action sets a limit on the quality factor of the acoustic cavity. The back-action is discussed in some detail in Sup. Met. V of Paper I, where we find that the shot noise alone would limit the quality factor of the cavity to $Q \ll 300\,000$ in order to keep it occupied by $n \ll 1$ back-action phonons.

In addition to the shot noise, dissipation in the SET results in heating of the electrons on its island, and the major part of this thermal power is ultimately converted to phonons. This is also discussed in Sec. 2.1.2 and Ch. 4. This back-action is harder to estimate, since we do not know what fraction (if any) of the phonon power enters the Rayleigh modes. Common models for the thermalization of the SET electron gas assume that all power dissipates to the substrate bulk. In Ref. [26], Qu *et al.* calculated the thermalization expected from a mechanical model where Rayleigh modes are taken into account and found that the electron-phonon thermalization power should scale as $P_{e-ph} \propto T_e^6 \log T_e$ for such a model. Although experiments indicate that the actual dependence is the $P_{e-ph} \propto T_e^5$ expected when only bulk phonons cool the SET electron gas [15, 22, 24], we cannot exclude that the SET emits thermal Rayleigh phonons with a power that is substantial on the scale of quantum measurements. The RF-SET should be a suitable tool to study this thermalization path experimentally: By dissipating a controlled amount of power on a surface some distance away from the SET and measuring its time-domain response, it should be possible to separate phonons reaching the SET through different modes.

For truly quantum limited detection of SAW, a Quantum Capacitance Electrometer (QCE) [97, 98] may be a better probe than the RF-SET. The QCE is a Cooper-pair box, similar to an SEB but with a charge periodicity of $2e$ and a Josephson energy splitting at the charge degeneracy point. The curvature of the lower energy band around charge degeneracy works as

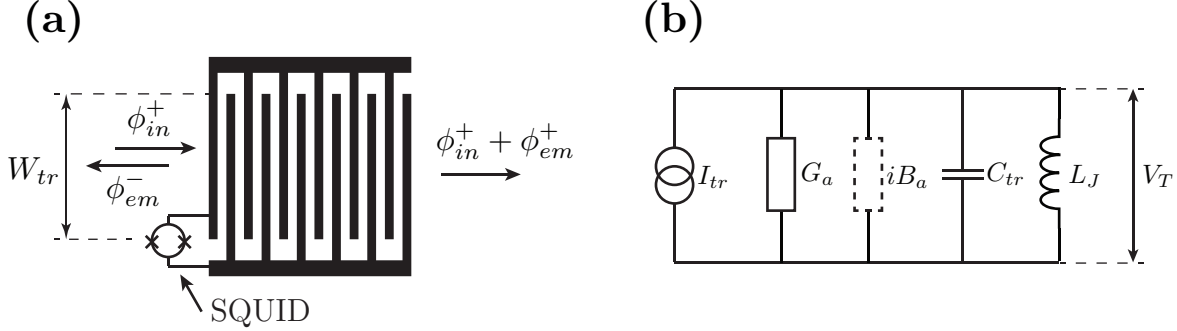


Figure 3.3: A SAW-coupled transmon. **(a)** Schematic of a transmon where C_{tr} has been shaped into an IDT, with complex SAW amplitudes labeled. **(b)** Equivalent circuit, valid for low driving powers. C_{tr} and L_J are the geometric capacitance and the SQUID inductance, respectively. The admittances G_a and iB_a come from the IDT model described in Sec. 2.2. The current through the circuit due to incoming SAW is $I_{tr} = g_m \phi_{in}^+$, and the IDT structure re-emits SAW with amplitude $\phi_{em}^\pm = \mu V_T$ in each direction.

an effective capacitance $C_Q = \delta^2 E / \delta V_g^2$, which can be read out in a dissipation-free process. As for practical RF-SSETs, the performance is limited by the amplifier, and the QCE needs to be probed with a relatively weak RF signal to avoid the non-quadratic regime of the energy band, which reduces the SNR compared with the RF-SSET. This problem can in principle be solved by parametric post-amplification.

3.6 Coupling SAW to a superconducting qubit

We have also investigated in theory how SAW can be coupled to a superconducting qubit. For these studies, we consider a qubit of the “transmon” type, which consists of a Josephson junction shunted by a large geometric capacitance [99, 100]. The compelling point about the transmon is that its geometric capacitance, C_{tr} , can be fashioned into the shape of an IDT, and thereby couple to SAW modes in the substrate where it is deposited. The Josephson junction is typically fabricated in the form of a Superconducting Quantum Interference Device (SQUID), so that its Josephson coupling energy E_J , and consequently also its Josephson inductance L_J , can be tuned with a magnetic field.

The transmon can be described by a classical equivalent LC -circuit at low driving powers, *i.e.* as long as only the two lowest energy states of the harmonic LC -oscillator are populated. We can merge this model with the IDT model in Sec. 2.2, letting C_{tr} take the role of C_T . A schematic of the layout along with the equivalent circuit are shown in Fig. 3.3. The qubit center frequency is given by the resonance between C_{tr} and L_J .

$$\omega_{0,Q} = \frac{1}{\sqrt{L_J C_{tr}}} \quad . \quad (3.13)$$

An incoming SAW beam with complex amplitude ϕ_{in}^+ generates a current $I_{tr} = g_m \phi_{in}^+$ through the circuit, dropping a voltage V_T over the parallel elements depicted in Fig. 3.3(b). In

response to the voltage, the circuit will emit SAW with complex amplitude $\phi_{em}^\pm = \mu V_T$ in both directions, referred to a common point such as the center of the transmon.

We assume that the electrical and acoustic resonances coincide at the angular frequency ω_0 , and calculate the response of the transmon to incoming SAW of frequency

$$\omega = 2\pi f_{SAW} \quad . \quad (3.14)$$

On resonance ($\omega = \omega_0$), the parallel connection of C_{tr} and L_J has a real impedance approaching infinity and the imaginary acoustic admittance iB_a goes to zero. The total acoustic admittance is then given by $Y_{tot}(\omega_0) = G_a(\omega_0)$, and using

$$G_a = -\mu g_m \quad (3.27)$$

we get the emitted amplitude in each direction as

$$\phi_{em}^\pm = \mu \frac{g_m \phi_{in}^+}{G_a} = -\phi_{in}^+ \quad . \quad (3.15)$$

This means that the SAW amplitudes in the positive direction cancel, and all power is reflected. This is analogous to the reflection of a photon in a transmission line by a real or artificial atom [101–103].

As a function of frequency, we have:

$$\phi_{em}^\pm(\omega) = \mu(\omega) V_T = \frac{\mu(\omega) I}{Y_{tot}} = \frac{\mu(\omega) g_m(\omega) \phi_{in}^+}{G_a(\omega) + iB_a(\omega) + i\omega C_{tr} + 1/(i\omega L_J)} \quad . \quad (3.16)$$

Inserting Eq. 2.37 and Eq. 3.13 gives

$$\phi_{em}^\pm(\omega) = \frac{-\phi_{in}^+}{1 + \frac{i}{G_a(\omega)} \left[B_a(\omega) + \frac{\omega}{L_J} \left(1 - \frac{\omega^2}{\omega_0^2} \right) \right]} \quad . \quad (3.17)$$

A useful transmon [101, 104] may have $E_J/E_C = 40$ and $\omega_0/2\pi = 5$ GHz, which gives

$$C_{tr} = \frac{e^2}{2E_C} = 69 \text{ fF} \quad \text{and} \quad L_J = \frac{\hbar^2}{4e^2 E_J} = 15 \text{ nH} \quad . \quad (3.18)$$

Here we use $E_C = \frac{e^2}{2C_{tr}}$, *i.e.* defined for electrons rather than Cooper pairs. For fixed C_{tr} , the physical width of the transmon is

$$W_{tr} \approx \frac{C_{tr}}{N_{tr} C_S} \quad (3.19)$$

with N_{tr} the number of finger pairs in the capacitance and C_S the capacitance per unit length of a single such pair. For a finger structure with reasonable dimensions, $N_{tr} \lesssim 50$, the resonance of the electrical circuit elements dominates over the acoustic one, so B_a can be neglected and $G_a = G_a(\omega_0)$.

The reflection and transmission of acoustic power are given by

$$R = \frac{|\phi_{em}^-|^2}{|\phi_{in}^+|^2}, \quad T = \frac{|\phi_{em}^+ + \phi_{in}^+|^2}{|\phi_{in}^+|^2} \quad . \quad (3.20)$$

These are plotted in Figs. 3.4(a) and (c) for a device with the parameters above.

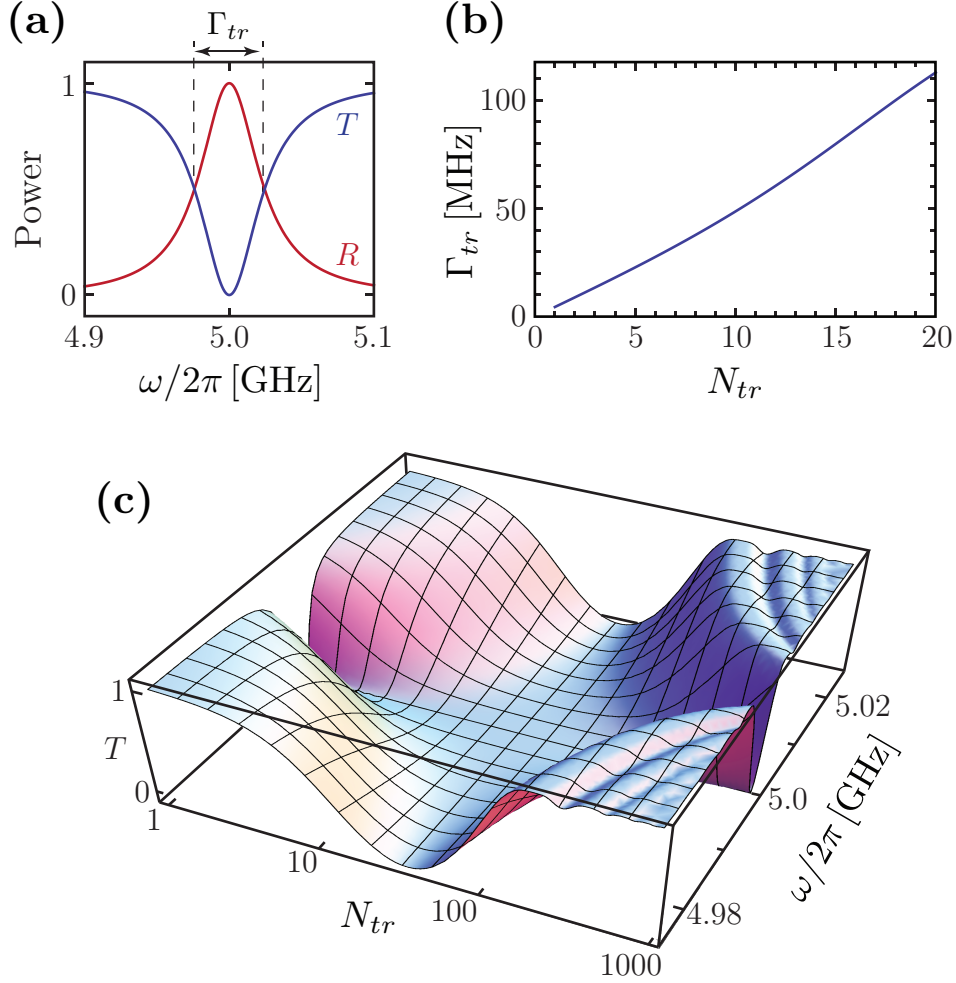


Figure 3.4: Coupling of SAW to a transmon with $\omega_0/2\pi = 5$ GHz and $E_J/E_C = 40$. (a) SAW power transmission (T) and reflection (R) for $N_{tr} = 10$. (b) Coupling frequency Γ_{tr} versus the number of transmon finger pairs, N_{tr} . (c) Power transmission as a function of N_{tr} and frequency. For low N_{tr} , the electrical resonance dominates, and its width along the frequency axis gives Γ_{tr} . For $N_{tr} \gtrsim 50$, the width of the resonance peak is limited by the acoustic properties of the transmon. In practice, $N_{tr} \approx 50$ is an upper limit, since a higher value produces unfeasibly small W_{tr} given the fixed C_{tr} .

The coupling frequency Γ_{tr} is given by the width of the power reflection/transmission peak, which is plotted in Fig. 3.4(b) as a function of N_{tr} for fixed C_{tr} . Γ_{tr} determines the rate at which the a quantum $\hbar\omega$ can transfer between the qubit and the coupled system, in this case the Rayleigh modes in the substrate around ω_0 . From the calculation above we find

$$\Gamma_{tr} \approx N_{tr} \times 4.4 \text{ MHz} \quad . \quad (3.21)$$

A similar calculation is presented in Sup. Disc II of Paper I , where the coupling was considered all the way from the electrical transmission line to the qubit through an IDT. That calculation gave a slightly different, and not perfectly correct, value of $\Gamma_{tr} = N_{tr} \times 3.7 \text{ MHz}$. The simpler calculation above is more representative than the one in the paper, since the coupling is an inherent property of the qubit and the SAW transmission line, and does not depend on what IDTs or probes are used to interact with the SAW. In a realistic experiment, the qubit would be excited from an IDT, and the transmitted SAW would be studied either with an IDT or with a local probe.

3.7 Conclusions and outlook

Using an RF-SET as a local probe, we were able to detect SAW at very low levels, both in terms of energy and mechanical displacement. In approach of the quantum limit, the SET back-action may prove to give too much back-action, but quantum devices that use the same type of charge coupling in a parametric process should be able to circumvent this.

The coupling of SAW to a superconducting qubit is particularly interesting, since this could allow the production of non-classical acoustic states. These should have properties in common with propagating photonic states, but be more accessible to study due to their lower speed and stronger coupling to matter. Ideas along these lines are further developed in Sup. Disc. II of Paper I .

Chapter 4

Charge noise in SETs

The basic properties of charge noise are described in Sec. 2.1.3. In the studies presented here, we set out to investigate how the noise varies with temperature, bias conditions and external electric fields, in order to get an indication of what processes govern its generation. By studying how the noise sources thermalize with the SET and the surrounding materials, we can gain information about their fundamental properties, without making strong assumptions about their microscopic origin. We also studied the relaxation of charge TLFs after large potential steps were applied to the SET gates. By describing the TLFs in terms of a complex susceptibility, we can relate the step response to the charge noise.

The experimental work was done in collaboration with Arsalan Pourkabirian (A.P.), initially with the author in a more supervisory role, and a large part of the credit goes to him. The theoretical analysis has been a collaborative effort, with substantial contributions from Göran Johansson (G.J.) and Per Delsing – particularly on the microscopic modeling of TLFs and their susceptibilities – as well as John Clarke. We also received valuable help from Thilo Bauch and Joachim Lublin (J.L.). The results shall be disseminated in two journal articles, one of which has been submitted and is part of this thesis (Paper II).

4.1 Experimental setup

The SETs were fabricated by A.P. using two-angle evaporation of aluminum on an Si substrate covered with 400nm of thermal SiO₂. Five SETs were deposited on each chip, in the geometry shown in Fig. 4.1. We strived to achieve high charging energies in the SETs, in order to use them also at high temperature, and some devices had $E_C/k_B > 10$ K. Two nominally identical chips were fabricated and measured, each in a separate measurement run, henceforth denoted MR1 and MR2.

The chips were cooled in a dilution refrigerator (“Mr Freeze”) with a base temperature of $T_0 < 20$ mK, fitted with extensive low-pass filtering of the measurement lines at the mixing chamber. The aluminum of the samples was held in the non-superconducting state by means of a magnetic field from a superconducting magnet in persistent-current mode, of 0.6 T for MR1 and 1 T for MR2.

Fig. 4.2 shows a schematic of the total measurement setup. The details of the setup evolved during the course of the experiment, in order to optimize its performance. The SETs were voltage biased symmetrically with respect to the refrigerator ground by two custom-built battery-powered transimpedance amplifiers (TIAs), which measured the current I_{SET} passing

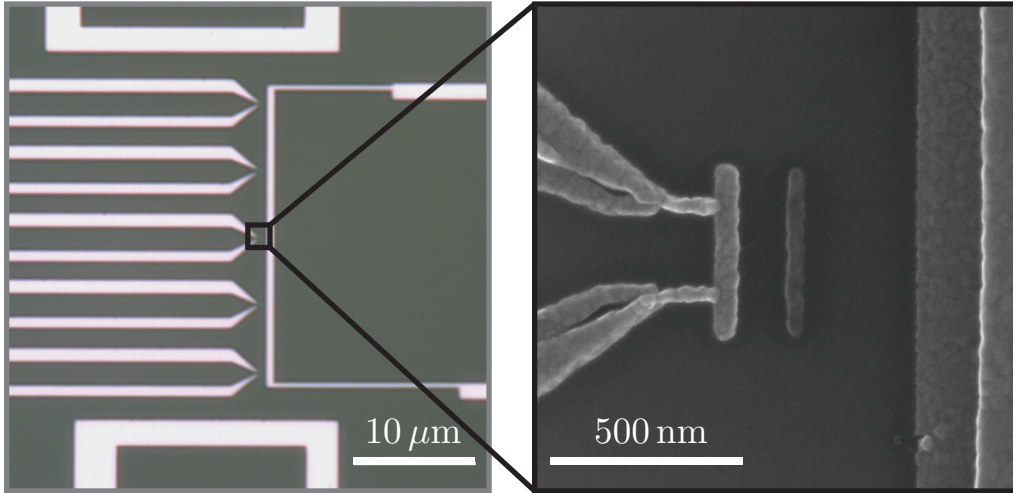


Figure 4.1: Layout of the SETs used for charge noise measurements. The chip contains five SETs, separated by $5\ \mu\text{m}$ and placed a distance of $600\ \text{nm}$ from the main gate, which is common to all the SETs. Apart from the main gate, there are two side gates, seen at the top and bottom, used to apply a more global electric field to the devices. The island is approximately $70\ \text{nm}$ by $500\ \text{nm}$, with a film thickness of $30\ \text{nm}$.

through the SET differentially. The amplifiers were constructed by J.L. as part of his MSc project, based on the work of Björn Starmark [105]. After post-amplification and filtering, the current signal was routed to a Keithley 2001 voltmeter and (for MR1) an SR785 dynamic signal analyzer (DSA) or (for MR2) a PXI-6259 data acquisition card.

The refrigerator is installed in an electrically shielded room, and we took care to avoid ground loops and other sources of interference. We used battery-powered SIM928 low-noise voltage sources from Stanford Research Systems (SRS) to bias and gate the SETs, through voltage dividers at room temperature. On top of the DC gate signal, an AC signal known as the “pilot” was applied at a frequency of $f_p = 377\ \text{Hz}$, with an amplitude corresponding to a known fraction of an electron charge induced on the SET island. A DS345 function generator from SRS was used to supply the pilot signal, chosen because its output can float with respect to ground.

We acquired current spectra in a frequency range from $1\ \text{Hz}$ to $401\ \text{Hz}$, either directly with the dynamic signal analyzer or by Fourier-transforming a signal sampled with the data acquisition card. Each final spectrum was averaged between $10\ \text{s}$ and $1\ \text{min}$. We compensated the data for a slight roll-off in the amplifiers, which have bandwidths of $\sim 1\ \text{kHz}$, and subtracted the calculated amplifier noise and shot noise [Fig. 4.3]. The shot noise was calculated as $e I_{SET}$, *i.e.* with the Fano factor $F = 0.5$ as for uncorrelated tunneling. This gives the correct value at high currents and high temperatures, which is the situation when the shot noise may influence the results. Since the amplifier noise depends on both source impedance and gain, we used calculated values in the analysis [105], which agree with measurements. After these compensations, we normalized each spectrum to the acquired level of the pilot signal, in order to null out variations and drift in the charge-to-current gain $\delta I_{SET}/\delta Q_g$ of the SET. Before

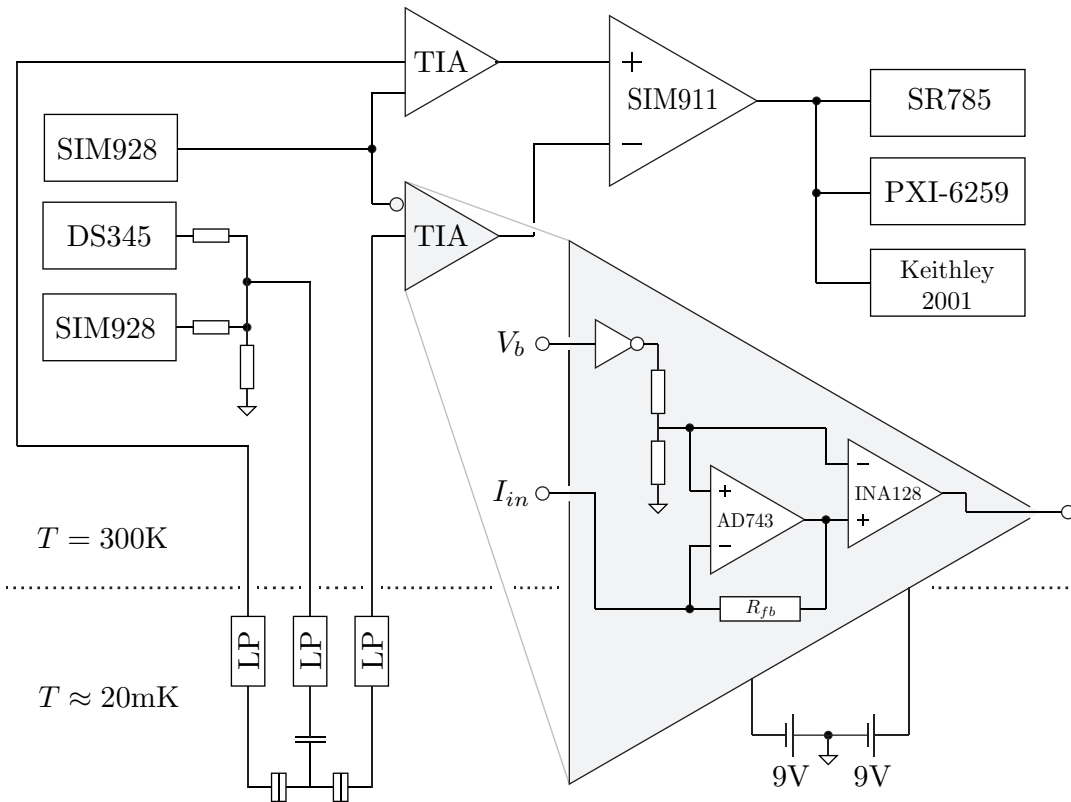


Figure 4.2: Experimental setup for measuring charge noise in SETs. The boxes labeled “LP” represent the low-pass filters in the refrigerator. For the most recent batch of measurements, the setup was doubled, so that two SETs could be measured at the same time. The transimpedance amplifiers (TIA) were constructed and built by J.L. The SIM928 is a battery powered voltage source, the SIM911 a voltage amplifier, SR785 a signal analyzer and the DS345 a function generator, all supplied by Stanford Research Systems. The PXI-6259 is a data acquisition card from National Instruments, and the Keithley 2001 a digital voltmeter. This schematic shows the basic measurement setup, but additional modules were inserted in the signal chain at various times, in efforts to maximize the measurement performance.

each spectrum was acquired, we measured I_{SET} while sweeping the gate voltage over several modulation periods, in order to find the operating point which maximizes dI_{SET}/dQ_g . In practice, we used the point where the current was midway between the lowest and highest points on the modulation curve. The exception to this is the measurements of noise as a function of V_b and I_{SET} , where we adjusted the gate to give a specific current value, rather than to maximize the charge gain. The DC current was monitored continuously during spectrum acquisition, and we measured the refrigerator temperature before and after each spectrum was acquired. In all cases, Matlab software was used to control the measurements and acquire data.

In order to compare different noise spectra, we need to compute a single characteristic value \tilde{S}_Q to represent the noise level of each spectrum. It is common to compare $1/f$ noise at arbitrarily chosen frequencies of 1 Hz or 10 Hz, and some authors have extracted the noise level by fitting a $1/f$ function to the full measured spectrum [51, 55]. A complication in this analysis is the presence of individual strongly-coupled TLFs, which may dominate the spectrum in certain frequency ranges. Although it is possible to extract some important information about the microscopic nature of the noise sources from such a TLF, we are primarily interested in the smooth $1/f^\alpha$ part of the noise spectrum.

The measurements presented in Paper II were concentrated on one SET (with $E_C/k_B = 10.9$ K and $R_\Sigma = 368$ k Ω , denoted S1 in the paper), where the contribution from a strongly-coupled TLF with $\omega_0 < 100$ Hz was visible at high temperature. At low frequency, the measured spectra are inaccurate due to the short acquisition time, and we did not deem it possible to fit the data with a Lorentzian superimposed with the $1/f^\alpha$ contribution, without introducing too many new assumptions. To minimize the influence of the Lorentzian, we instead evaluated \tilde{S}_Q at the high end of the measurement bandwidth, by taking the average value of $S_Q(f)$ for $383 \leq f \leq 401$ Hz, *i.e.* for frequencies above f_p . We found this method to be robust, and to produce low scattering between data points acquired with similar temperature and bias.

4.2 Thermal properties of charge noise

In Paper II, we primarily investigated the thermal properties of TLFs, and how they relate to the self-heating of the SET. The temperature dependence of charge noise has been measured previously by several authors [36, 48, 49, 52, 55, 57], and we sought to repeat such a measurement with higher precision, in order to draw strong conclusions about the nature of the noise sources.

A common approach to temperature-dependent cryogenic measurements is to use a PID-regulated heater to balance the cooling power of the refrigerator. The cooling power is, however, strongly and non-linearly dependent on temperature, which makes it difficult to regulate T_0 over a large range, and the long stabilization times limit the time available for measurements. After some attempts along this route, we chose instead to start with the refrigerator at base temperature and warm it up in a slow and continuous sweep (~ 20 h), repeating a fast noise measurement many times during the warm-up. We measured the noise of several SETs during such temperature sweeps, and consistently found that the noise level increased linearly with temperature. This was the case also when strong electric fields were applied around the SET, either from the main gate or between the two side-gates.

Like many authors before us [36, 48, 49, 51, 52, 54, 55], we found that the noise saturates

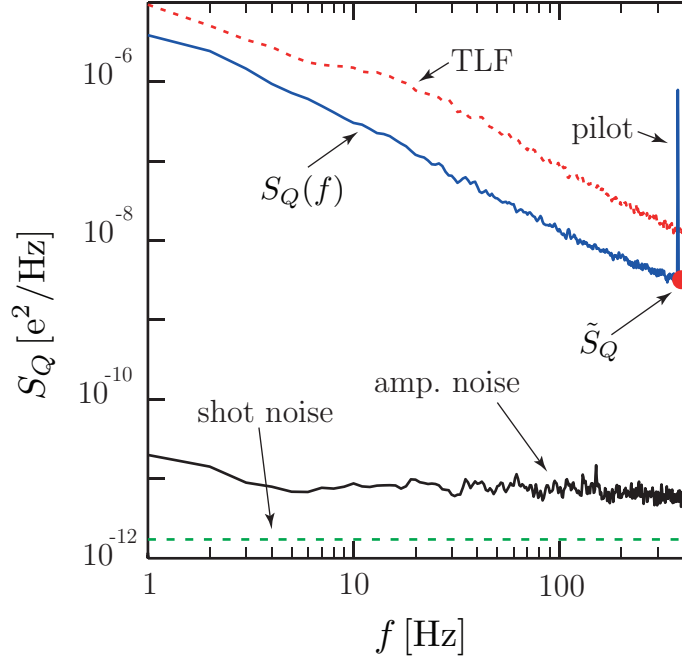


Figure 4.3: Charge noise spectra: The blue curve shows a typical charge spectrum at low temperature, with the pilot signal at $f_p = 377$ Hz. The dashed red curve was acquired for the same device at higher temperature of $T_0 \approx 1.5$ K. The bend in the spectrum is due to a strongly-coupled TLF superimposing a Lorentzian spectrum on the $1/f^\alpha$ noise that we wish to study. The Lorentzian cut-off frequency tends to increase with temperature. To be able to compare different spectra with minimal influence from this Lorentzian, we calculate \tilde{S}_Q as the average noise in frequencies between 383 Hz and 401 Hz. The lower bound of this range was chosen to ensure that \tilde{S}_Q is not influenced by the pilot signal. The black curve is the total amplifier noise measured with open inputs of the TIAs, for a gain of $10\text{ M}\Omega$. The dashed green line is the calculated shot noise. The amplifier noise and shot noise have been converted to charge units using the charge gain of the SET, determined from the pilot signal.

to a constant level at low temperature. This saturation has been tentatively attributed to self-heating of the SET, which would affect the sources of the charge noise [36]. However, it is primarily the *electrons* on the SET island which are heated, and it has not been clear how the charge fluctuators, which are external to the SET island, would couple thermally to the SET electron gas. Alternative theories have been put forward, such as a mechanism where switching between TLF states occurs by quantum tunneling at low temperature [36], or excitations either from external photons [50] or from the electrons tunneling through the SET. The latter type of excitation could be either in the form of inelastic scattering between electrons and TLFs in the junction barriers [36, 57] or absorption of energy from the voltage shot noise on the SET island [49].

In order to find out the reason for the saturation, we did a temperature sweep as described above, while at the same time altering between three values of the SET bias voltage. From this measurement, we could clearly see the saturation level of the noise increase with SET bias. In this regime, we also see that the noise level increases according to $\tilde{S}_Q = \beta T$, as discussed in Paper II. From this, we can rule out that the saturation is caused by a quantum mechanical tunneling between the TLF states or by external photons, since neither process should have a strong dependence on SET bias.

As the temperature is elevated, the noise is the same independent of SET bias. This indicates that the same TLFs are activated by the SET bias as by the refrigerator temperature.

To elaborate on this, we measured the noise at 315 bias points with the refrigerator at its base temperature, adjusting V_b and I_{SET} independently. For each data point, V_b was fixed and we swept the SET gate to find out what gate voltage to apply to get the desired current. After fixing the gate at this voltage, we did not alter the bias during the spectrum acquisition. In order to null out drift in measurement parameters and the noise generators, we applied the bias points in (pseudo-) random order.

These data can be processed in several ways. First, we can compare the measured noise with what we would expect if the TLFs were activated by shot noise from the SET. The spectrum of the shot noise depends in a non-trivial way on bias voltage, current and temperature, and has been calculated by G.J. *et al.* in Ref. [34]. The noise power at negative frequencies can supply photons to other systems that couple electrically to the SET island, such as the TLFs, allowing them to be excited out of thermal equilibrium. Fig. 4.4(a) shows the shot noise power integrated over all negative frequencies, $S_{V,exc}$ for an SET with approximately the same parameters as the one used in the experiment. For comparison, the measured charge noise as a function of V_b (with the same data as in Fig. 3(a) of Paper II) is plotted in Fig. 4.4(b). For both high and low electron temperature, we see that $S_{V,exc}$ decreases with V_b for low V_b , whereas our measurements show an increase in \tilde{S}_Q with V_b . We conclude from this that excitation by the SET shot noise is not likely to be the reason for the saturation.

Next, we can consider the hypothesis of Kenyon *et al.* [36, 57], that the tunneling electrons scatter inelastically against TLFs in the tunnel barriers. In this scenario, we expect each tunneling electron to be able to excite TLFs with activation energies up to $\sim eV_b/2$. With a uniform distribution of activation energies (as generally assumed in microscopic TLF models), the number of accessible TLFs should then scale with V_b , as well as with the rate of tunneling, *i.e.* I_{SET} . The relaxation rate of the activated TLF can be assumed to dominate over its excitation rate, and then the noise power scales with the excitation rate [45]. Hence, this mechanism should yield $S_Q \propto V_b |I_{SET}|$.

While we do observe a monotonic dependence of \tilde{S}_Q on $P_{SET} = V_b |I_{SET}|/2$, it is much weaker than we expect from the inelastic-scattering model. The weak power law indeed

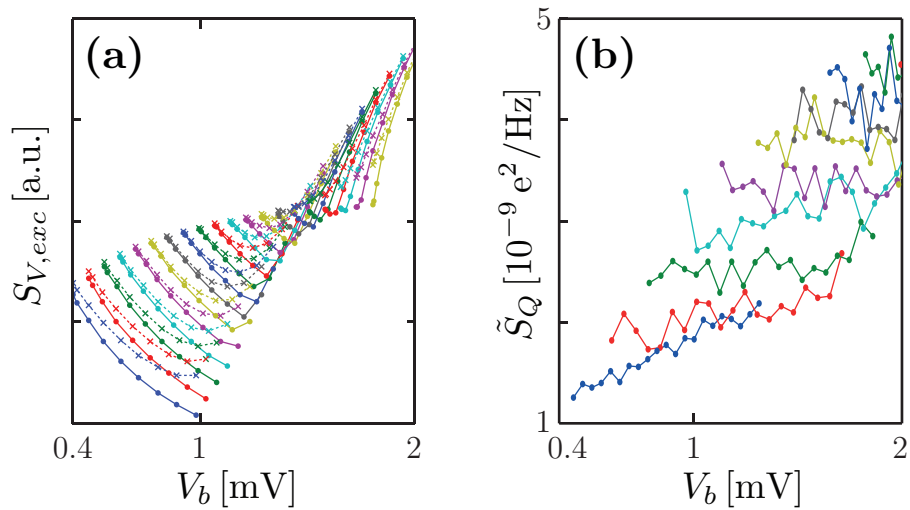


Figure 4.4: Comparison of SET shot noise power to charge noise. **(a)** Calculated shot noise power integrated over all negative frequencies (capable of exciting TLFs) as a function of SET bias, calculated by G.J based on experimental SET parameters. The lines connect points with the same Q_g , within the range $0 < Q_g \leq 0.5 e$, with the lowest I_{SET} giving the lowest noise power. Points and solid lines are calculated for an electron temperature of $T_e = 50 \text{ mK}$ and crosses and solid lines for $T_e = 1.5 \text{ K}$. **(b)** Charge noise measured in the SET as a function of V_b , for a range of values of I_{SET} . This plot uses the same data as Fig. 3(a) in Paper II. Comparing the two panels, especially at low I_{SET} , we see a decrease in shot noise power with V_b , but an increase in the level of charge noise.

resembles the dependence expected for the temperature of the thermalized SET electron gas on P_{SET} , according to Eq. 2.3.

$$P = \Sigma\Omega(T_e^n - T_{ph}^n) \quad . \quad (2.3)$$

Under the assumption that the saturation is indeed caused by heating of the noise sources above the refrigerator temperature, we can use the linear dependence we measured for \tilde{S}_Q on T_0 to estimate the temperature of the TLFs affecting the SETs. Thus, there are three temperature scales that we wish to compare:

- The electron temperature on the SET island.
- The phonon temperature in the substrate.
- The temperature of the TLFs, as estimated from our noise measurements.

Our initial attempts at determining the electron temperature of the SET used a numerical SET simulator written by G.J., which self-consistently calculates the temperature of the island electron bath with electron-phonon ($e-ph$) thermalization taken into account. The simulator confirms that almost all the power dissipated in the SET is emitted as phonons. We attempted to find the parameters Σ and n , which give the thermalization power through Eq. 2.3 by fitting simulations to SET stability diagrams acquired at base temperature. However, due to the weak dependence of the electron temperature Te on the dissipated power P_{SET} , these fits did not have sufficient accuracy for us to draw strong conclusions, although we found that values reported in the literature could reproduce the stability diagram well. To find the electron temperature as a function of power dissipated by the SET, we used instead Eq. 2.3 with $n = 5$ and $\Sigma = 0.4 \text{ nWK}^{-4}$ taken from [22], assuming low temperature of the SET leads and the phonon bath. At the time Paper II was submitted, we were not aware of the recent work by Underwood *et al.* [24], where the $e-ph$ thermalization in Al is discussed in more detail. The results of this paper are consistent with our model.

To determine the temperature in the substrate, we use a Finite Element Method calculation, implemented in Comsol. To save computational resources, the model is axi-symmetric, with the SET represented as a disc with radius $\sqrt{\frac{A_{SET}}{\pi}} = 106 \text{ nm}$, to give the same contact area A_{SET} with the substrate as in the actual device. Assuming that all the power dissipated in the SET is transferred to the substrate (*i.e.* no power is lost by tunneling of hot electrons), that the thermal conductivity is isotropic, and that the thermal interface barrier (Kapitza resistance) between Si and SiO₂ can be neglected, we can solve this model for the substrate's temperature distribution in the vicinity of the SET.

The thermal conductivity of silicon oxide has been studied carefully, and its temperature dependence has been found to be independent of the microscopic specifics of the material or any external factors, and remarkably similar for a range of amorphous materials [106]. From [106], we get $\Lambda_{\text{SiO}_2} = 0.03T^2 \text{ Wm}^{-1}\text{K}^{-3}$. For the underlying silicon, the $\Lambda \propto T^3$ dependence of the Debye model explains the thermal conductivity well, to within a prefactor that may depend on such factors as crystal doping. In our model, we used $\Lambda_{\text{Si}} = 5.0T^3 \text{ W/mK}^4$, from [107]. Since the thermal conductance is much higher in Si than in SiO₂, and the SiO₂ layer is thick on the scale of the SET island, Λ_{Si} has relatively little impact on the thermalization of the SET.

The model is illustrated in Fig. 4.5, along with a solution for the temperature distribution at an SET power of $P_{SET} = 5 \text{ pW}$ and a refrigerator base temperature of $T_0 = 20 \text{ mK}$. The

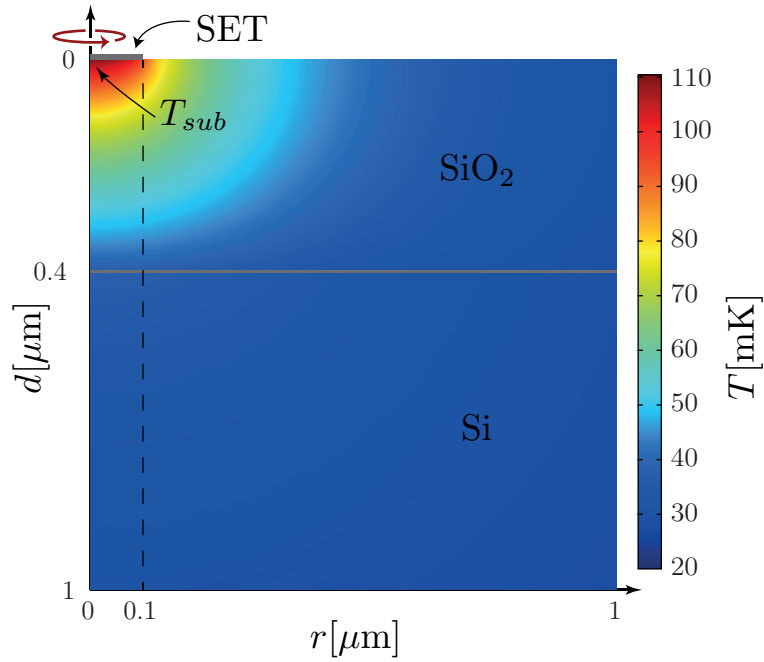


Figure 4.5: Finite Element Method calculation of the substrate temperature under the SET, as a function of radial coordinate (r) and depth (d). In this axially symmetric model, the SET is represented as a line at the surface from the origin to $r = 106$ nm, and it is clear that the substrate temperature deviates from 20 mK only in the SiO₂ layer very close to the SET. In the calculation, the substrate extends $60 \mu\text{m}$ along both axes, where the temperature is assumed to be $T_0 = 20$ mK.

highest temperature, denoted T_{sub} is found at the center of the island, at the interface between the SET and the underlying SiO_2 .

We thus have estimates for the three temperatures in the system: That of the electron gas, T_e , that of the substrate closest to the SET (T_{sub}), and that of the charge noise sources, T_{TLF} , all as a function of the power dissipated on the SET island. Plotting these three together (Fig. 3 of Paper II), we find that the temperature of the noise sources is lower than the SET temperature by approximately a factor 4, but warmer than the warmest part of the substrate by approximately the same factor. Even though the thermal models are not accurate, these differences are large enough to be significant.

It would not be remarkable if the TLFs had been found to follow the local temperature of the substrate. Their substantially elevated temperature, however, leads to the conclusion that the TLFs are thermally coupled directly to the electron gas of the SET island without the intermediary of substrate phonons, or that they reside in a region with a higher phonon temperature than any point in the bulk of the substrate. Such regions include the oxide on the outside of the SET and in the junction barriers.

We do not have support for any particular microscopic TLF model that would follow this pattern of thermalization. We can, however, speculate that the noise is caused by a process where the TLF charge is not bound in a double-well potential, but tunnels between the SET island and an external potential well. Kafanov *et al.* [60] proposed such a model, where the external wells are the microscopic grains produced upon two-angle evaporation of Al, but this cannot explain the charge noise observed in devices fabricated by other methods. Recent data, although not fully conclusive, did not show any dependence on the perimeter length of the junctions of Al SETs, as would be expected from this model [108]. It is known that the disorder in the interface between metals and amorphous insulators can give rise to potential wells, known as Metal-Induced Gap States (MIGS), which are able to trap electrons for extended times. It has recently been proposed that the flux noise observed in SQUIDS is caused by such trapped electrons flipping their spin stochastically. We can speculate that electrons may tunneling in and out of the same kind of traps, thereby producing the charge noise.

It is also possible that the TLFs are located in the junction barriers, where they would experience the wavefunctions of the hot SET electrons. However, our measurements on the step response of an SET, discussed in Sec. 4.3 indicate that that the TLFs are affected directly by the SET gate voltage. This would not be the case if they were located inside the junctions.

4.3 Descriptions of TLFs and their susceptibility

In the TLF model presented by Dutta & Horn [46], the transitions between TLF states are assumed to be thermally activated, with each TLF having a single characteristic activation energy E_{TLF} and a Lorentzian cut-off frequency

$$\omega_0 = \omega_0 e^{-E_{TLF}/k_B T} \quad . \quad (4.1)$$

Under the assumption that the activation energies are uniformly distributed for the TLF ensemble influencing the device, this model produces $1/f$ noise which scales linearly with temperature.

The model was originally meant to describe the conductance noise in semiconductors [63], where moving carriers are caught by a defect or a surface state, represented by a single

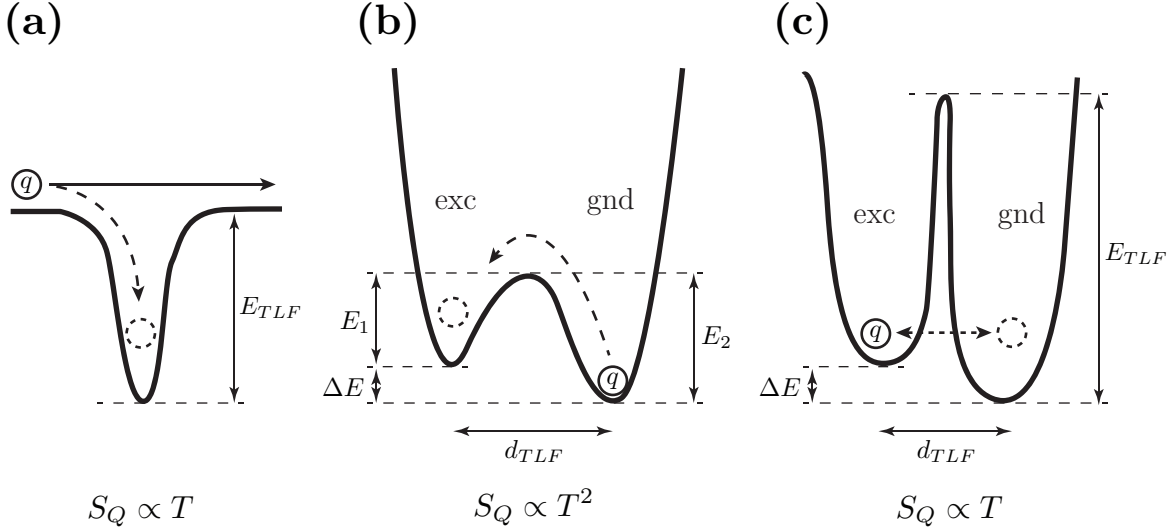


Figure 4.6: Different models for TLFs. **(a)** A resistance fluctuator as described by Dutta & Horn [46, 63]. A propagating electron may get trapped in a potential well, and needs to be thermally activated to the energy E_{TLF} in order to escape. When trapped, the electron repels other electrons which leads to an increase in resistance. **(b)** The double-well potential treated by Kenyon *et al.* [36, 57]. The charged particle is thermally excited over the barrier in both directions, which leads to $S_Q \propto T^2$. The two states couple the charge q_{TLF} with different strengths to the SET. **(c)** The model treated in this section. The charged particle tunnels through the central barrier, while remaining in thermal equilibrium. The probabilities are P_g and P_e to be in the ground state and the excited state, respectively. In all three panel, “ q ” is short for q_{TLF} .

potential well of depth E_{TLF} as illustrated in Fig. 4.6(a). As such, it does not fit perfectly with plausible microscopic descriptions of charge TLFs in insulators.

The common way to represent a charge TLF is instead as a single charged particle moving stochastically between two coupled wells, as illustrated in Fig. 4.6(b). This was treated by Kenyon *et al.* [36, 57], who proposed a modification to the Dutta & Horn model where the potential is characterized by two activation energies, one for each direction of switching. Assuming that the two potential wells are independently and uniformly distributed and that the transitions are thermally activated over the middle barrier, the authors predict a temperature dependence of $S_Q \propto T^2$. This was also supported by their measurements, as well as those of other authors [48, 49, 55].

As an alternative, we can model a TLF where the transitions occur by tunneling through the central barrier, the height E_{TLF} of which greatly exceeds both the thermal energy and the energy asymmetries ΔE between the two states. Such a TLF model is illustrated in Fig. 4.6(c). In thermal equilibrium, the transition rates to the excited state (Γ_{\uparrow}) and to the ground state (Γ_{\downarrow}) satisfy detailed balance:

$$\Gamma_{\uparrow} = \Gamma_{\downarrow} \frac{P_e}{P_g} = \Gamma_{\downarrow} e^{-\Delta E/k_B T} \quad . \quad (4.2)$$

The occupation probabilities of the ground state (P_g) and the excited state (P_e) are given by

$$P_g = \frac{1}{1 + e^{-\Delta E/k_B T}} \quad , \quad P_e = \frac{1}{1 + e^{\Delta E/k_B T}} \quad . \quad (4.3)$$

Under these conditions, the Lorentzian spectrum of Machlup (Eq. 2.5) can be written as

$$S_{Q,Lor} = (\kappa q_{TLF})^2 P_g P_e \frac{\omega_0}{\omega_0^2 + \omega^2} = (\kappa q_{TLF})^2 \cosh^{-2} \left(\frac{\Delta E}{2k_B T} \right) \frac{\omega_0}{\omega_0^2 + \omega^2} \quad (4.4)$$

where κ is a coupling factor between the TLF and the SET, such that the difference in charge induced on the SET from the two TLF states (*i.e.* the amplitude of the telegraph signal) is κq_{TLF} . The Lorentzian cut-off frequency is set by $\omega_0 = \Gamma_\uparrow + \Gamma_\downarrow$. For a big ensemble of TLFs with uniformly distributed ΔE ,

$$\int_{-\infty}^{\infty} \cosh^{-2} \left(\frac{\Delta E}{2k_B T} \right) d\Delta E = 4k_B T \quad (4.5)$$

so the factor $P_g P_e$ gives a linear temperature dependence of the noise power even if ω_0 is independent or only weakly dependent on temperature, as expected for tunneling through a high barrier.

Under an externally applied electric field \mathbf{E} , there is a shift in ΔE :

$$\Delta E(\mathbf{E}) = \Delta E(0) + q_{TLF} \mathbf{E} \cdot \mathbf{d}_{TLF} \quad (4.6)$$

where \mathbf{d}_{TLF} is the physical separation between the two potential wells. By treating an oscillating perturbation of ΔE , it is possible to calculate a complex susceptibility

$$\chi_{TLF} = -\frac{q_{TLF}^2 d_{TLF}^2 n_{TLF}}{4\epsilon_0 k_B T} \cosh^{-2} \left(\frac{\Delta E}{2k_B T} \right) \frac{\omega_0^2 + i\omega\omega_0}{\omega_0^2 + \omega^2} \quad (4.7)$$

for an ensemble of identical TLFs with a spatial density n_{TLF} , which satisfies

$$\mathbf{P} = \epsilon_0 \chi_{TLF} \mathbf{E} \quad . \quad (4.8)$$

Comparing Eq. 4.7 with Eq. 4.4, we have

$$S_{Q,Lor}(\omega) = -\frac{4\epsilon_0 k_B T}{n_{TLF} d_{TLF}^2 \omega} \kappa^2 \text{Im}(\chi_{TLF}) \quad . \quad (4.9)$$

To get the total noise, we need to sum over an ensemble of such TLFs with different ω_0 and integrate the contributions from all TLFs surrounding the SET, taking the spatial distribution $n_{TLF}(\mathbf{r})$ and the position-dependent coupling, $\kappa(\mathbf{r})$ into account. As discussed by Dutta & Horn, a logarithmic distribution $D(\omega_0)$ of ω_0 (a fixed number of TLFs per decade of frequency) produces perfect $1/f$ noise. Since the tunnel rate decreases exponentially with the height and width of the central barrier, this is consistent with a uniform distribution of barrier heights E_{TLF} . However, even distributions that deviate substantially from the logarithmic one produce $1/f^\alpha$ noise with $\alpha \approx 1$.

4.4 Step response of charge TLFs

The original plan of MR2 was to measure the temperature dependence of the charge noise also in the presence of strong electric fields from the gate and the side-gates. In the process, we found that the sudden application of such a field not only caused the SET working point to instantly move many periods along its modulation function, but that the working point kept slowly increasing for many hours after the field was applied. Similar behaviour has been observed previously for SETs made from highly doped silicon, but on much shorter timescales [109]. Slow drift of the SET offset charge is a known phenomenon, and has been studied previously, although it has usually been treated as a separate process from the $1/f$ charge noise [110, 111].

We proceeded to measure the response of the SETs both to steps in the gate voltage and differential steps applied to the side-gates, at different temperatures. These experiments were all done in the second measurement run, MR2, where we sampled the SET current at 20 kSamples/s. Fig. 4.7 shows an example of the SET current after the main SET gate was stepped from -4.9 V to 4.9 V, along with the extracted values for the induced island charge, after compensation for the big charge jumps. Each period in I_{SET} corresponds to one additional electron induced on the SET island. The data were acquired for 10 – 20 h after application of the step.

It seems plausible that the slow charge relaxation is due to the same type of TLFs that cause the charge noise, and their response can then be described by the susceptibility χ_{TLF} of Eq. 4.7.

For a medium of TLFs embedded in an ideal dielectric with susceptibility χ_i , the response to a change in gate voltage is given by

$$Q_g(t) = \epsilon_0 G \mathfrak{F}^{-1}[(\chi_{TLF} + \chi_i + 1) \mathfrak{F}(V(t))(\omega)](t) \quad (4.10)$$

where G is a geometry factor (*e.g.* $G = A/d$ for a plate with area A parallel to the SET island at a short distance d). With $V(t) = V_0\Theta$ and Θ a step function from 0 to 1 at $t = 0$, and ignoring the instantaneous contributions from the ideal dielectric, χ_{TLF} gives a response of:

$$Q_g(t) = G \epsilon_0 \frac{d_{TLF}^2 n_{TLF} q_{TLF}^2}{4\epsilon_0 k_B T \cosh\left(\frac{\Delta E}{2k_B T}\right)^2} (1 - e^{-\omega_0 t}) V_0 \Theta(t) \quad . \quad (4.11)$$

In the same way as for the charge noise, the total step response is calculated by summing the contributions from many TLFs with different ΔE and ω_0 . We find that the shape of the expected response fits with the data, although some work remains to treat the true geometry of the sample and determine the distribution of TLFs.

4.5 Conclusions and outlook

Our data show that the TLFs are in thermal equilibrium, and that the saturation level of the noise observed in SETs at low temperature is caused by self-heating. They further indicate an unexpectedly strong thermal coupling between the electron gas on the island of an SET and the ensemble of TLFs that generate charge noise in the same device, which in turn speaks for a model where the TLFs are located in the interfaces between the SET island and the surrounding insulators. Extending the experiments to SETs deposited on different substrate

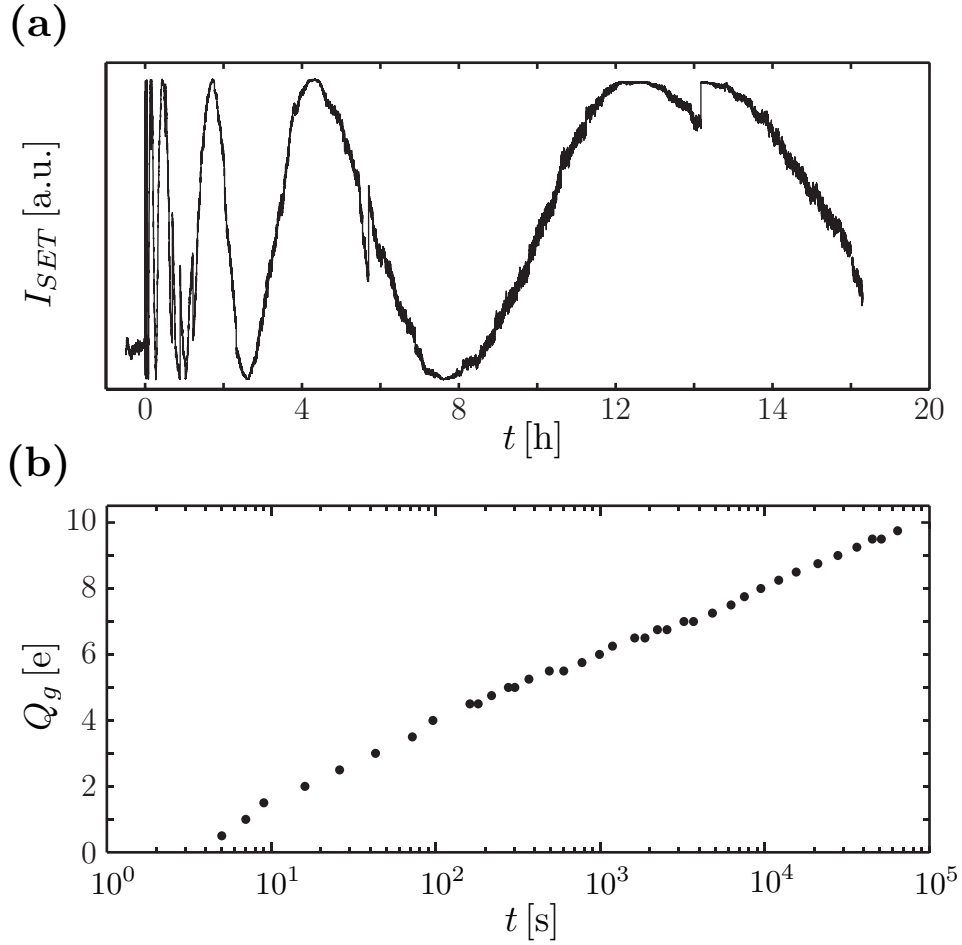


Figure 4.7: Response of an SET after the gate voltage was stepped from $V_g = -4.9$ V to $V_g = 4.9$ V at $T = 50$ mK. **(a)** The SET current, oscillating one period for every electron induced on the island. **(b)** Charge induced on the island, extracted from the peaks and valleys in (a), in addition to the ideal contribution of the gate dielectric. Since the first few oscillations are too fast to be resolved, we cannot say with certainty how large the contribution is from the TLFs.

materials, as well as suspended devices, would be a natural continuation of the experimental work. In particular, a suspended SET with the island made of a noble metal – without surface oxide – should have very little charge noise if our hypothesis is correct.

The measurements of charge relaxation in SETs must be analyzed further before we can conclude whether this is caused by the same TLFs as the charge noise. If this can be proven to be the case, systematic studies of the full susceptibility of the TLF ensemble may provide some further insight into its microscopic nature.

Chapter 5

Photon detection with SETs on heterostructures

Many competing techniques exist to detect individual photons at or around optical wavelengths. Different applications for single-photon detection have different demands, and the various existing detector techniques have their particular advantages and drawbacks. For low-intensity image capture, avalanche silicon diodes dominate [112], since they are fast and can be fabricated in arrays by methods compatible with standard CMOS, and work from the infrared up through the visible spectrum. Silicon diodes also find plenty of use in quantum-optical experiments, where many counts can be averaged and the relatively high noise and low quantum efficiency are not problematic.

For certain purposes, such as quantum cryptography and related experiments, high quantum efficiency must be combined with a low rate of dark counts [113]. That is, nearly all incoming photons must be detected, but in the absence of photons, there must be as few false alerts as possible. It is also desirable to combine these properties with number-resolution, *i.e.* the capability to determine whether a light pulse contains one, two, three or more photons. In this segment, superconducting bolometers have made rapid progress, particularly devices of the Transition Edge Sensor (TES) variety [114–116]. These use a small and thermally insulated piece of superconductor material, biased on the verge between the superconducting state and the normal state. This phase transition is sharp enough that the heat from a single absorbed photon produces a measurable increase in the resistance of the material. Modern TES bolometers can be number resolving, but there is generally a trade-off between the efficiency and the area available for photon absorption.

The approach to single photon detection presented here competes for the same application segment as TES, but uses a rather different technique: Instead of converting incoming photons to heat, photons impinge on the surface of a semiconductor heterostructure, each generating an electron-hole pair in a two-dimensional potential well. The electron and the hole are thus confined vertically to a layer near the semiconductor surface, where they can be laterally separated and transported to dedicated detection regions, for RF-SETs to detect their charges. The concept of using SETs for photon detection was first demonstrated in Ref. [117]. Primarily, we strived to use the potential of a Surface Acoustic Wave (SAW) to separate and transport the carriers, but also made attempts to guide them with electric field gradients generated by resistive electrodes on the substrate surface. The prototypes investigated were all based on GaAs, for operation at wavelengths around 800 nm, but the technique can

be generalized to other material systems with different optical properties, such as Si or InP. Due to the high charge sensitivity of the RF-SET, this approach should allow number-resolved photon detection with a quantum efficiency above 90% and a negligible rate of false counts. Compared with TES, the advantages are a bigger absorption area and the ability to operate at higher temperatures, limited only by the charging energy of the SET. To test the samples, we fitted a He-3 refrigerator with RF equipment, optical fibers, and a custom sample holder where the cleaved end of a fiber can be mounted just above the sample surface (see Sec. 2.3).

These developments all took place within the EU project “ACDET II”, a collaboration between Cambridge University, UK; Paul Drude Institute für Festkörperelektronik (PDI), Germany; Bristol University, UK; Universidad de Valencia, Spain; Alcatel Thales III-V Lab, France; and Chalmers. The details of the proposed design are discussed in Paper III .

5.1 Heterostructures

Crystalline compounds made from elements in the third and fifth column of the periodic table, such as GaAs and InP, are of great technological importance. They tend to be semiconducting with direct bandgaps, making them useful in electro-optical devices, and their high carrier mobilities make them suitable for high-frequency and low-noise transistors. Furthermore, they all have a Zinc-Blende crystal structure, and several subsets of compounds within this group have similar lattice constants but different band structures. This allows for the epitaxial growth of layered heterostructures, *i.e.* stacks of crystalline semiconductor with different electrical properties from one layer to the next. This effectively allows the construction of potential landscapes for charge carriers along the depth of grown material, which can be patterned in the lateral dimensions either by lithography or by local application of electric gate potentials. Recent years have seen the development go towards materials with high carrier mobility, such as InAs, and InSb. However, much of the technology was developed in the $\text{Al}_x\text{Ga}_{1-x}\text{As}$ system, which remains widespread. The bandgaps of these compounds vary with the Al content from 1.5 eV for pure GaAs to 3.1 eV for pure AlAs. For $x < 0.38$, the bandgap remains direct [118].

Fig. 5.1 shows a heterostructure designed to confine both electrons and holes in a two dimensional plane, near the surface. The photon capturing layer is called the “well”, and consists of pure GaAs surrounded by layers of AlGaAs, which form confinement barriers due to their higher bandgap. Apart from the barriers, multiple thin layers can be grown to form optical Bragg mirrors around the well. By tailoring the mirrors and the layer thicknesses, this type of structure can be fashioned into an efficient absorber of photons of a defined wavelength. It is important to note that this structure is undoped, and therefore differs from a two-dimensional electron gas (2DEG): Until the incidence of a photon with sufficient energy to excite an electron from the valence band, the well remains devoid of free carriers.

All heterostructures used in our photonic samples were designed by PDI, and grown by Molecular Beam Epitaxy or Metal-Organic Chemical Vapor Deposition at PDI and Alcatel Thales III-V lab. The one shown in Fig. 5.1 is the final design for our photon detector samples, which achieved a photo-electrical conversion efficiency greater than 90 %, as measured by optical absorption [119].

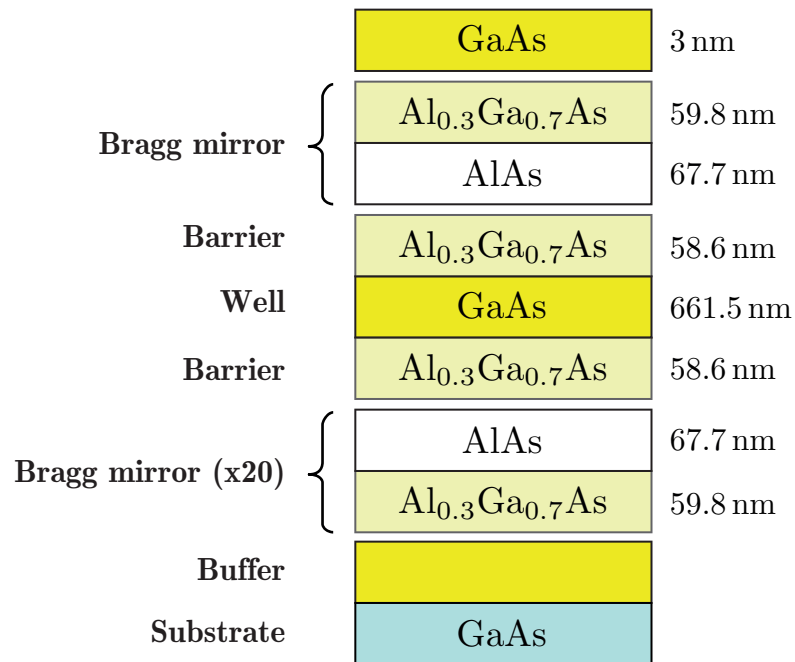


Figure 5.1: A heterostructure designed to produce and trap electron-hole pairs from incoming photons. The Bragg mirrors ensure that a photon of the right wavelength resonated for a long time in the GaAs well, increasing the chance of absorption. Once a photon has been absorbed, the high bandgap of the barriers prevents both the electron and the hole from escaping the GaAs layer.

5.2 Surface acoustic wave carrier transport

Although GaAs is only weakly piezoelectric, it is possible to generate SAW efficiently on its (001) surface, as described in Sec. 2.2. Wherever the acoustic wave propagates, it produces a periodic potential which penetrates the well of the heterostructure. At high acoustic power, the field can be strong enough to deplete a two-dimensional electron gas, dividing it into a sequence of moving quantum dots, given a suitable lateral confinement. This has been utilized in attempts to realize a quantized current source for metrological purposes [120].

When traversing a structure like the one shown in Fig. 5.1, the moving SAW potential serves two purposes: When a photon is absorbed and an electron excited to the conductance band, the electron and the hole are created in the immediate vicinity of each other, largely overlapping. Unless action is taken, this leads to a fast recombination and re-emission of the photon. With the SAW applied, given a sufficient amplitude, the electron is attracted to the positive part of the moving potential wave, and the hole to the negative one. Hence, the two are separated by $\lambda_{SAW}/2$, and thereby kept from recombining. Since the electric field from the SAW is strongest at the surface, the carriers are also kept near the top of the well, where they can be most easily accessed by electrical terminals deposited on top of the chip.

With the electrons and holes trapped by the piezoelectric potential of the SAW, the carriers move along with the SAW beam at speed v_{SAW} . By applying attractive potentials to gates on the surface, they can be made to follow the SAW directly underneath the guiding electrodes, while still being confined vertically to the GaAs potential well. The absorption and transport efficiencies of this scheme was demonstrated by PDI as part of the ACDET II project [119]. At the ends of the carrier guides, two RF-SETs are deposited on the chip surface to detect the incoming electrons and holes. Since the bandwidth of the RF-SET is limited to around 10 MHz, it is not possible to detect the carriers while they are passing the SET island at the speed v_{SAW} . Rather, the carriers must be electrostatically trapped near the SETs for a sufficiently long time to be reliably detected. Since the SET also responds strongly to the SAW potential (see Ch. 3), the most suitable trapping method was determined to be an attractive common-mode potential applied to the RF-SET source and drain. The SAW power should then be turned off once the carriers reach the SET, in order for the SET to measure their charges undisturbed. For improved fidelity, the signals from the two SETs can be recorded differentially [121] or in a setup for detecting correlations between electrons and holes.

To improve the electro-acoustic performance of the devices, the surface was covered with a sputtered layer of strongly piezoelectric ZnO, which also served as a dielectric to localize the electric field from the surface electrodes to the desired regions: A small hole was etched in the ZnO layer at the charge detection areas, and the SET was deposited inside the window whereas its leads went on top of the ZnO. By this arrangement, the electric field in the well due to the common-mode biased SET is stronger in the detection region than elsewhere under the leads, allowing the charge to be trapped at the SET.

A schematic of the initial plan for the SAW-based sample is shown in Fig. 5.2. Several of the technical features are not included in this schematic, but were added to the design during the course of the project. The final SAW-based detector layout is shown in Fig. 5.3. Due to the complex fabrication, no device could unfortunately be made to work well enough to be tested under cryogenic conditions. In particular, the deposition and processing of ZnO turned out to be problematic, especially in combination with SET fabrication.

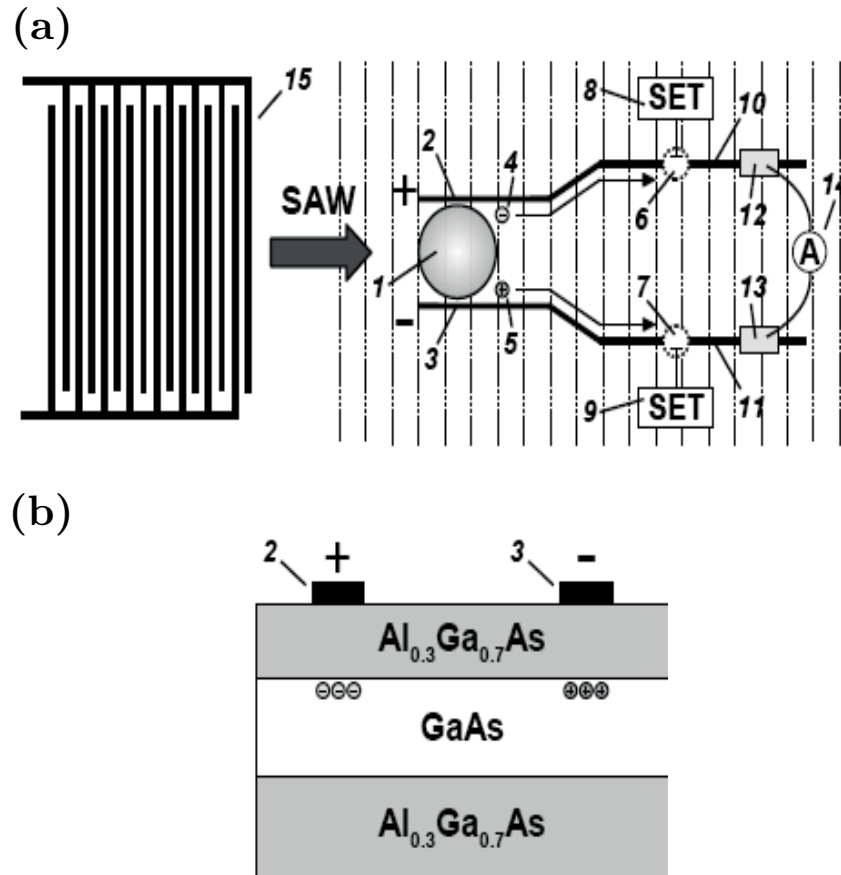


Figure 5.2: Proposal schematic of the ACDET sample design, top view (a) and side view (b), courtesy of V. Talyanskii and adapted from Paper III: Photons impinging on the absorption region (1) excite electron-hole pairs. These are separated and transported by the electric field from the SAW, which emanates from the IDT (15). The lateral field from the guides (2, 3) brings electrons (4) to follow the top guide and holes (5) to follow the bottom one. At the ends of the guides are the detection regions (6, 7), where RF-SETs (8, 9) detect the charge carriers upon their arrival. After detection, the carriers are disposed to ohmic contacts (12, 13). For characterization in the absence of SETs, the current through the ohmic contacts (14) indicates the efficiency of photon absorption and carrier transport.

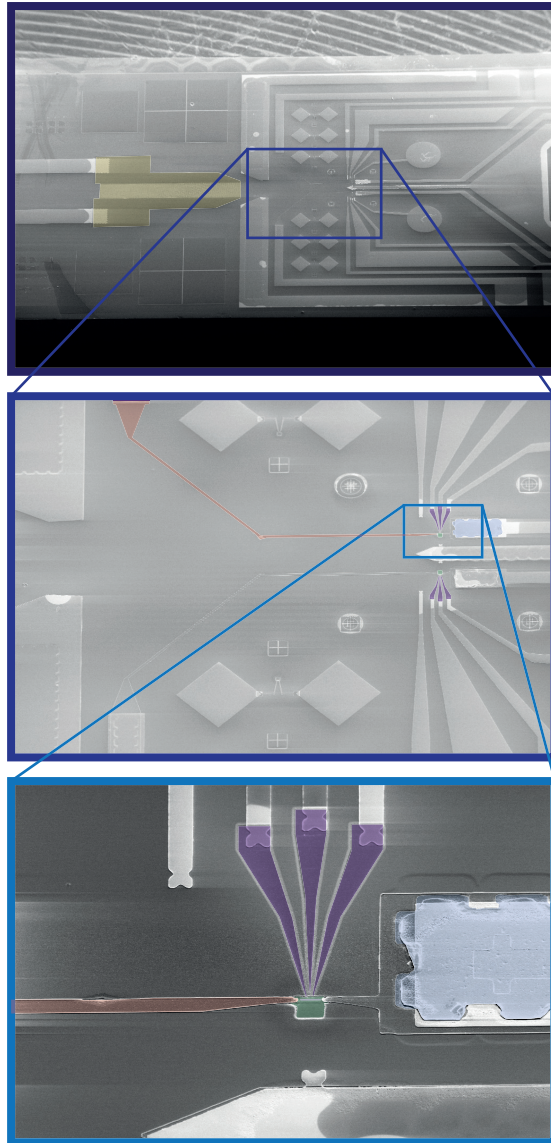


Figure 5.3: Successively zoomed-in electron micrographs of a sample for SAW-based photon detection, in false-color. Yellow: Uni-directional IDT. Red stripe: Electron guide deposited underneath a layer of ZnO. There is also an identical guide for holes, not marked with color. Green: Charge detection region with a window etched in the ZnO. Purple: SET, with the island deposited in the ZnO window. Blue: Ohmic N-type contact. The red dot marks the center of the light absorption area.

5.3 Resistive carrier guiding

During the course of the project, the field from the guiding electrodes was found to be sufficient to separate electrons from holes without need for the short-range field provided by the SAW [119]. In the light of this, we attempted an alternative approach to the SAW transport, where the carriers are forced to move by potential gradients applied over the guides, in addition to the common-mode guide potentials required to attract carriers from the point of photon incidence. In order to not dissipate too much power on the chip, the guides must be made from a highly resistive material, in our case NiCr. Similarly to the trapping scheme for the SAW-based samples, the leads the resistive guides should reside on an insulating layer. Otherwise the carriers would follow the lead all the way to the bonding pad rather than stopping at the end of the guide, where the SET is deposited. After detection at the SET, the gradient along the guide is inverted, forcing the carrier to an ohmic contact at the opposite end of the guide.

The resistive-guide variety of samples were made from the same heterostructure as the SAW-based samples. The P-type ohmic contacts were fabricated during a visit to PDI, and all subsequent fabrication could be done in the Nanofabrication laboratory at Chalmers. Two types of prototypes were fabricated, one with an SET at the end of the electron guide, as described above, and one where the SET was not deposited, but a second N-type ohmic contact was deposited in its place. A sample of the first kind is shown in Fig. 5.4. Tests on the second type of sample indicated that photo-generated carriers in the well could be guided between the ohmics by the electric fields, but the measurements were not fully conclusive. In the other kind of sample, the SET could be seen to respond to light, but only at relatively high intensities.

5.4 Conclusion and outlook

Although there is some merit to this approach to photon detection once technical difficulties are overcome, the investigations were not carried past the stage of prototyping. The niche of applications for which cryogenic detector operation is acceptable is relatively small, and the great progress of TES bolometers puts competing technologies at a disadvantage.

Although the work on photon detectors based on SAW and RF-SETs did not culminate in a functional device, we discovered in the course of the project that the RF-SET can be used as a sensitive probe for SAW. This spin-off result is discussed in detail in Ch. 3.

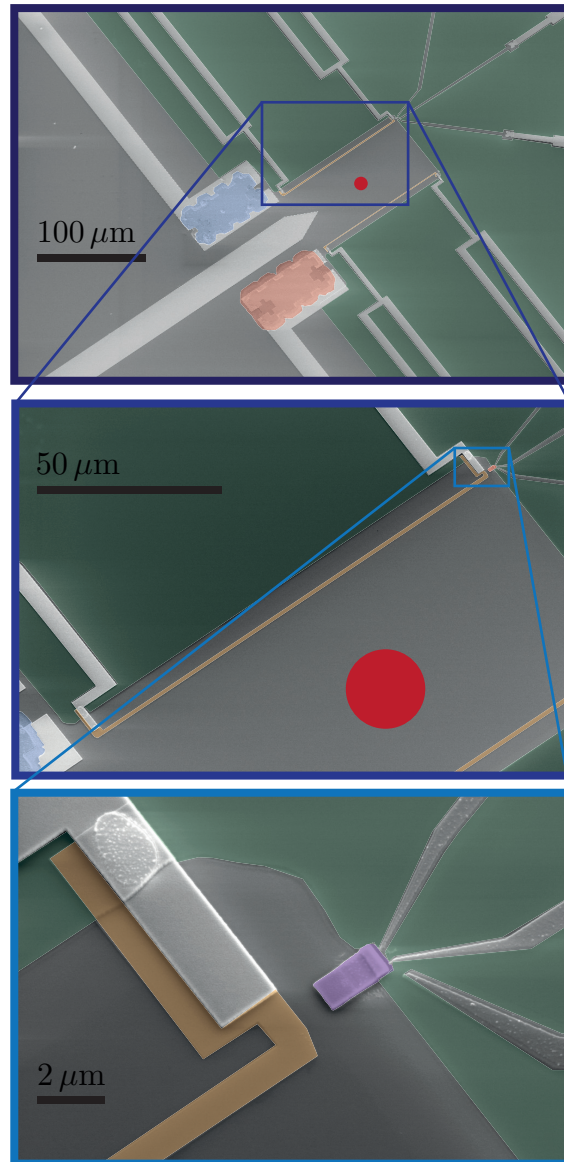


Figure 5.4: Successively zoomed-in electron micrographs of a photon detector prototype of the “resistive-guide” type, in false-color. Green: Evaporated SiO_2 ; yellow: NiCr guides, each with a resistance of approximately $10\text{ k}\Omega$; blue and red: Ohmic contacts of N-type and P-type, respectively; Purple: SET island. The red dot marks the light absorption area.

Chapter 6

Charge pumping with single-electron devices

The ampere is one of the seven base units in the International System of Units (SI), from which all other units are derived. In spite of this, it is in practice derived from the units of voltage and resistance, since these have extremely accurate manifestations in the Josephson effect and the Quantum Hall effect, respectively.

A long standing goal in the field of electrical metrology is to construct a quantized current source independent of the volt and the ohm, capable of transporting electrons through a circuit at an accurately known rate f to give a current

$$I = e f \quad . \quad (6.1)$$

Such a standard could be used to rearrange dependencies between units and constants in the SI [122]. Of more fundamental scientific interest, however, is the possibility to compare the quantized electron current with the quantum standards for the ohm and the volt, in an experiment known as the Metrological triangle [123–125]. With sufficient precision, such an experiment could potentially reveal unknown corrections to the constituent equations of the three standards.

The first quantized current source was the *single-electron turnstile* [4], which has similarities with the SINIS turnstile discussed below. Its successor, the *single-electron pump* was demonstrated by Pothier *et al.* [5], and subsequently improved to metrological accuracy at NIST [126]. The 7-junction electron pump at NIST still holds the record for accuracy with 15 ppb [6, 127]. However, the multijunction pumps are limited to relatively low current ($\lesssim 20$ pA), and the many control lines (each subject to a random charge offset) make them challenging to operate [86]. It is therefore not feasible to increase the current substantially by connecting many such pumps in parallel.

Several other methods for achieving quantized current have been proposed and/or realized, based *e.g.* on surface acoustic wave transport [120], Cooper pair sluicing [128], electron counting with an RF-SET [129], and Quantum phase slips in superconducting nanowire [130]. However, none of these has so far approached the extreme levels of accuracy required for metrological experiments.

In 2007, two promising new candidates for a next generation charge pump were indepen-

dently presented: The adiabatic semiconducting pump [131] and the hybrid SINIS¹ turnstile [7]. Both of these are in principle capable of producing high currents, and they both use a single gate for pumping, which makes them relatively easy to operate and parallelize. The adiabatic pump has recently demonstrated an accuracy of less than 1 ppm [132].

Although some attempts at fabricating semiconductor pumps from GaAs heterostructure provided through the ACDET project (Ch. 5), we soon turned our efforts to the SINIS turnstile. The work on such devices was done in collaboration with the group at Aalto University in Finland, headed by Jukka Pekola, where the first device of this type was demonstrated.

6.1 Photon-assisted tunneling in a resistive electron pump

The experiments on Photon Assisted Tunneling took place at the National Physical Laboratory, under the supervision of Stephen Giblin, and were disseminated in the M.Sc thesis of the author [133] and in Paper IV. Since Ref. [133] discusses this experiment in detail, the overview given here will be brief.

An electron pump consists of a sequence of tunnel junctions, connected by islands with high charging energies relative to the temperature. The induced charge Q_g for each island is controlled with a separate gate, and by cycling the gates at different phases, an electron can be transported by tunneling from one island to the next, all the way from source to drain. For its basic operation, the pump must have least $n_J = 3$ junctions.

The dominant error source in a few-junction pump is co-tunneling of electrons, where the synchronous tunneling by several electrons transports one electron all the way through the pump, even though each of the individual tunneling events would be prohibited by the Coulomb blockade if they had been separated in time. For each extra junction added to the pump, one more electron must tunnel in synchronization with the others in order for a co-tunneling event to take place. Hence, the rate of co-tunneling decreases exponentially with the number of junctions.

Since the complexity of pump operation also increases with n_J , an alternative solution to the co-tunneling problem is to embed the pump in a high-impedance environment [134, 135]. According to Ref. [134], each resistance quantum $R_K \approx 26 \text{ k}\Omega$ in series with the pump should work as well as an additional junction in blocking co-tunneling, assuming that parasitic elements can be neglected.

However, experiments on the 7-junction pump showed that with common co-tunneling sufficiently suppressed, additional errors are observed, which are not accounted for by standard theory. It was proposed that the extra errors are caused by Photon-Assisted (co-) Tunneling (PAT) [43, 44, 136], possibly due to the high-frequency end of the $1/f$ charge noise.

In Ref. [44], Covington *et al.* investigated PAT in the 7-junction pump by applying calibrated microwave signals to its source terminal and studying the rates of leakage and pumping errors with an SET.

We sought to do similar experiment, but for a pump with a series resistor (R-pump) fabricated by Sergey Lotkhov at PTB Braunschweig. The pump had four junctions, with gates coupled to the two islands closest to the source. On the drain side, the pump is terminated in a “memory island” where electrons can enter and exit and be detected with an SET. On the

¹SINIS is an abbreviated description of the sequence of materials that make up the device. S stands for superconductor, I for insulator (tunnel barrier), and N for normal metal.

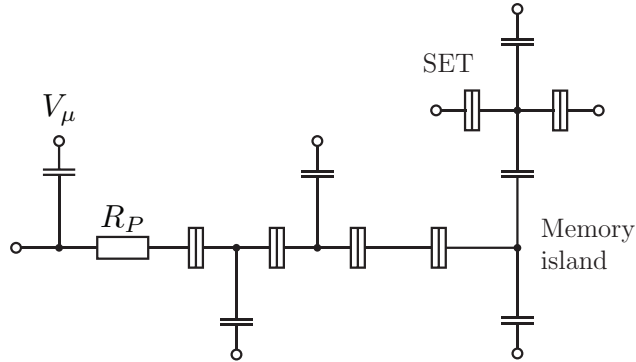


Figure 6.1: Schematic of the 4-junction R-pump. The SET was used to count electrons leaking onto the Memory island through the pump, while microwaves of amplitude V_T were applied to the pump resistor R_P .

source side, the pump had a resistor $R_P \approx 80 \text{ k}\Omega$ made of CrO_x . Fig. 6.1 shows a schematic of the device.

With the sample cooled in a dilution refrigerator, we applied a microwave signal to the source resistor, and measured the leakage through the pump as a function of the applied microwave amplitude V_T . We extrapolated the microwave amplitudes over the pump junctions from measurements of PAT in the SET, fitted with the theory of Tien & Gordon [136].

For a fixed microwave frequency of $\omega/2\pi = 18 \text{ GHz}$, the results were in agreement with the predictions of Ref. [136], with a leak rate limited by two-photon processes². However, since we only had reliable data at one frequency, we could not draw any strong conclusions about the merits of the series resistor for inhibiting photon-assisted tunneling through the pump.

6.2 Principles of the SINIS turnstile

The SINIS turnstile has the same physical design as an SET, only with the island made of normal metal and the leads superconducting (see Fig. 2.2). Its operation resembles that of the original single-electron turnstile by Geerligs *et al.* [4]: It is DC biased in the direction of the current, and a single gate is cycled to pick an electron from the source and deposit it in the drain. However, where the original turnstile only makes use of Coulomb blockade to block unwanted transitions, the SINIS turnstile (“turnstile” henceforth) uses the Coulomb blockade in combination with the BCS energy gap in superconductors for its operation (see Sec. 2.1.6).

The turnstile is typically biased at $V_b \approx \Delta/e$, where Δ is the gap energy of the superconductor. Assuming low temperature, so that there are no excited quasiparticles (QPs), the only way an electron-like charge carrier (“electron” henceforth) can move from source to drain is from the lower QP branch of the source, onto the island, and out through the upper QP branch of the drain. Fig. 6.2 (a) illustrates the energy scales involved, and it is clear from this figure that no current can flow even in the absence of Coulomb blockade, since the relevant bands of the source and drain are separated by the energy $2\Delta - V_b$. The fact that transitions

²In Paper IV, the leakage rate is fitted with an exponential function in the microwave amplitude V_T , rather than the $\Gamma \propto V_T^{2n}$ predicted for an n -photon process, predicted in Ref. [136] and observed in Ref. [44]. The latter model is used in Ref. [133]

through the device as a whole are energetically unfavorable also means that it is immune to co-tunneling.

Although DC current is suppressed, it is possible to transport electrons one by one by repeatedly cycling the gate charge $n_g = V_g C_g / e$ at an amplitude \tilde{n}_g . Two charge states of the island, $n = 0$ and $n = 1$, are used for pumping, where n is the number of excess electrons on the island³. They differ in energy by $\delta E_C = E_C(1 - 2n_g)$. The pumping cycle is illustrated in Fig. 6.2(a-d), and examples of quantized current plateaus are shown in Figs. 2 and 3 of Paper V .

NISIN structures can be used a similar way, but the SINIS design is preferable from a practical perspective since the normal metal island is cooled by selective tunneling of hot electrons, whereas a superconducting island would be heated. Co-tunneling is also an important error process in the NISIN turnstile.

The cycle of Fig. 6.2(a-d) describes ideal operation, but there are also several possible sources of pumping error. The first-order processes include missed tunneling events and back-tunneling. The former may be an issue if the pumping rate is too fast and the junctions have high resistances. The latter is when an electron tunnels off the island to the upper QP branch of the source, or onto the island from the lower QP branch of the drain. This process is only important at high pumping frequencies, since the electron otherwise has time to tunnel to the drain at an early point in the cycle, before the backward transition rate becomes prominent. Back-tunneling can be seen as a decrease in current for increasing pump amplitude \tilde{n}_g .

Although the SINIS structure should in principle not conduct any current at $V_b < 2\Delta/e$, a slight conductance is often observed in this regime. It can be measured by sweeping V_b over the gap region and simultaneously sweeping Q_g slowly over several periods. The gate sweep ensures that the measurements include the charge degeneracy point, which is where the pure sub-gap conductance is observed. The sub-gap conductance can be explained phenomenologically by a broadening of the DOS in the superconductor [75, 76], and it has recently been suggested that this broadening is in fact due to high-frequency photons from the environment [137]. Using good filtering on the measurement lines seems to greatly reduce the sub-gap leakage, and a large part of the joint efforts concerned on-chip decoupling of the turnstiles from their electrical environment.

It is possible to reduce the leakage by using a square waveform to drive the RF gate, rather than a sinusoidal one. This reduces the time the turnstile spends in the vulnerable region around charge degeneracy. Another possible method would be to modulate V_b over the device at twice the pumping frequency, so that the device is unbiased when the gate is swept through the degeneracy point.

The second-order error process known as Andreev tunneling consists of two electrons entering the island, breaking a Cooper pair in the source or drain. In a stability diagram (Fig. 6.2(e)), its activation thresholds are parallel to the thresholds for the desired single-electron thresholds $s_{0 \rightarrow 1}$ and $d_{1 \rightarrow 0}$. For $E_C < \Delta$, the Andreev thresholds are lower than $s_{0 \rightarrow 1}$ and $d_{1 \rightarrow 0}$, so the errors may prohibit metrological pumping accuracy. However, for $E_C > \Delta$, the desired transitions have lower transition thresholds and thus occur earlier in the cycle, so the Andreev current can be avoided altogether. This is studied in Paper V .

The operation of SINIS turnstiles is well covered in Ref. [138], and Ref. [139] discusses the error processes in detail.

³We only treat the first quantization plateau here, but it is possible to transfer several electrons in each cycle, albeit with reduced accuracy.

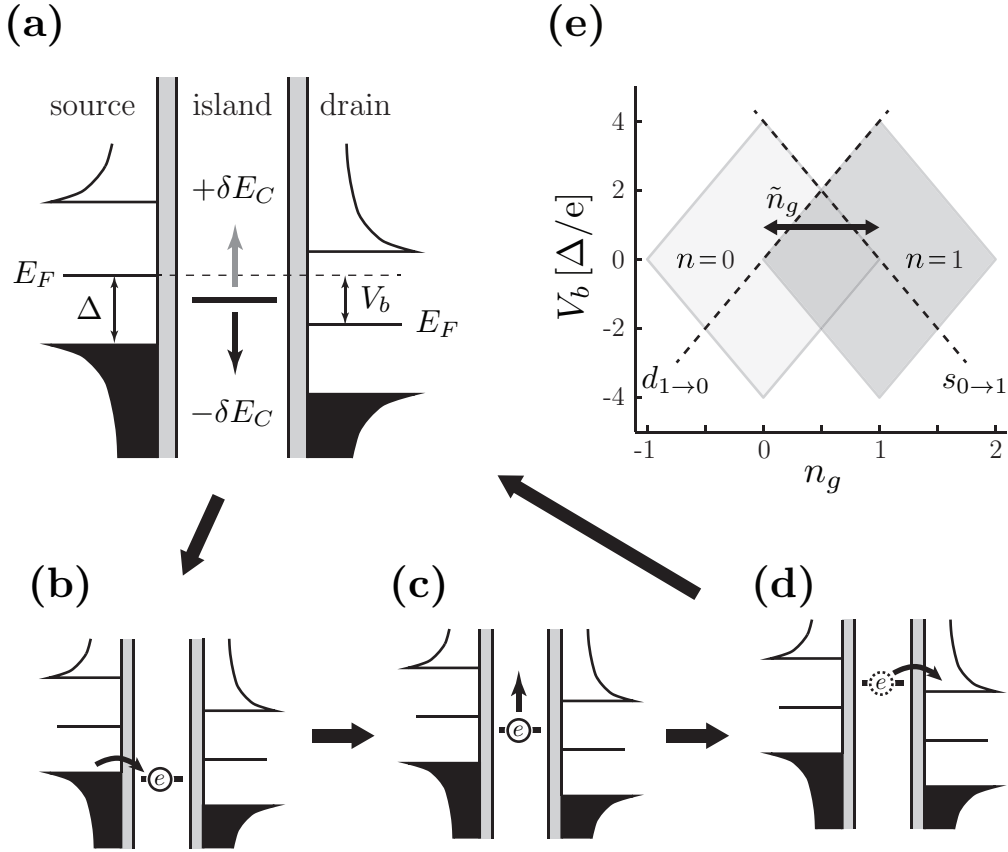


Figure 6.2: Operation and stability of the SINIS turnstile, assuming zero temperature. **(a)** Initial state of the pumping cycle. The energy level plotted for the normal-metal island is $\delta E_C = E_C(1 - 2n_g)$. From the initial state, the gate voltage n_g is increased, decreasing δE_C and making the island attractive to electrons. **(b)** It becomes energetically favorable for an electron to enter the island from the lower QP branch of the source electrode when $\delta E_C \leq V_b/2 - \Delta$. **(c)** After the tunneling event, n_g is lowered again. As δE_C increases, it would be favorable for the electron to tunnel back into the QP branch it came from, but since the only empty state there is the hole it left behind, the rate for such a transition is practically zero. **(d)** For $\delta E_C \geq \Delta - V_b/2$, it becomes favorable for the electron to tunnel off the island and create an excitation in the upper QP branch of the drain. As in step (b), the single carrier occupying the upper QP branch of the drain is at no risk of tunneling back onto the island, and δE_C can again be lowered, making the turnstile ready for a new pumping cycle. **(e)** Stability diagram of a turnstile with $E_C = \Delta$. The large diamonds represent regions where the number of electrons on the island is stable. Either state is stable in the overlapping region, corresponding to panels (a) and (c). The pumping cycle follows the black arrow back and forth, the length of which represents the peak-to-peak value of \tilde{n}_g . The dashed lines show the transitions where the intended tunneling events become favorable ($s_{0 \rightarrow 1}$ for entrance from the source and $d_{1 \rightarrow 0}$ for exit to the drain).

6.3 SINIS samples and experiments

The work on SINIS turnstiles was done in collaboration with the group led by Jukka Pekola at Aalto University in Finland, where these devices were first demonstrated. The first plan for a collaborative experiment was to connect two turnstiles in series with a memory island between them, and couple an RF-SET to the memory island to count the pumping errors. If the concept is extended to three turnstiles and two RF-SETs, it is possible to discern what kind of error occurred, and in which of the turnstiles. With a realistically low error rate, it should be possible to feed calculated compensation signals back to the pumps in realtime, to produce an essentially error-free current quantization.

We initiated attempts in this direction, designing and fabricating some samples, but decided that preliminary studies were necessary in order to reduce the leakage rates through the turnstiles. At this time, no evaporator suitable for making small SIN junctions existed in the Nanofabrication Laboratory at Chalmers, so the last fabrication step had to be done in Finland. The Al-AlO_x-Cu junctions tend to degrade much more rapidly than junctions made of Al-AlO_x-Al, which made it difficult to ship samples between institutions. Instead, the author brought samples from Chalmers that were prepared for two-angle evaporation, and the measurements were done jointly at the Aalto laboratory.

The first set of samples were SINIS turnstiles terminated with arrays of Josephson junctions or SQUIDs. The high impedances of the arrays should serve to provide a calm electrical environment for the turnstiles, thereby reducing the leakage. With SQUID arrays, it is possible to tune the impedances with an electric field, and hence to prove conclusively the impact of the environmental shielding on the turnstile performance.

In order to combine SIS and SIN junctions in the same device, we had to use three-angle evaporation, which requires a large resist undercut (see Sec. 2.4). Since the turnstile junctions need to be small, it is also important to have high lithographic resolution. The resist stack described in Sec. A.1, with a 30 nm thick Ge layer, was used for this purpose. The developed mask for a SQUID array sample is shown in Fig. 2.15(b).

Although the SQUID arrays worked as intended and could be tuned with a magnetic field, the experiments were ultimately unsuccessful, since the high array impedance in combination with the low capacitance of the source and drain electrodes caused instabilities in the turnstile bias, with strong anomalies in the pumping plateaus as a result. A second batch of samples included large shunt capacitances across the turnstiles to alleviate this effect, but these have not yet been characterized.

The second joint experiment was done with the intention of parallelizing turnstiles of high quality, in order to reach high pumping currents with maintained accuracy. Such parallelization had been demonstrated previously [140], but the samples used in [140] exhibited strong frequency-dependent heating which limited the current. The heating was believed to take place in the dielectrics surrounding the RF gate, and we set out to make samples with high-quality materials in a multi-layer process to cure the problem. Each chip had ten turnstiles driven by a common RF gate, but with separate DC gates to cancel offset charges. Fig. 6.3 shows two electron micrographs of such a sample. The RF gate was etched from a ground plane of Al by Reactive Ion Etching (RIE) and the surface was covered with PECVD-grown SiO₂, which was subsequently patterned by RIE. Large-scale-patterning of the ground plane, to allow wire-bonding and to isolate the gate, was done with the SiO₂ as a mask. Bonding leads and pads were deposited by evaporation and lift-off, and a high-resolution Ge mask for two-angle evaporation was prepared in alignment with the RF gate. The patterning was done

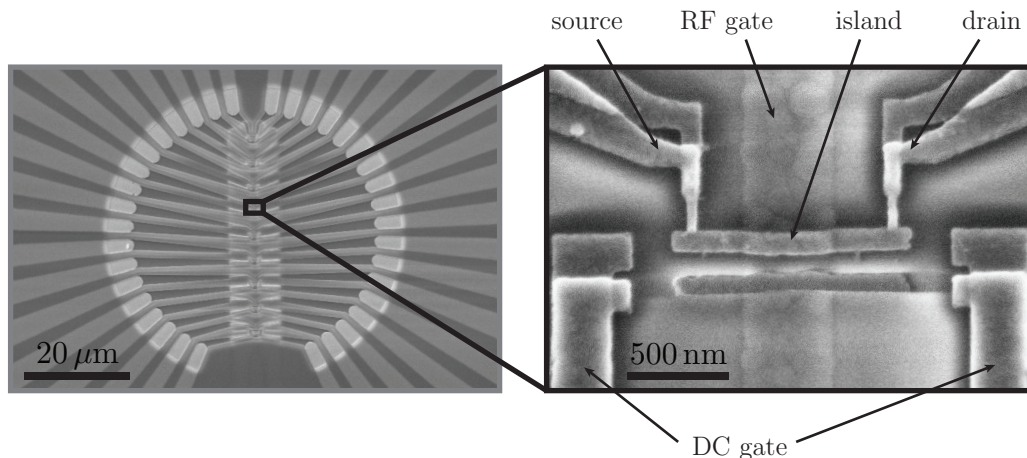


Figure 6.3: Electron micrograph of ten parallel SINIS turnstiles, with a zoom-up on one device.

with contact photolithography and e-beam lithography. The process used 4" wafers of glass and oxidized *Si*. The use of a glass substrate complicates the fabrication procedure, due to charging effects in the e-beam lithography steps (see Sec. 2.4).

Although we did not observe any heating in these samples, they turned out to have high subgap leakage, in spite of the ground plane under the bias leads. In a follow-up experiment, the Finnish group found that the leakage remained after the bonding wire to the RF gate was removed, but that it decreased substantially when the on-chip lead and bonding pad for the RF gate was scratched away from the chip. This is a clear indication that environmental noise reaching the device through the gate can be an important error source, and was the dominant one in these experiments. Subsequent measurements by the Finnish group on one of these samples resulted in Paper V, where Andreev errors in the pumping plateaus were compared between this device and a sample with lower E_C fabricated in Finland.

6.4 Conclusions and outlook

For the SINIS turnstiles, the important error processes have been identified, and methods to avoid the errors have been successful. It remains to be seen whether the error suppression can be maintained all the way to the very high requirements set by quantum metrology. For a moderate error rate, the use of feedback from a pair of RF-SETs remains a viable path to metrological accuracy. With several new types of electron pumps competing to reach this limit, the prospect of closing the Metrological triangle does not seem too distant.

Appendix A

Recipes for sample fabrication

The processing recipes presented here are tailored for the Nanofabrication Laboratory at the Department of Microtechnology and Nanoscience, Chalmers. Hence, they reference specific pieces of equipment by name and tool number, which may not be available elsewhere.

A.1 Three-layer hard mask

This recipe is useful for two- or three angle evaporation of small junctions. It is more complicated than two-layer resists, but produces higher resolution, allows for bigger and more well-controlled undercut, and is insensitive to electron back-scattering.

1. Spin-coat MMA co-polymer to the desired bottom layer thickness, *e.g.* “EL10” (10% solid in Ethyl lactate) at 6000 RPM for 320 nm. Bake for 15 min. at 170°C on a hotplate.
2. Evaporate 15-30 nm Ge resistively from a new boat at low rate (0.4 Å/s). The Balzer evaporator is well suited for this. 15 nm of Ge produces the finest features, but for shadow evaporation of Al, the grain size of the evaporated film is usually large enough that it makes no difference if 30nm of Ge is used. The thicker Ge layer maintains its shape even with very little support from the bottom layer (see Fig. 2.15(b)).
3. Immediately after evaporation, spin-coat ZEP 7000 1:1 in Diglyme, at 2000 RPM for 60 nm.
4. Expose with e-beam at 100 kV with a dose of 350 $\mu\text{C}/\text{cm}^2$. Use no proximity correction but draw the finest features twice (doubled in the pattern CAD file). This reduces resist heating compared with regular dose modulation. For SETs, the outermost 20 nm of the fingers and the 20 \times 20 nm in the corners of the island can be double-exposed like this.
5. Prepare the Oxford RIE (Tool #404) by running a high-power O₂ plasma in the Flourine chamber (make a copy of the recipe “Martin G preclean”).
6. Develop for 30s in Hexyl Acetate under MegaSonic agitation at power 5, no heating. Blow dry with N₂ without prior rinsing.
7. Load the substrate into the etcher on a Sapphire carrier. Etch with a low-pressure CF₄ plasma (make a copy of the recipe “Martin G through Ge”).

8. For non-critical undercut, ash in an isotropic O₂ plasma, *e.g.* recipe “Ash20m” in the Batchtop. Thicker bottom layers require longer ashing times. For smaller undercut, use a low-pressure plasma of O₂ mixed with around 20% Ar to etch vertically to the substrate. Follow that with an isotropic (high-pressure) O₂ ashing plasma to etch the undercut.
9. Lift-off after shadow evaporation can be done in heated acetone.

A.2 Large scale photolithography.

This recipe is useful for contact pads and other big features deposited by lift-off. A similar process can be used for etching if step 3 is omitted. Please beware of some older recipes that were used in the group, which produced smaller and less reliable undercut. This sometimes caused bad contact between the pads and subsequent layers.

1. Spin-coat HMDS Primer at 3000 RPM, bake for 1 min at 110°C
2. Spin-coat LOR3B at 3000 RPM for 350 nm of thickness, bake for 5 min. at 190°C.
3. Spin-coat S1813 at 3000 RPM for 1500 nm thickness. Bake for 2 min. at 110°C.
4. Expose for 10 s at 6 mW/cm², “Hard contact” mode in an MA6 mask aligner.
5. Develop for 30-60 s in MF319. Rinse in water (in a Quick-dump rinser) and blow dry with N₂
6. Optionally, descum in an O₂ plasma, *e.g.* “ash15s” in the Batchtop.
7. Lift-off can be done in acetone, but warm Remover 1165 usually works faster and easier.

Fig. 2.14 shows a cross-section of this resist stack after development and metal evaporation.

A.3 Large-scale e-beam lithography

This recipe is useful for contact pads and other big features deposited by lift-off, when photolithography is too imprecise or for tests on small pieces. Photolithography should be used whenever possible, to avoid wasting e-beam time. A similar process can be used for etching if step 2 is omitted and the development time is shortened to 30-40 s.

1. Spin-coat HMDS Primer at 3000 RPM, bake for 1 min. at 110°C.
2. Spin-coat LOR3A at 2000 RPM for 350 nm of thickness, bake for 5 min. at 190°C.
3. Spin-coat UV5 0.8 (diluted) at 4000 RPM, bake 2 min. at 130°C.
4. Expose with e-beam at 100 kV with a dose of 20 – 55 μC/cm², depending on proximity correction and feature size. 55 μC/cm² is sufficient to make small and isolated alignment marks on top of a metal layer. For large patterns,
5. Post-bake for 90 s at 130°C. This is a critical step and should be done as soon as possible after exposure.

6. Develop for 45-90s in MF24A, rinse in water (in a Quick-dump rinser) and blow dry with N₂. Unless the features are densely spaced, development can continue until the undercut is visible under microscope.
7. Optionally, descum in an O₂ plasma, *e.g.* “ash15s” in the Batchtop.
8. Lift-off can be done in acetone, but warm Remover 1165 usually works faster and easier.

A.4 Small-scale e-beam lift-off

This recipe is useful for fine and dense structures, such as high-frequency IDTs, where the undercut must be kept to a minimum. To minimize the undercut, the thinnest possible bottom layer should be used, $\sim 50\%$ thicker than the film to be deposited. Development in MIBK:IPA selectively removes exposed bottom layer resist, whereas IPA:H₂O etches more isotropically. To simplify the development of the bottom layer, it can be worth exposing “development thermometers” in unused areas of the substrate. These are gratings with a period that varies around the desired undercut. During bottom layer development the thermometers will collapse gradually as the undercut gets too small to support the top layer, starting from the densest part. This gives an indication of the undercut size that is visible under optical microscope.

1. Spin-coat MMA co-polymer to the desired bottom layer thickness, *e.g.* “EL6” (6% solid in Ethyl lactate) at 6000 RPM for 120 nm. Bake for 5 min. at 170 °C on a hotplate
2. Spin-coat ZEP520A 1:2 at 6000 RPM, bake for 10 min at 170°C on a hotplate.
3. Expose at 100 kV. For IDTs and similar structures, proximity correction is essential..
4. Develop for 30 un in Hexyl Acetate under MegaSonic agitation at power 5, no heating. Blow dry with N₂ without rinsing.
5. Develop the bottom layer, *e.g.* 45s in IPA:MIBK under light agitation. Rinse in IPA and blow dry with N₂.
6. Optionally, descum in an O₂ plasma, *e.g.* “ash15s” in the Batchtop.
7. Lift-off after metal deposition can be done in warm acetone.

Acknowledgements

My foremost gratitude goes to professor Per Delsing who has been my supervisor, for his support and confidence in my ability, his massive scientific contributions to the work and his contagious enthusiasm for physics.

I also look back with fondness on the time I spent under Stephen Giblin's supervision at the NPL.

My favorite way to deal with theoretical puzzles has been to go upstairs and look for Göran Johansson, who has been able to handle every problem I have shown up with and always been happy to explain and discuss things on the spot.

Special acknowledgement goes to my tireless partner in noise, Arsalan Pourkabirian, who made heroic efforts in the lab. The work by Joachim Lublin on the same topic also deserves a special mention.

I have had the fortune to work with several collaborators outside Chalmers, and I wish to express my thanks to all of them:

- to John Clarke for sharing his deep insights in physics and sharpening my writing with his red pen.
- to Jukka Pekola for the great hospitality, and the whole group at Micronova – Ville, Antti, Sergey and everyone else – for good collaboration.
- to the partners of ACDET for the noble attempt, and especially Paulo Santos for helping us get traction in the studies of SAW.

The past and present members of QDP and the surrounding groups that I have enjoyed sharing a workplace with are too numerous to list, and I would really prefer not to leave anyone out. I owe special thanks to Henrik Brenning for teaching me the ins and outs of the cleanroom, Philip Krantz for making the artistic cover image, and Fredrik Persson, Kyle Sundqvist, Sergey Kafanov, Jonas Bylander, Samuel Lara and Tine Greibe for particularly enlightening discussions.

I am also grateful to Staffan Pehrson and Lars Jönsson for the many things they have made and fixed, to Marie Fredriksson and Ann-Marie Frykestig for solving all administrative problems, to Hans Odelius for letting me use his equipment, and to the staff in the Nanofabrication Laboratory for their help and advice, especially Bengt Nilsson, Henrik Frederiksen and Örjan Arthursson.

Finally, I want to thank Anna Aspgrén for the mentorship and my friends and family for their support.

Bibliography

1. Averin, D. V. & Likharev, K. K. Coulomb blockade of single-electron tunneling, and coherent oscillations in small tunnel junctions. *Journal of Low Temperature Physics* **62**, 345–373 (1986).
2. Fulton, T. A. & Dolan, G. J. Observation of single-electron charging effects in small tunnel junctions. *Physical Review Letters* **59**, 109–112 (1987).
3. Brenning, H., Kafanov, S., Duty, T., Kubatkin, S. & Delsing, P. An ultrasensitive radio-frequency single-electron transistor working up to 4.2 K. *Journal of Applied Physics* **100**, 114321 (2006).
4. Geerligs, L. J., Anderegg, V. F., Holweg, P. A. M., Mooij, J. E., Pothier, H., Esteve, D., Urbina, C. & Devoret, M. H. Frequency-Locked Turnstile Device for Single Electrons. *Physical Review Letters* **64**, 2691–2694 (1990).
5. Pothier, H., Lafarge, P., Urbina, C., Esteve, D. & Devoret, M. H. Single-Electron Pump Based on Charging Effects. *Europhysics Letters* **17**, 249–254 (1992).
6. Keller, M. W., Martinis, J. M., Zimmerman, N. M. & Steinbach, A. H. Accuracy of electron counting using a 7-junction electron pump. *Applied Physics Letters* **69**, 1804–1806 (1996).
7. Pekola, J. P., Vartiainen, J. J., Möttönen, M., Saira, O.-P., Meschke, M. & Averin, D. V. Hybrid single-electron transistor as a source of quantized electric current. *Nature Physics* **4**, 120–124 (2007).
8. Durrani, Z. A. K. *Single-Electron Devices and Circuits in Silicon* (World Scientific, London, 2009).
9. Wasshuber, C. *Computational Single-Electronics* (Springer, Wien, 2001).
10. Likharev, K. & Averin, D. *Mesoscopic Phenomena in Solids* (eds Altshuler, B., Lee, P. A. & Webb, R. A.) 173–271 (Elsevier, Amsterdam, 1991).
11. *Single Charge Tunneling: Coulomb Blockade Phenomena in Nanostructures* (eds Grabert, H. & Devoret, M. H.) (Plenum Press, New York, 1992).
12. Devoret, M. H., Esteve, D. & Urbina, C. Single-electron transfer in metallic nanostructures. *Nature* **360**, 547–553 (1992).
13. Kulik, I. & Shekhter, R. Charge Quantization Effects and Superconductivity of Small Particles. *Soviet Journal of Low Temperature Physics* **2**, 9–13 (1976).
14. Averin, D. V. & Nazarov, Y. V. *Single Charge Tunneling: Coulomb Blockade Phenomena in Nanostructures* (eds Grabert, H. & Devoret, M.) 217–247 (Plenum Press, New York, 1992).

15. Giazotto, F., Heikkilä, T. T., Luukanen, A., Savin, A. M. & Pekola, J. R. Opportunities for mesoscopics in thermometry and refrigeration: Physics and applications. *Reviews of Modern Physics* **78**, 217–274 (2006).
16. Heikkilä, T. & Nazarov, Y. V. Statistics of Temperature Fluctuations in an Electron System out of Equilibrium. *Physical Review Letters* **102**, 130605 (2009).
17. Korotkov, A. N., Samuelsen, M. R. & Vasenko, S. A. Effects of overheating in a single-electron transistor. *Journal of Applied Physics* **76**, 3623–3631 (1994).
18. Laakso, M. A., Heikkilä, T. T. & Nazarov, Y. V. Fully Overheated Single-Electron Transistor. *Physical Review Letters* **104**, 196805 (2010).
19. Schmidt, D. R., Schoelkopf, R. J. & Cleland, A. N. Photon-Mediated Thermal Relaxation of Electrons in Nanostructures. *Physical Review Letters* **93**, 045901 (2004).
20. Roukes, M. L., Freeman, M. R., Germain, R. S., Richardson, R. C. & Ketchen, M. B. Hot Electrons and Energy Transport in Metals at Millikelvin Temperatures. *Physical Review Letters* **55**, 422–425 (1985).
21. Kautz, R. L., Zimmerli, G. & Martinis, J. M. Self-heating in the Coulomb-blockade electrometer. *Journal of Applied Physics* **73**, 2386–2396 (1993).
22. Meschke, M., Pekola, J. P., Gay, F., Rapp, R. E. & Godfrin, H. Electron Thermalization in Metallic Islands Probed by Coulomb Blockade Thermometry. *Journal of Low Temperature Physics* **134**, 1119–1143 (2004).
23. Patton, K. R. & Geller, M. R. Phonon spectrum in a nanoparticle mechanically coupled to a substrate. *Journal of Luminescence* **94-95**, 747–750 (2001).
24. Underwood, J. M., Lowell, P. J., O’Neil, G. C. & Ullom, J. N. Insensitivity of Sub-Kelvin Electron-Phonon Coupling to Substrate Properties. *Physical Review Letters* **107**, 255504 (2011).
25. Karvonen, J. T. & Maasilta, I. J. Influence of Phonon Dimensionality on Electron Energy Relaxation. *Physical Review Letters* **99**, 145503 (2007).
26. Qu, S.-X., Cleland, A. N. & Geller, M. R. Hot electrons in low-dimensional phonon systems. *Physical Review B* **72**, 224301 (2005).
27. Wellstood, F. C., Urbina, C & Clarke, J. Hot-electron effects in metals. *Physical Review B* **49**, 5942–5955 (1994).
28. Schmidt, D. R., Yung, C. S. & Cleland, A. N. Temporal measurement of hot-electron relaxation in a phonon-cooled metal island. *Physical Review B* **69**, 140301 (2004).
29. Savin, A. M., Pekola, J. P., Averin, D. V. & Semenov, V. K. Thermal budget of superconducting digital circuits at subkelvin temperatures. *Journal of Applied Physics* **99**, 084501 (2006).
30. Korotkov, A. N. Intrinsic noise of the single-electron transistor. *Physical Review B* **49**, 10381–10392 (1994).
31. Kafanov, S. & Delsing, P. Measurement of the shot noise in a single-electron transistor. *Physical Review B* **80**, 155320 (2009).
32. Käck, A., Wendin, G. & Johansson, G. Full-frequency voltage noise spectral density of a single-electron transistor. *Physical Review B* **67**, 035301 (2003).

33. Korotkov, A. N. & Paalanen, M. A. Charge sensitivity of radio frequency single-electron transistor. *Applied Physics Letters* **74**, 4052–4054 (1999).
34. Johansson, G., Delsing, P., Bladh, K., Gunnarsson, D., Duty, T., Käck, A., Wendin, G. & Aassime, A. *Proceedings of the NATO ARW: Quantum Noise in Mesoscopic Physics* (2002), 337–356.
35. Aassime, A., Gunnarsson, D., Bladh, K., Delsing, P. & Schoelkopf, R. Radio-frequency single-electron transistor: Toward the shot-noise limit. *Applied Physics Letters* **79**, 4031–4033 (2001).
36. Kenyon, M., Lobb, C. J. & Wellstood, F. C. Temperature dependence of low-frequency noise in Al–Al₂O₃–Al single-electron transistors. *Journal of Applied Physics* **88**, 6536–6540 (2000).
37. Zimmerli, G., Eiles, T. M., Kautz, R. L. & Martinis, J. M. Noise in the Coulomb blockade electrometer. *Applied Physics Letters* **61**, 237–239 (1992).
38. Zorin, A. B., Ahlers, F. J., Niemeyer, J., Weimann, T., Wolf, H., Krupenin, V. A. & Lotkhov, S. V. Background charge noise in metallic single-electron tunneling devices. *Physical Review B* **53**, 13682–13687 (1996).
39. Paladino, E., Faoro, L., Falci, G. & Fazio, R. Decoherence and 1/f Noise in Josephson Qubits. *Physical Review Letters* **88**, 228304 (2002).
40. Vion, D., Aassime, A., Cottet, A., Joyez, P., Pothier, H., Urbina, C., Esteve, D. & Devoret, M. H. Manipulating the quantum state of an electrical circuit. *Science* **296**, 886–889 (2002).
41. Bergli, J., Galperin, Y. M. & Altshuler, B. L. Decoherence in qubits due to low-frequency noise. *New Journal of Physics* **11**, 025002 (2009).
42. Bylander, J., Gustavsson, S., Yan, F., Yoshihara, F., Harrabi, K., Fitch, G., Cory, D. G., Nakamura, Y., Tsai, J.-S. & Oliver, W. D. Noise spectroscopy through dynamical decoupling with a superconducting flux qubit. *Nature Physics* **7**, 565–570 (2011).
43. Kautz, R. L., Keller, M. W. & Martinis, J. M. Noise-induced leakage and counting errors in the electron pump. *Physical Review B* **62**, 15888–15902 (2000).
44. Covington, M., Keller, M. W., Kautz, R. L. & Martinis, J. M. Photon-Assisted Tunneling in Electron Pumps. *Physical Review Letters* **84**, 5192–5195 (2000).
45. Machlup, S. Noise in Semiconductors: Spectrum of a Two-Parameter Random Signal. *Journal of Applied Physics* **25**, 341–343 (1954).
46. Dutta, P. & Horn, P. M. Low-frequency fluctuations in solids: 1/f noise. *Reviews of Modern Physics* **53**, 497–516 (1981).
47. Rogers, C. T., Buhrman, R. A., Gallagher, W. J., Raider, S. I., Kleinsasser, A. W. & Sandstrom, R. L. Electron trap states and low frequency noise in tunnel junctions. *IEEE Transactions on Magnetism* **23**, 1658–1661 (1987).
48. Song, D., Amar, A., Lobb, C. J. & Wellstood, F. C. Advantages of superconducting Coulomb-blockade electrometers. *IEEE Transactions on Applied Superconductivity* **5**, 3085–3089 (1995).

49. Wolf, H., Ahlers, F. J., Niemeyer, J., Scherer, H., Weimann, T., Zorin, A. B., Krupenin, V. A., Lotkhov, S. V. & Presnov, D. E. Investigation of the Offset Charge Noise in Single Electron Tunneling Devices. *IEEE Transactions on Instrumentation and Measurement* **46**, 303–306 (1997).
50. Tavkhelidze, A. N. & Mygind, J. Low-frequency noise in single electron tunneling transistor. *Journal of Applied Physics* **83**, 310–317 (1998).
51. Li, T. F., Pashkin, Y. A., Astafiev, O., Nakamura, Y., Tsai, J. S. & Im, H. Low-frequency charge noise in suspended aluminum single-electron transistors. *Applied Physics Letters* **91**, 033107 (2007).
52. Henning, T., Starmark, B., Claeson, T. & Delsing, P. Bias and temperature dependence of the noise in a single electron transistor. *The European Physical Journal B* **8**, 627–633 (1999).
53. Starmark, B., Henning, T., Claeson, T., Delsing, P. & Korotkov, a. N. Gain dependence of the noise in the single electron transistor. *Journal of Applied Physics* **86**, 2132–2136 (1999).
54. Krupenin, V. A., Presnov, D. E., Zorin, A. B. & Niemeyer, J. Aluminum Single Electron Transistors with Islands Isolated from the Substrate. *Journal of Low Temperature Physics* **118**, 287–296 (2000).
55. Astafiev, O., Pashkin, Y. A., Nakamura, Y., Yamamoto, T. & Tsai, J. S. Temperature Square Dependence of the Low Frequency 1/f Charge Noise in the Josephson Junction Qubits. *Physical Review Letters* **96**, 137001 (2006).
56. Zimmerman, N. M., Cobb, J. L. & Clark, A. F. Modulation of the charge of a single-electron transistor by distant defects. *Physical Review B* **56**, 7675–7678 (1997).
57. Kenyon, M., Cobb, J. L., Amar, A., Song, D., Zimmerman, N. M., Lobb, C. J. & Wellstood, F. C. Dynamics of a Charged Fluctuator in an Al-AlO_x-Al Single-Electron Transistor. *Journal of Low Temperature Physics* **123**, 103–126 (2001).
58. Furlan, M. & Lotkhov, S. Electrometry on charge traps with a single-electron transistor. *Physical Review B* **67**, 205313 (2003).
59. Buehler, T. M., Reilly, D. J., Starrett, R. P., Chan, V. C., Hamilton, A. R., Dzurak, A. S. & Clark, R. G. Observing sub-microsecond telegraph noise with the radio frequency single electron transistor. *Journal of Applied Physics* **96**, 6827–6830 (2004).
60. Kafanov, S., Brenning, H., Duty, T. & Delsing, P. Charge noise in single-electron transistors and charge qubits may be caused by metallic grains. *Physical Review B* **78**, 125411 (2008).
61. Mathieson, E. *Induced charge distributions in proportional detectors* tech. rep. (Brookhaven National Laboratory, Upton, New York, 1991).
62. Krupenin, V. A., Presnov, D. E., Savvateev, M. N., Scherer, H., Zorin, A. B. & Niemeyer, J. Noise in Al single electron transistors of stacked design. *Journal of Applied Physics* **84**, 3212–3215 (1998).
63. McWhorter, A. L. *Semiconductor Surface Physics* (ed Kingston, R.) 207–228 (University of Pennsylvania, Philadelphia, 1957).

64. Visscher, E. H., Lindeman, J., Verbrugh, S. M., Hadley, P., Mooij, J. E. & van der Vleuten, W. Broadband single-electron tunneling transistor. *Applied Physics Letters* **68**, 2014–2016 (1996).
65. Pettersson, J., Wahlgren, P., Delsing, P., Haviland, D. B., Claeson, T., Rorsman, N. & Zirath, H. Extending the high-frequency limit of a single-electron transistor by on-chip impedance transformation. *Physical Review B* **53**, 13272–13274 (1996).
66. Schoelkopf, R. J., Wahlgren, P., Kozhevnikov, A., Delsing, P. & Prober, P. The Radio-Frequency Single-Electron Transistor (RF-SET): A Fast and Ultrasensitive Electrometer. *Science* **280**, 1238–1242 (1998).
67. Reilly, D. J. & Buehler, T. M. Direct measurement of the intrinsic RC roll-off in a radio frequency single electron transistor operated as a microwave mixer. *Applied Physics Letters* **87**, 163122 (2005).
68. Knobel, R., Yung, C. S. & Cleland, A. N. Single-electron transistor as a radio-frequency mixer. *Applied Physics Letters* **81**, 532–534 (2002).
69. Bardeen, J., Cooper, L. N. & Schrieffer, J. R. Microscopic Theory of Superconductivity. *Physical Review* **106**, 162–164 (1957).
70. Van Duzer, T. & Turner, C. W. *Principles of superconductive devices and circuits* (Prentice Hall, Upper Saddle River, 1999).
71. Tinkham, M. *Introduction to Superconductivity* Second edi (Dover Publications, New York, 2004).
72. Falci, G., Bubanja, V. & Schön, G. Quasiparticle and Cooper pair tunneling in small capacitance Josephson junctions. *Zeitschrift für Physik B Condensed Matter* **85**, 451–458 (1991).
73. Maassen van der Brink, A., Odintsov, A. A., Bobbert, P. A. & Schön, G. Coherent Cooper pair tunneling in systems of Josephson junctions: effects of quasiparticle tunneling and of the electromagnetic environment. *Zeitschrift für Physik B Condensed Matter* **85**, 459–467 (1991).
74. Haviland, D., Harada, Y., Delsing, P., Chen, C. & Claeson, T. Observation of the Resonant Tunneling of Cooper Pairs. *Physical Review Letters* **73**, 1541–1544 (1994).
75. Dynes, R. C., Narayanamurti, V. & Garno, J. P. Direct Measurement of Quasiparticle-Lifetime Broadening in a Strong-Coupled Superconductor. *Physical Review Letters* **41**, 1509–1512 (1978).
76. Dynes, R. C., Garno, J. P., Hertel, G. B. & Orlando, T. P. Tunneling Study of Superconductivity near the Metal-Insulator Transition. *Physical Review Letters* **53**, 2437–2440 (1984).
77. Pekola, J., Maisi, V., Kafanov, S., Chekurov, N., Kemppinen, a., Pashkin, Y., Saira, O.-P., Möttönen, M. & Tsai, J. Environment-Assisted Tunneling as an Origin of the Dynes Density of States. *Physical Review Letters* **105**, 8–11 (2010).
78. Rayleigh, L. On Waves Propagated along the Plane Surface of an Elastic Solid. *Proceedings of the London Mathematical Society* **s1-17**, 4–11 (1885).
79. Plessky, V. P. & Reindl, L. M. Review on SAW RFID tags. *IEEE transactions on ultrasonics, ferroelectrics, and frequency control* **57**, 654–668 (2010).

80. Datta, S. *Surface Acoustic Wave Devices* (Prentice-Hall, Englewood Cliffs, NJ, 1986).
81. Campbell, C. *Surface Acoustic Wave Devices for Mobile and Wireless Communications* (Academic Press, San Diego, 1998).
82. Biryukov, S. V., Gulyaev, Y. V., Krylov, V. V. & Plessky, V. P. *Surface acoustic waves in inhomogeneous media* (Springer, Heidelberg, 1995).
83. Hashimoto, K.-y. *Surface acoustic wave devices in telecommunications: modelling and simulation* (Springer, Heidelberg, 2000).
84. Morgan, D. *Surface Acoustic Wave Filters* Second edi (Academic Press, Amsterdam, 2007).
85. Martinis, J. M., Devoret, M. H. & Clarke, J. Experimental tests for the quantum behavior of a macroscopic degree of freedom: The phase difference across a Josephson junction. *Physical Review B* **35**, 4682–4698 (1987).
86. Keller, M. W. Practical aspects of counting electrons with a single-electron tunneling pump. *The European Physical Journal, Special Topics* **172**, 297–309 (2009).
87. Bluhm, H. & Moler, K. a. Dissipative cryogenic filters with zero dc resistance. *The Review of scientific instruments* **79**, 014703 (2008).
88. O’Connell, A. D., Hofheinz, M., Ansmann, M., Bialczak, R. C., Lenander, M., Lucero, E., Neeley, M., Sank, D., Wang, H., Weides, M., Wenner, J., Martinis, J. M. & Cleland, A. N. Quantum ground state and single-phonon control of a mechanical resonator. *Nature* **464**, 697–703 (2010).
89. Teufel, J. D., Donner, T., Castellanos-Beltran, M. A., Harlow, J. W. & Lehnert, K. W. Nanomechanical motion measured with an imprecision below that at the standard quantum limit. *Nature nanotechnology* **4**, 820–823 (2009).
90. Rocheleau, T., Ndukum, T., Macklin, C., Hertzberg, J. B., Clerk, A. A. & Schwab, K. C. Preparation and detection of a mechanical resonator near the ground state of motion. *Nature* **463**, 72–75 (2010).
91. Massel, F., Heikkilä, T. T., Pirkkalainen, J.-M., Cho, S. U., Saloniemi, H., Hakonen, P. J. & Sillanpää, M. A. Microwave amplification with nanomechanical resonators. *Nature* **480**, 351–354 (2011).
92. Teufel, J. D., Li, D., Allman, M. S., Cicak, K., Sirois, A. J., Whittaker, J. D. & Simmonds, R. W. Circuit cavity electromechanics in the strong-coupling regime. *Nature* **471**, 204–208 (2011).
93. Naber, W., Fujisawa, T., Liu, H. & van der Wiel, W. Surface-Acoustic-Wave-Induced Transport in a Double Quantum Dot. *Physical Review Letters* **96**, 136807 (2006).
94. Thomas, C., Heiderhoff, R. & Balk, L. J. 200 femtometer sensitivity for near-field analysis of surface acoustic waves in a scanning electron / scanning probe microscope hybrid system. *Applied Physics Letters* **90**, 144106 (2007).
95. El Habti, A., Bastien, F., Bigler, E. & Thorvaldsson, T. High-frequency surface acoustic wave devices at very low temperature: Application to loss mechanisms evaluation. *The Journal of the Acoustical Society of America. J. Acoust. Soc. Am. (USA)* **100**, 272–277 (1996).

96. Yamanouchi, K., Nakagawa, H. & Odagawa, H. *Joint Meeting EFTF – IEEE IFCS 2* (IEEE, 1999), 911–914.
97. Johansson, G., Tornberg, L. & Wilson, C. Fast quantum limited readout of a superconducting qubit using a slow oscillator. *Physical Review B* **74**, 100504 (2006).
98. Persson, F., Wilson, C., Sandberg, M. & Delsing, P. Fast readout of a single Cooper-pair box using its quantum capacitance. *Physical Review B* **82**, 134533 (2010).
99. Koch, J., Yu, T., Gambetta, J., Houck, A., Schuster, D., Majer, J., Blais, A., Devoret, M., Girvin, S. & Schoelkopf, R. Charge-insensitive qubit design derived from the Cooper pair box. *Physical Review A* **76**, 042319 (2007).
100. Houck, A. A., Koch, J., Devoret, M. H., Girvin, S. M. & Schoelkopf, R. J. Life after charge noise: recent results with transmon qubits. *Quantum Information Processing* **8**, 105–115 (2009).
101. Hoi, I.-C., Wilson, C., Johansson, G., Palomaki, T., Peropadre, B. & Delsing, P. Demonstration of a Single-Photon Router in the Microwave Regime. *Physical Review Letters* **107**, 073601 (2011).
102. Shen, J. T. & Fan, S. Coherent photon transport from spontaneous emission in one-dimensional waveguides. *Optics letters* **30**, 2001–2003 (2005).
103. Shen, J.-T. & Fan, S. Coherent Single Photon Transport in a One-Dimensional Waveguide Coupled with Superconducting Quantum Bits. *Physical Review Letters* **95**, 213001 (2005).
104. Hoi, I.-C. *Strong Interaction Between a Single Artificial Atom and Propagating Microwave Photons*. Licentiate thesis (Chalmers University of Technology, 2011).
105. Starmark, B. *Low Frequency Noise in the Single Electron Transistor: Instrumentation and Experiments*. Licentiate Thesis (Chalmers University of Technology and University of Gothenburg, 1998).
106. Pohl, R. O., Liu, X. & Thompson, E. Low-temperature thermal conductivity and acoustic attenuation in amorphous solids. *Reviews of Modern Physics* **74**, 991–1013 (2002).
107. Kumar, G. S., Vandersande, J. W., Klitsner, T., Pohl, R. O. & Slack, G. A. Low-temperature heat transport by charge carriers in doped semiconductors. *Physical Review B* **31**, 2157–2162 (1985).
108. Lublin, J. *Title to be decided*. Master Thesis (Chalmers University of Technology, 2012).
109. Savin, A., Manninen, A., Kivinen, P., Pekola, J., Prunnila, M., Ahopelto, J., Kamp, M., Emmerling, M. & Forchel, A. *Physics, Chemistry and Application of Nanostructures - Reviews And Short Notes To Nanomeeting-2001* **9** (2001), 466–469.
110. Zimmerman, N. M., Huber, W. H., Simonds, B., Hourdakis, E., Fujiwara, A., Ono, Y., Takahashi, Y., Inokawa, H., Furlan, M. & Keller, M. W. Why the long-term charge offset drift in Si single-electron tunneling transistors is much smaller (better) than in metal-based ones: Two-level fluctuator stability. *Journal of Applied Physics* **104**, 033710 (2008).
111. Zimmerman, N. & Huber, W. Microscope of glassy relaxation in femtogram samples: Charge offset drift in the single electron transistor. *Physical Review B* **80**, 195304 (2009).

112. Cova, S, Ghioni, M, Lacaïta, A, Samori, C & Zappa, F. Avalanche photodiodes and quenching circuits for single-photon detection. *Applied optics* **35**, 1956–1976 (1996).
113. Gisin, N., Ribordy, G., Tittel, W. & Zbinden, H. Quantum cryptography. *Reviews of Modern Physics* **74**, 145–195 (2002).
114. Clarke, J., Hoffer, G. I., Richards, P. L. & Yeh, N. H. Superconductive bolometers for submillimeter wavelengths. *Journal of Applied Physics* **48**, 4865–4879 (1977).
115. Nahum, M. & Martinis, J. M. Ultrasensitive-hot-electron microbolometer. *Applied Physics Letters* **63**, 3075–3077 (1993).
116. Lee, A. T., Richards, P. L., Nam, S. W., Cabrera, B. & Irwin, K. D. A superconducting bolometer with strong electrothermal feedback. **69**, 1801–1803 (1996).
117. Cleland, A. N., Esteve, D., Urbina, C. & Devoret, M. H. Very low noise photodetector based on the single electron transistor. *Applied Physics Letters* **61**, 2820–2822 (1992).
118. Vurgaftman, I., Meyer, J. R. & Ram-Mohan, L. R. Band parameters for III–V compound semiconductors and their alloys. *Journal of Applied Physics* **89**, 5815–5875 (2001).
119. Jiao, S. J., Batista, P. D., Biermann, K., Hey, R. & Santos, P. V. Electrical detection of ambipolar acoustic carrier transport by surface acoustic waves. *Journal of Applied Physics* **106**, 053708 (2009).
120. Talyanskii, V. I., Shilton, J. M., Pepper, M., Smith, C. G., Ford, C. J. B., Linfield, E. H., Ritchie, D. A. & Jones, G. A. C. Single-electron transport in a one-dimensional channel by high-frequency surface acoustic waves. *Physical Review B* **56**, 180–184 (1997).
121. Schneiderman, J. F., Delsing, P., Shaw, M. D., Bozler, H. M. & Echternach, P. M. Characterization of a differential radio-frequency single-electron transistor. *Applied Physics Letters* **88**, 083506 (2006).
122. Milton, M. J. T., Williams, J. M. & Forbes, A. B. The quantum metrology triangle and the redefinition of the SI ampere and kilogram; analysis of a reduced set of observational equations. *Metrologia* **47**, 279–286 (2010).
123. Likharev, K. K. & Zorin, A. B. Theory of the Bloch-Wave Oscillations in Small Josephson Junctions. *Journal of Low Temperature Physics* **59**, 347–382 (1985).
124. Piquemal, F & Genève, G. Argument for a direct realization of the quantum metrological triangle. *Metrologia* **37**, 207–211 (2000).
125. Keller, M. W. Current status of the quantum metrology triangle. *Metrologia* **45**, 102–109 (2008).
126. Martinis, J. M., Nahum, M. & Jensen, H. D. Metrological accuracy of the Electron Pump. *Physical Review Letters* **72**, 904–907 (1994).
127. Keller, M. W., Eichenberger, A. L., Martinis, J. M. & Zimmerman, N. M. A Capacitance Standard Based on Counting Electrons. *Science* **285**, 1706–1709 (1999).
128. Vartiainen, J. J., Möttönen, M., Pekola, J. P. & Kempainen, A. Nanoampere pumping of Cooper pairs. *Applied Physics Letters* **90**, 082102 (2007).
129. Bylander, J., Duty, T. & Delsing, P. Current measurement by real-time counting of single electrons. *Nature* **434**, 361–364 (2005).

130. Mooij, J. E. & Nazarov, Y. V. Superconducting nanowires as quantum phase-slip junctions. *Nature Physics* **2**, 169–172 (2006).
131. Blumenthal, M. D., Kaestner, B., Li, L., Giblin, S., Janssen, T. J. B. M., Pepper, M., Anderson, D., Jones, G. & Ritchie, D. A. Gigahertz quantized charge pumping. *Nature Physics* **3**, 343–347 (2007).
132. Giblin, S. P., Kataoka, M, Fletcher, J. D., See, P, Janssen, T. J. B. M., Griffiths, J. P., Jones, G. A. C., Farrer, I & Ritchie, D. A. Single electron pumps: towards a quantum representation of the ampere. arXiv:1201.2533 (2012).
133. Gustafsson, M. *Photon Assisted Tunneling in Resistive Electron Pumps*. Master thesis (Chalmers University of Technology, 2005).
134. Golubev, D. & Zaikin, A. Charge fluctuations in systems of mesoscopic tunnel junctions. *Physics Letters A* **169**, 475–482 (1992).
135. Lotkhov, S. V., Zangerle, H., Zorin, a. B. & Niemeyer, J. Storage capabilities of a four-junction single-electron trap with an on-chip resistor. *Applied Physics Letters* **75**, 2665–2667 (1999).
136. Tien, P. K. & Gordon, J. P. Multiphoton Process Observed in the Interaction of Microwave Fields with the Tunneling between Superconductor Films. *Physical Review* **129**, 647–651 (1963).
137. Pekola, J., Maisi, V., Kafanov, S., Chekurov, N., Kemppinen, A., Pashkin, Y., Saira, O.-P., Möttönen, M. & Tsai, J. Environment-Assisted Tunneling as an Origin of the Dynes Density of States. *Physical Review Letters* **105**, 026803 (2010).
138. Kemppinen, A., Meschke, M., Möttönen, M., Averin, D. V. & Pekola, J. P. Quantized current of a hybrid single-electron transistor with superconducting leads and a normal-metal island. *The European Physical Journal Special Topics* **172**, 311–321 (2009).
139. Averin, D. & Pekola, J. Nonadiabatic Charge Pumping in a Hybrid Single-Electron Transistor. *Physical Review Letters* **101**, 066801 (2008).
140. Maisi, V. F., Pashkin, Y. A., Kafanov, S., Tsai, J.-S. & Pekola, J. P. Parallel pumping of electrons. *New Journal of Physics* **11**, 113057 (2009).

